ABSTRACT

Title of Dissertation: UNVEILING THE SELF-ASSEMBLY OF POLYMER-GRAFTED NANOPARTICLES IN SELECTIVE SOLVENTS

Chelsey Lamar, Doctor of Philosophy, 2023

Dissertation directed by: Professor Zhihong Nie,
Department of Chemistry and Biochemistry

The self-assembly of inorganic nanoparticles (NPs) has garnered considerable attention due to the potential for fabricating functional structures with unique collective properties. In recent years, polymers have emerged as valuable candidates in assisting the organization of NPs into complex architectures with multiple capabilities. Researchers have shown that polymer-grafted nanoparticles (PGNPs) facilitate the use of advanced nanostructures with tailored properties in biomedical applications. Although, continued exploration of the rational design and tailoring of PGNP assemblies is needed to expand our understanding before we can fully realize the potential of these structures in desired applications. My dissertation aims to investigate the fundamental aspects and elucidate the underlying mechanisms in the self-assembly of PGNPs for modern biomedical applications.

A facile and versatile solution-based strategy was utilized to explore the individual self-assembly of PGNPs with anisotropic NPs and the co-assembly of binary PGNPs with distinct sizes. We focused on designing, characterizing, and exploring the optical properties of hierarchical

assembly structures produced from inorganic NPs tethered with amphiphilic block copolymers (BCPs). Individual PNGPs with anisotropic NPs and binary mixtures of small and large PGNPs produce vesicle structures with well-defined packing arrangements. My work shows how key parameters, including polymer chain length, nanoparticle size, and concentration, influence the self-assembly behavior and the formation of vesicles in each system. Through a combination of experimental observations and theoretical considerations, I highlight the significance of polymer shell shape in dictating the self-assembly behavior of individual anisotropic PGNPs. Moreover, I demonstrate that elevated temperatures impacted the stability and optical responses of the vesicle structures. In co-assembly studies, my work describes the macroscopic segregation of PGNPs with different sizes in the vesicular membrane, which is attributed to the conformation entropy gain of the grafted copolymer ligands. This research will provide valuable insights into the self-assembly behavior and fundamental design of PGNP structures relevant to biomedical applications.

UNVEILING THE SELF-ASSEMBLY OF POLYMER-GRAFTED NANOPARTICLES IN SELECTIVE SOLVENTS

by

Chelsey Lamar

Dissertation submitted to the Faculty of the Graduate School of the
University of Maryland, College Park, in partial fulfillment
of the requirements for the degree of
Doctor of Philosophy
2023

Advisory Committee:
Professor Sang Bok Lee, Chair
Professor Zhihong Nie
Professor Jeffery T. Davis
Professor Neil V. Blough
Professor Mohamad I. Al-Sheikhly, Dean's Representative

Dedication

To my Dad, Jeffrey Alan Lamar.

Acknowledgements

First and foremost, I would like to thank God for His grace, guidance, and blessings throughout this entire process. His presence and strength have provided me with the resilience and fortitude needed to overcome obstacles and pursue this research with dedication. My sincere gratitude goes to my husband, Nas. Your belief in my abilities, even during moments of doubt, has propelled me forward. I am truly blessed to have you by my side. To my parents, I am grateful for the sacrifices my Mom has made to support me in raising my son, Jeremy, while I had to work late nights in the lab. I also want to acknowledge the immense impact that my Dad has had in raising me. His unwavering love, belief in me, and understanding have continued to propel me forward, even though he is no longer with us. I would like to express my deep appreciation to my dear friends and family for their unwavering faith in my abilities, their willingness to listen during moments of frustration, and their insightful conversations have been a constant source of inspiration.

I would like to extend a heartfelt thank you to my advisor, Dr. Zhihong Nie. Thank you for imparting your knowledge, continuing to invest in me, and guiding me through my research journey. I would like to express my gratitude to all the members of the Nie lab, especially Marcus Dr. Kong, Kyle, Xiaoying, and Qian, who generously shared their time and knowledge throughout my time in graduate school. I also would like to especially thank Scott Holdren, Dr. Liou, and Yijing for supporting me throughout the data collection and analysis processes.

I extend my heartfelt appreciation to the staff and faculty in the Department of Chemistry and Biochemistry. Thank you to Dr. Reutt-Robey and Dr. Lee for fostering

a supportive environment and to all the faculty who were pivotal in helping make the necessary accommodations for me to continue my research. I am truly thankful for the members of my dissertation committee, Dr. Davis, Dr. Blough, and Dr. Al-Sheikhly. Their commitment to academic excellence and their willingness to dedicate their time to review and provide guidance is deeply appreciated. Special thanks to Dr. Davis for recruiting me and Dolores and Carl for being a constant source of encouragement.

I would like to take a moment to specifically acknowledge the student members of NOBCChe, Hakeem, Sandra, and Yehnara, and our faculty advisors Dr. Dayie, and Dr. LaRonde. They have provided me with valuable insights and perspectives, engaged in fruitful discussions, and offered words of encouragement during challenging times.

I would also like to acknowledge Ms. Parker, Marissa, Migdalia, Peter, and Sunji who played an instrumental role in shaping my professional and personal growth. Their dedication to students in STEM and their camaraderie has made this academic endeavor all the more meaningful. I am deeply grateful for their unwavering support and the lasting mark they have left on my journey.

Table of Contents

List of Figures

Figure 2.10 (a) Schematic illustration of corona morphology dependence on BCP concentration and representative SEM images of B-PGNPs of Au NCs prepared with different concentrations of thiol-terminated polystyrene-*b*-polyethylene oxide: 0.01, 0.02, 0.06, 0.25 mg/mL (left to right). (b) Ligand shell thickness, *l*, measured from SEM images as a function of BCP concentration for 60 nm Au NCs in the dried state. Representative SEM images of (c,f) sheet-like aggregates, relatively (d,g) large and (e,h) small vesicles assembled from 60 nm Au NCs modified with PS_{130}-b-PEO_{45} copolymers.

Figure 2.11 Representative SEM images of (a-c) defected vesicles before thermal treatment and (d-f) vesicle structures after thermal treatment in 3 different samples. (g) statistical analysis of vesicle dimensions in different samples. Corresponding UV-Vis spectra of vesicle assemblies taken (h) after dialysis at room temperature 25 ℃' and (i) after cooling down to room temperature after thermal treatment 25 ℃''.

Figure 2.12 (a-f) Representative SEM images of morphological transitions induced by thermal treatment at 50 ℃ in 3 different samples of vesicular assemblies. (g) Corresponding UV-Vis spectra of different samples taken immediately after thermal treatment.

Figure 3.1 Schematic Illustration of building blocks in different binary mixtures used for the concurrent self-assembly of B-PGNPs.

Figure 3.2 SEM images of Au NS with different sizes and corresponding UV-Vis absorption spectrum of Au nanospheres with different dimensions.

Figure 3.3 TGA of copolymer ligand weights for different hybrid building blocks.

Figure 3.4 Representative SEM images of patchy vesicles assembled from a binary mixture of (a, b) 10 nm and 60 nm and (c, d) 20 nm and 60 nm Au nanospheres grafted with PS_{421}-b-PEO_{45} copolymer ligands. (e) DLS spectrum of modified Au NPs before and after self-assembly.

Figure 3.5 Large are and close-up SEM images of patchy vesicles assembled from a binary mixture of (a, b) 10 nm Au NS and 60 nm Au NC grafted with PS_{211}-b-PEO_{45} and (c, d) 30 nm Au NS and 60 nm Au NC grafted with PS_{130}-b-PEO_{45} copolymer ligands.

Figure 3.6 SEM images of the resulting assemblies produced from binary mixtures of 10 nm and 60 nm gold nanospheres grafted with different BCP lengths. Binary mixtures were prepared at a 1:1 volume ratio.

Figure 3.7 Phase diagrams of different assembly morphologies produced from binary mixtures of 10 nm and 60 nm gold nanospheres grafted with different BCP lengths for 3 different volume ratios of small to large B-PGNPs, v_s: v_L including 1:3 (a) 1:1 (b) and 3:1 (c).

Figure 3.8 The effect of BCP lengths grafted to Au NC on the co-assembly behavior. SEM images of the resulting assemblies produced from binary mixtures of NS-10-PS_{97}-b-PEO_{45} mixed with (a) NC-60-PS_{97}-b-PEO_{45} (b) NC-60-PS_{250}-b-PEO_{45} (c) NC-60-PS_{652}-b-PEO_{82} and of NS-10-PS_{652}-b-PEO_{82} mixed with (d) NC-60-PS_{130}-b-PEO_{45} (e) NC-60-PS_{250}-b-PEO_{45} (f) NC-60-PS_{652}-b-PEO_{82}. (g) corresponding UV-Vis absorption spectrum of NS-10-PS_{652}-b-PEO_{82} grafted with different BCP lengths.

Figure 3.9 The effect of feeding ratio on the formation of hybrid vesicles in Binary System A. Representative SEM images of the resulting assemblies produced from B-PGNPs with 10 nm and 60 nm gold nanospheres at a 3:1 volume ratio of small and large B-PGNPs.

List of Tables

List of Abbreviations

1D	One dimensional
2D	Two dimensional
3D	Three dimensional
AA	Ascorbic Acid
Ag	Silver
AIBN	Azobis(isobutyronitrile)
Au	Gold
BCPs	Block copolymers
B-PGNPs	Block copolymer Grafted Nanoparticles
CH2Cl2	Dichloromethane
CPPA	4-cyano-4-(phenylcarbonothioylthio) pentanoic acid
CTA	Chain Transfer Agent
CTAB	Hexadecyltrimethylammonium bromide
CTAC	Hexadecyltrimethylammonium chloride
DCC	N,N′-dicyclohexylcarbodimide
DLS	Dynamic Light Scattering
DMF	N,N-Dimethylformamide
DPD	Dissipative particle dynamics
Fe3O4	Iron Oxide
GPC	Gel Permeation Chromatography
HAuCl4	Gold (III) chloride trihydrate
H-PGNPs	Homopolymer Grafted Nanoparticles

HVs	Heterogeneous vesicles
ICP-MS	Inductively Coupled Plasma Mass Spectrometry
LSPR	Localized surface plasmon resonance
MAMs	Molecular amphiphiles
M_n	Number-average molecular weight
M-PGNPs	Mixed Polymer Grafted Nanoparticles
MRI	Magnetic resonance imaging
M_w	Molecular weight
m-YSVs	Multi-Yolk Shell Vesicles
$NaBH_4$	Sodium borohydride
NaBr	Sodium Bromide
NCs	Nanocubes
NIR	Near-infrared
NPAM	Nanoparticle amphiphile
NPs	Nanoparticles
NSs	Nanospheres
NTO	Trisoctahedron Nanoparticles
NTR	Transitional Type Nanoparticles
P4VP	Poly(4-vinylpyridine)
PA	Photoacoustic
PAA	Poly(acrylic acid)
PDMS	Polydimethylsiloxane
PEO	Poly(ethylene oxide)

PGNPs	Polymer Grafted Nanoparticles
PMMA	Poly(methyl methacrylate)
PS	Polystyrene
PVs	Patchy vesicles
R_0	Root mean square end-to-end distance
RAFT	Reversible addition-fragmentation chain transfer
R_g	Radius of Gyration
SEM	Scanning electron microscope
SiO2	Silicon dioxide
s-YSVs	Single-Yolk Shell Vesicles
TEM	Transmission electron microscope
TGA	Thermogravimetric Analysis
THF	Tetrahydrofuran
YSVs	Yolk Shell Vesicles

Chapter 1: Introduction

The self-assembly of noble metal NPs is popularly investigated for the potential to advance technologies in biomedicine, energy, and information technologies due to their ability to exhibit a range of unique properties.[1–5] For instance, plasmonic NPs (i.e. Au and Ag) exhibit a special property known as localized surface plasmon resonance (LSPR) when interacting with light. A variety of applications have already taken advantage of such plasmon phenomena because of their large enhancement factors in their optical and/or electromagnetic responses.[6] Such factors can be tailored by varying size, composition, geometry, or environment of NPs.[7,8] Moreover, the plasmonic coupling between nanoparticles can be significantly enhanced by shortening the distance or ordering the spatial arrangement of NPs.[9–11] The aggregation of NPs can potentially result in new absorption bands, for instance, which is not present in induvial NPs.[12] Given the obvious effects of discrete NPs in applications, research interests has shifted towards assembling NPs into more complex nanoarchitectures with enhanced collective properties.

Due to the demand for next generation materials and devices, several bottom-up and top-down strategies have emerged to induce the assembly of building blocks into ordered structures. Top-down techniques (e.g., electron beam & focused-ion lithography) have proven effective at controlling the spatial ordering of nanoscale building blocks over a few hundred nanometers, but these techniques are often expensive and are limited at the tens of nanometer scale.[2] Better control of the nanoscale building blocks location in the assembled structures is needed to fully exploit the collective properties and transform their use in practical applications. In comparison, bottom-up self-assembly is a cost-effective approach that offers more precise control of particles and easier

manipulation of interparticle distances at much smaller length scales (< 10 nm), resulting in more robust assemblies.[13]

A proliferation of research on the self-assembly of NPs has led to the emergence of polymer-grafted inorganic nanoparticles (PGNPs) as strong candidates for controlling the organization of inorganic NPs.[14,15] Significant research studies have shown that tethered polymers are ideal for assembling NPs for several reasons. For instance synthetic polymers can (1) weaken the long-range interaction of NPs to guide their self-assembly since polymer length scales of are comparable to the size of NPs, ~10-70nm[15] (2) preserve the dipole-dipole interactions of NPs, which provides better control of the NP collective properties[11] (3) enable the reversible assembly of nanostructures due to their responsiveness to external stimuli (e.g., light, heat, pH change or acoustic waves)[16]. Thus, self-assembly studies have focused on tailoring the composition, functionalities, and architecture of polymer tethers on NP surfaces to modulate interparticle interactions and facilitate their assembly.

The purpose of this chapter is to provide an overview on the physical characteristic and self-assembly behavior of polymer-grafted inorganic nanoparticles (PGNPs). This introduction will highlight various strategies and techniques for directing the self-assembly of PGNPs into desired structures via interfacial self-assembly, anisotropic self-assembly or co-assembly with additive components. Lastly, this chapter will address the recent advances of PGNP structures self-assembled from plasmonic nanoparticles in modern medical and biological studies.

1.1 Structural Properties of PGNPs

The optical, electronic, and magnetic features of the inorganic NPs and the mechanical strength, flexibility, processability, and dielectric properties of the anchored polymer chains offer

new opportunities for designing novel architectures or enhancing the collective properties of existing NP structures.[17] PGNPs composed of homopolymer, a mix of immiscible polymers, or block copolymer polymer brushes are typically employed in the controlled self-assembly of NPs. In each case, PGNPs can be prepared using "grafting from" or "grafting to" approaches, where polymer grafts replace surface-charged species that stabilize and prevent the aggregation of NPs. This affords PGNPs the ability to self-assemble into a plethora of nanocomposite structures when the short or long-range interparticle interactions are modulated through the interplay of attractive (i.e., van der Waals, hydrogen bonding, other non-covalent interactions) and repulsive (steric and electrostatic) forces.[18]

Due to the tunable, programmable properties PGNPs and the ability to leverage their synthetic versatility, interactions between PGNPS can be manipulated by changing the polymer length, composition or grafting densities (σ), in addition to the particle size and shape, and the dispersion media.[19] Spherical PGNPs dispersed in good solvents exhibit different types of conformation depending on the graft density of polymer brushes when introduced to a poor solvent environment (Figure 1.1).[20] At low grafting densities, the polymer chains are like free chains/random coils and have a so-called 'mushroom' conformation. In this case, there is a relatively low entropic penalty for the lateral phase separation of grafted homopolymer chains as neighboring particles approach each other. As graft density increases, polymer chains are stretched toward the solvent media from the anchor points due to excluded volume effects resulting in the semi-dilute polymer brush (SDPB) conformation. As further increases higher concentrations, polymer chains attain more extended conformations with non-Gaussian characteristics known as the concentrated polymer brush (CPB) regime. In this regime, the distance is much larger between the ends of polymer chains

compared to root segments at the surface and the tip segments can preferentially adopt the SDPB conformation.

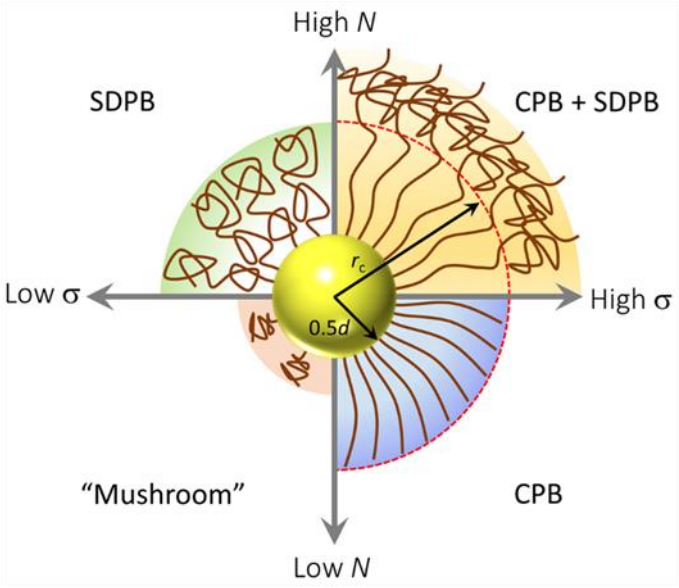

Figure 1.1 Schematic illustration of conformation of polymer brushes on the NP surface. Adapted with permission from ref. 20 (copyright 2018, American Chemical Society).

1.2 Physical Behaviors of PGNPs

When PGNPs are dispersed in a good solvent or compatible polymer matrix (usually identical), interparticle interactions between densely grafted PGNPs are typically repulsive and isotropic due to excluded volume effects arising from the interpenetrating brushes.[17] However, when interactions between the grafted polymer brushes and the surrounding media become unfavorable (*i.e.*, enthalpically incompatible), attractive interactions between PGNPs can occur that promotes aggregation.[21–24] Recent advances in engineering and understanding NP surface chemistry have demonstrated that PGNPs with distinct surface patches or amphiphilic tethers offer unique opportunities to modulate interparticle interactions and increase the hierarchy and complexity of assembly structures.[25] In this case, one can achieve such complex structures by simply relying on

the microphase separation or conformational changes of polymer brushes on the NP surface to direct the self-organization of PGNPs.[26] For example, vesicles with hollow interiors can be fabricated from the re-organization of polymers anchored on NP surfaces. This section will discuss the self-assembly behaviors of PGNPs with different polymer grafts that are typically employed in the controlled self-assembly of NPs, which include 1) homopolymers 2) immiscible mixed-polymers 3) block copolymers.

1.2.1 H-PGNPs

Homopolymer grafted nanoparticles (H-PGNPs) regiospecifically grafted with polymers are an intriguing class of assembly building blocks for designing hierarchical structures.[25,27–29] The distinct and spatially separated chemical regions on the nanoparticle surface impart H-PGNPs with assembly behaviors that can mimic molecular amphiphiles (MAMs).[30] To fully realize this, Kumacheva *et al.* utilized the inherent shape and surface energy anisotropy of "pom-pom"-like gold nanorods for assembling a variety of well-defined nanostructures with desired optical properties (Figure 1.2).[31,32] These prototypical building blocks are structurally analogous to amphiphilic A-B-A type tri-block copolymers, which granted H-PGNPs with stronger directional interparticle interactions. During the synthetic process, thiol-terminated polystyrene (PS) chains were preferentially grafted onto both ends (i.e., the (111) crystal facets) of gold (Au) nanorods, because the longitudinal faces of the nanorods were densely capped with hexadecyltrimethylammonium bromide (CTAB) ligands. The self-assembly of Au nanorods tethered with PS was triggered by adding water (a poor solvent for PS) into a dispersion of the nanorods in various polar organic solvents. Here, the self-assembly process is driven mainly by the association of end-tethered PS chains to reduce the interfacial energy after water is added.

Depending on the composition of the solvent mixture, PS-tethered nanorods assembled into rings, chains, bundles, and vesicles with end-to-end or side-by-side modes of associations. Furthermore, when Au nanorods self-organized into ring with end-to-end arrangements, the plasmonic coupling between NPs could be precisely controlled by varying the PS length. H-PGNPs predesigned with anisotropic surface patches have the potential to self-assemble into hybrid structures with a higher degree of complexity. However, the selective attachment of polymers to certain crystal facets of NPs and surface characterization of resulting PGNPs are rather challenging, thus limiting the feasibility of scalable NP assembly.[14,17]

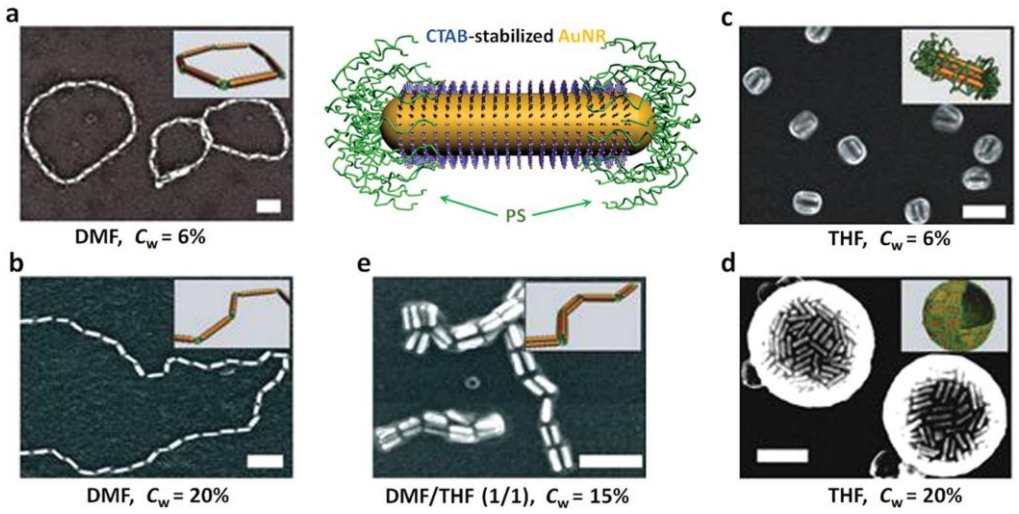

Figure 1.2 Self-assembly of CTAB-stabilized AuNRs tethered with thiol-terminated PS at two ends in selective solvent. The non-solvent is water, the water content (C_w) are different and labeled under SEM images. Scale bars are 100 nm. Adapted with permissions from ref. 30 (copyright 2007, Nature Publishing Group), and ref. 31 (copyright 2008, American Chemical Society).

Several research studies have suggested that regiospecific functionalization of H-PGNPs might not be a necessity to achieve higher-order assembly structures. Deeper insights into H-PGNPs with isotropic surface chemistry revealed that moderately or sparsely grafted H-PGNPs exhibit qualitatively different properties from their densely grafted counterparts. At low grafting

densities, anisotropic interactions can be induced in isotropically-grafted H-PGNPs when their surrounding media is replaced with a polymer matrix, identical PGNPs or a selective solvent. For instance, Akcora et al. discovered that polystyrene tethered silicon dioxide nanoparticles (PS-SiO_2) in a PS homopolymer matrix assembled into unique architectures like strings, sheets, and platelet-like structures, depending on the graft density of PS brushes tethered to SiO_2 NP surfaces.[33] At lower graft densities, microphase separation between the ungrafted inorganic surfaces and the PS matrix is facilitated due to the relatively low entropic cost for polymer tethers to distort as neighboring particles approach each other. Although the range of assembled structures is limited in this approach, this work strongly indicates that sparsely grafted H-PGNPs also have the potential to mimic the self-assembly behavior of MAMs to generate nanostructures with increased hierarchy and complexity. It is promising that one can simply rely on the conformational changes of the polymer brushes of sparsely grafted H-PGNPs to access more complex 2D and 3D nanostructures.

1.2.2 M-PGNPs

Mixed-polymer grafted nanoparticles (M-PGNPs) have frequently been investigated as building blocks in PGNP self-assembly to extend the morphological range PGNP structures and improve the ordering of NPs (Figure 1.3).[34–38] In many cases, amphiphilic binary polymer brushes are used as ligands for the development of surface anisotropy and self-assembly of M-PGNPs into defined nanocomposites in selective solvents.[39–41] The immiscibility between flexible hydrophobic and hydrophilic polymer grafts induces their lateral microphase separation on nanoparticle surfaces into topological patterns, which results in the directional and attractive aggregation of M-PGNPs into thermodynamically favored structures. For example, grafted V-shaped ligands containing one hydrophobic polystyrene (PS) arm and one hydrophilic polyethylene oxide (PEO)

arm stretch and wrap around the surface of tiny gold and silver nanoparticles (~3 nm in diameter) to form a Janus topology during the self-assembly process. The resulting assemblies include rods, long wormlike aggregates, and vesicles that embody the lowest free-energy balance of interfacial tension and entropy loss.[42]

The direction organization of NPs, with mixed immiscible grafts, is determined by the relative size ratio of polymer brushes to the NP core ($2R_g/d$).[36] Researchers have found that the ratio of these parameters strongly dictates the spatial arrangement of inorganic NPs and the degree of lateral-phase separation between immiscible polymers. Song and Cheng *et al.* fabricated hybrid vesicles from Au NPs (~ 14 nm) functionalized with PEO and poly(methyl methacrylate) (PMMA) brushes via film rehydration (Figure 1.3a).[43] The microphase separation between the binary brushes (A & B) triggered the mixed grafts to adopt an "ABA" type deformation on the NP surfaces. More specifically, the hydrophobic PMMA brushes encapsulated the gold cores as a membrane and the hydrophilic PEO brushes served as the outer and inner stabilizing layer. As a result, Au NPs assembled into a monolayer inside the PMMA vesicular membrane. In this study, the relative size ratio between the mixed polymer brushes and the NP core is nearly equal ($2R_g$~1), which permits the Au NPs to contribute positively to the self-assembly of M-PGNPs into vesicle structures. In contrast, complex 3D nanostructures are harder to access when the size ratio of polymer brushes to the NP core is significantly smaller ($2R_g$ <<1). In a following study, it was further reported that amphiphilic M-PGNPs with a larger core size (~ 40 nm) could only self-assemble into dimers. In this case, there is a decrease in the flexibility and deformability of the polymer brushes.[44] Thus, the steric hindrance by PEO brushes and the hydrophobic interactions from PMMA brushes made it challenging for the amphiphilic M-PGNPs to organize into vesicles.

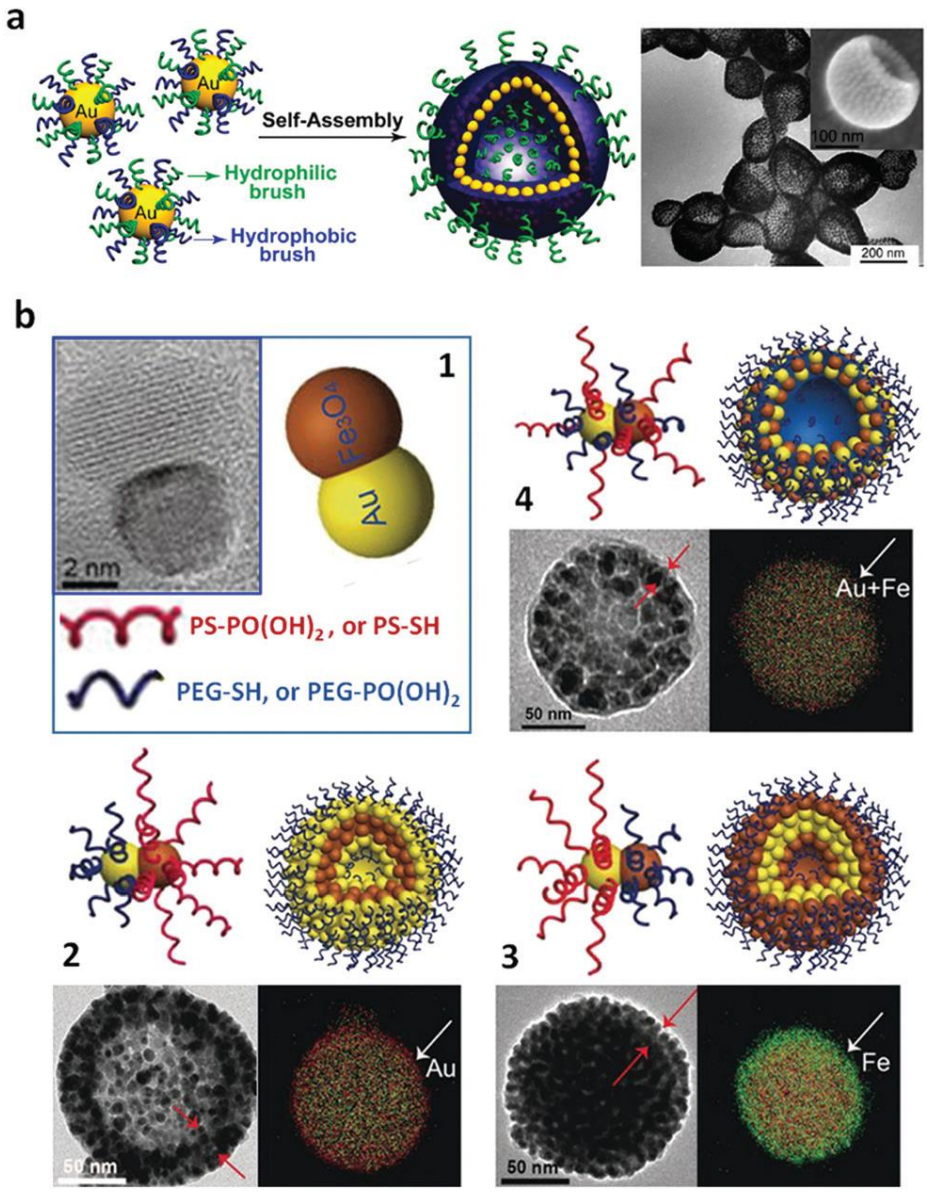

Figure 1.3 Self-assembly of M-PGNPs into vesicles. (a) Schematic and TEM image of hybrid vesicles assembled from 14 nm AuNP capped with mixed PEO/PMMA brushes via film rehydration. Adapted with permission from ref. 43 (copyright 2011, American Chemical Society). (b) Self-assembly of polymer-grafted Janus Au–Fe_3O_4 NPs into magneto-plasmonic vesicles with monolayered or bilayered NPs in the membranes. 1, components of Janus Au–Fe_3O_4 NPs and binary polymer ligands of PEO and PS with different ending groups. 2–4, schematics and TEM images of M-PGNPs and corresponding assembled vesicles: monolayered vesicle (4), bilayered vesicles with Fe_3O_4 components in the membrane center (2) and bilayered vesicles with Au components in the membrane center (3). Adapted with permission from ref 47(copyright 2017, Wiley-VCH).

M-PGNPs can also act as supramolecular amphiphiles and self-assemble into vesicles when M-PGNPs prefer to adopt "AB" type deformation. In this case, the relative size ratio of polymer brushes to NP core is much larger (i.e., $2R_g/d >>1$). Zubarev et al. demonstrated that V-shaped amphiphilic BCPs of poly(ethylene oxide) – *block* – polystyrene (PEO-*b*-PS). could self-assemble into cylindrical core micelles with arrays of Au NPs located at the interface of the hydrophobic PS core and hydrophilic PEO shell.[45] As M-PGNPs adopt "AB" type deformation, the behavior of NP cores is reminiscent of the cores of star-like polymers in good solvent, where Au NPs serve as a crosslinking center to covalently link the laterally phase separated PS and PEO brushes. Consequently, larger NP cores are constrained and become passive due to the crowded polymer brushes shielding the interparticle interactions during assembly. In another case, Moffitt *et al.* found that CDs NPs tethered with mixed brushes of PS and PMMA could self-assemble into vesicles, micelles, and worm-like micelles with a disc-like NP array at the interfaces. The morphological transition of M-PGNP assemblies was dependent on pH and salinity of negatively charged MAA groups in water.[46]

The self-assembly of M-PGNPs allows for control over the collective properties of assembled structures, thus enabling their applications in biological imaging, drug delivery, and therapy. Song *et al.* demonstrated that spherical gold nanoparticles (~ 14 nm) with a mix of hydrophilic PEO and PMMA or PEO and PMMA with 4-vinylpyridine (PMM4VP) chains could self-assemble into monolayer vesicles in water (Figure 1.3b).[47,48] They also showed that vesicles with positively charged walls of P4VP, originating from PEO/PMM4VP functionalized M-PGNPs, spontaneously dissociated into nanoparticles when the pH was reduced, which is a promising route toward pH-triggered drug delivery. The authors further demonstrated that gold nanorods modified with mixed PEO/PMMA brushes could also self-assemble into monolayer vesicles in water, which exhibited

LSPR peak in the NIR range. The vesicle membranes can be disrupted when irradiated with near-infrared light due to the localized heating associated with the excitation of the LSPR of the nanorods, which makes them particularly appealing for use in photothermal therapies. Most recently, Song and Cheng *et al.* observed that asymmetrically functionalized M-PGNPs could also self-organize into unique vesicle structures. They used Janus gold–iron(II,III) oxide nanoparticles, Au-Fe_3O_4 NPs, (~ 12.5 nm in length and 6.5 nm in diameter) capped with binary homopolymer ligands of PEO and PS to assemble into hybrid magneto-plasmonic vesicles.[48] The vesicle morphologies included dual layers of M-PGNPs that were situated at the interface and arranged perpendicularly to the vesicular membrane. The plasmonic coupling between Au NPs and magnetic dipole interaction of Fe_3O_4 within bilayered vesicles drastically enhanced the optical and magnetic properties of the assemblies for cancer imaging.

1.2.3 B-PGNPs

The self-assembly of amphiphilic block copolymer grafted NPs (B-PGNPs) in selective solvents is a versatile strategy to organize PGNPs into ordered structures.[49–51] In aqueous solution, isotropically-grafted block copolymer (BCP) brushes can develop spontaneous anisotropy from conformation changes on the surfaces of NPs which drives their self-assembly into well-defined nanostructures.[52] The morphologies of structures assembled from B-PGNPs can be controlled by changing the chain length of each block in the BCPs or the type of common solvent to dissolve the BCPs. In the former, if the hydrophilic chain length is varied while the hydrophobic segment is held constant, amphiphilic BCPs will adapt to different morphologies to minimize the overall free energy. In the latter, BCPs can change conformations to maximize interactions between the polymers and a good solvent such as tetrahydrofuran (THF) or N,N-dimethylformamide (DMF).

Nie and co-workers have pioneered research studies on the self-assembly of amphiphilic B-PGNPs, also known as nanoparticle amphiphiles (NPAMs). They provide detailed evidence that conformational changes of amphiphilic BCPs govern the anisotropic self-assembly of B-PGNPs into various nanostructures with distinct morphologies (Figure 1.4). For instance, Au NPs functionalized with thiol-terminated polystyrene-*block*-polyethylene oxide (PEO-*b*-PS-SH) self-assembled into vesicles and tubules with a monolayer of hexagonally packed Au NPs.[53] The self-assembly of B-PGNPs was triggered by film rehydration under sonication and the resulting assemblies were mainly controlled by kinetics. First, the BCP brushes on NPs stretched out to minimize the contact between PS chains during rehydration, since the hydrophilic PEO blocks were not dense enough to shield the hydrophobic PS blocks from the surrounding water (Figure 1.4a). This resulted in the formation of several 2D B-PGNP monolayers on top of the substrate, followed by an increase in the local density of PEO blocks between the top two monolayers of B-PGNPs (Figure 1.4b). Lastly, the monolayers of B-PGNPs detached to minimize the line tension, resulting in the formation of different B-PGNP assemblies, which was influenced by the diameter of Au NPs and the molecular weight (M_w) of hydrophobic PS (Figure 1.4b and c). This work highlighted the critical role of the size of NPs and polymer length of B-PGNPs in the formation of assembled structures. However, the film rehydration approach does not allow us fully assess the exact contribution of certain thermodynamic factors (i.e. nature of solvents, structural parameters of B-PGNPs) to the assembly process, since kinetics mainly controlled the formation of structures in this approach.

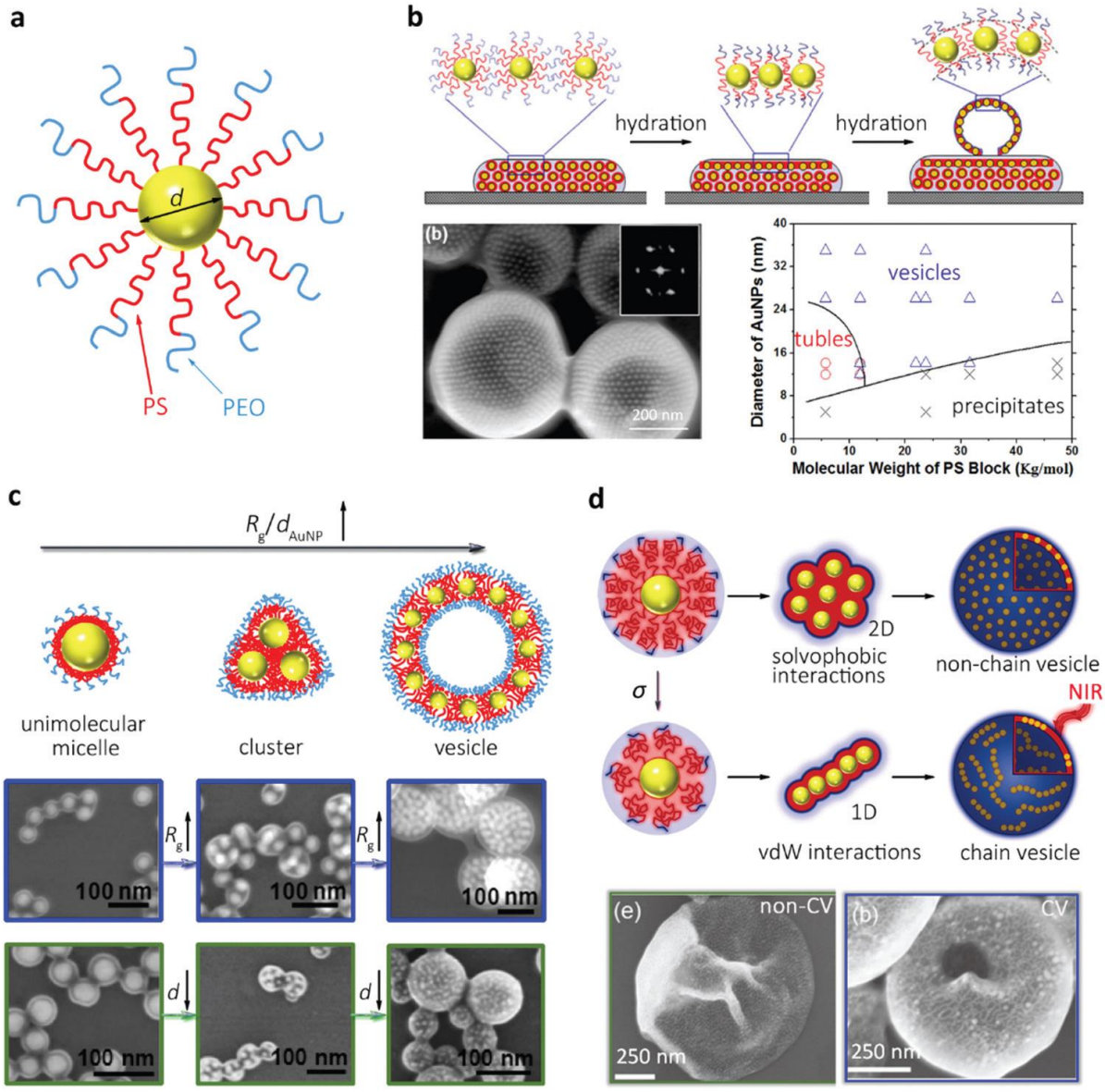

Figure 1.4 Effect of structural parameters of B-PGNPs on their assembly behaviors. (a) Schematic of a B-PGNP consisting of Au NP tethered with PEO-b-PS-SH BCPs. (b) Self-assembly of B-PGNPs via film rehydration. Top: Schematics of the conformational changes of polymer brushes during hydration process. Down panel: Representative SEM image of assembled vesicles with inset of the FFT pattern (left) and a product diagram of the B-PGNP assemblies (right). Adapted with permission from ref. 53 (copyright 2012, American Chemical Society). (c) Effects of Au NP core size d_{Au} and length of PS block (Rg) on the assembly of B-PGNPs in THF/H_2O mixture. Adapted with permission ref. 54 (copyright 2013, American Chemical Society). (d) Effect of s of polymers on the self-assembly of B-PGNPs in THF/H_2O mixture. Schematics reproduced with permission from ref. 55 (copyright 2016, Wiley-VCH).

To gain better insights into the role of critical factors, Nie *et al.* elucidated the effect of B-PGNP structural parameters on their self-assembly behavior in selective solvents. PEO-b-PS grafted Au NPs self-assembled into unimolecular micelles, clusters, or vesicles in THF/water mixtures, depending on the relative size of Au NPs and PS block in BCPs, quantified by the ratio R_g / d_{Au}.[54] In a systematic study accompanied by Dissipative particle dynamics (DPD) simulation, they found that PS chains cannot stretch and compact sufficiently to induce anisotropic conformation at $R_g / d_{Au} > 0.5$ (i.e., low M_w of PS blocks and large Au NP core size), the process yielded only unimolecular micelles. Otherwise, clusters and eventually vesicles are observed as the effective deformability of PS chains on the nanoparticle surfaces increases clusters and eventually vesicles were observed at $R_g / d_{Au} < 0.5$ (i.e., larger M_w of PS blocks and smaller Au NP core sizes). These results provide evidence of the underlying mechanisms of self-assembly and reinforce how instrumental particle deformability in anisotropic self-assembly.

Vesicles structures produced from B-PGNPs with amphiphilic copolymers offer intriguing opportunities for biological imaging. In a follow-up study, Nie *et al.* demonstrated that the lateral phase separation on NP surfaces and the resulting assembly behaviors in vesicular morphologies can be tuned by the graft density (σ).[55] B-PGNPs with relatively higher graft densities (> 0.3 chains/cm^2) assembled into vesicles with uniform distribution of Au NPs in the vesicular membrane. In contrast, B-PGNPs with a lower σ (~0.3 chains/cm^2) first assembled into chains and then vesicles with 1D strings of Au NPs in the vesicular membrane with increasing water content (Figure 1.4d). This two-step mechanism was governed by stronger van der Waals forces between Au NPs originating from the stretching of BCPs as neighboring Au NPs approached each other. Interestingly, chain-like vesicles outperformed vesicles with a uniform distribution of Au NPs in photoacoustic imaging of tumor *in vivo.* The interparticle distances of Au NPs in chain like

vesicles were significantly smaller, which resulted in a much stronger red-shift in the LSPR peaks compared to Au NPs that were uniformly distributed.

Comprehensive studies have shown that inorganic NPs tethered with homopolymers, binary homopolymers, or di-block copolymers could self-assemble into a rich variety of micro- and macro-scaled structures. Research advancements in engineering NP surface chemistry have demonstrated that anisotropic functionalization with single component or mixed homopolymer grafts offers better control in guiding nanoparticles to desired locations, but synthesis processes remain a grand challenge. Fortunately, a more in-depth understanding of the surface characterization of H-PGNPs revealed that anisotropic functionalization is not necessary for the directed organization of PGNPs. The simplicity in isotropic surface chemistry combined with the induced-anisotropic character on NPs surfaces significantly enhances the capabilities of B-PGNPs as building blocks for designing more complex nanostructures readily adaptable for scalable NP assembly. Moreover, the use of amphiphilic BCPs in vivo and in vitro studies is especially attractive for potential use in biomedical applications.

1.3 Co-assembly of PGNPs

Inspired by the self-organization of multiple molecular amphiphiles, the concurrent self-assembly, a.k.a. co-assembly, of PGNPs with other components has garnered much attention for constructing novel nanomaterials with increased complexity and functionality. In many cases, BCPs are used as additive components to design more complex architectures because they offer better control over the spatial distribution and orientations of inorganic nanoparticles in solid/state and solution based PGNP self-assembly.[17] Like individual PGNP assembly, current strategies to control NP locations focus on manipulating polymer brush interactions (i.e., hydrophobic

attraction, steric repulsion, or electrostatic repulsion) between assembly components and the environment. This section will provide an overview of the architectural advancements in assembly systems with one or more PGNPs.

Highly functional hybrid structures can be designed from the co-assembly of H-PGNPs and BCPs confined in emulsion droplets. Jiang and co-workers used the soft confinement of emulsion droplets to co-assemble PS-grafted Au NPs and PS-*b*-P4VP into spherical, pinecone-like, and bud-like scaffolds.[56] The location and alignment of Au NPs was precisely controlled by tailoring the polymer graft type, BCP length and compositions, and ration of surfactants. Upon solvent evaporation, the tunable behaviors of PGNPs resulted in distinct structures with Janus or alternating PS and P4VP regions with Au NPs selectively located at the terminal ends or along the boundaries of the phase domains. Jiang and Zhu et al. also used collapsed emulsion droplets to assemble PS-grafted Au NPs with PS-*b*-P4VP into nanosheets with hexagonally-packed cylindrical patterns. The nanosheets serve as scaffolds to template the organization of PS-grafted inorganic NPs.[57]

The concurrent assembly B-PGNPs and BCPs in solution offers a facile strategy to design unique architectures and morphologies with the controlled location of nanoparticles (Figure 1.5). Liz Maran *et al.* used additional polystyrene-*block*-polyacrylic acid (PS-*b*-PAA) free BCPs to increase the complexity of nanostructures assembled from sparsely grafted H-PGNPs, PS-tethered Au NPs, in solution.[58,59] They fabricated 3D nanoclusters from spherical and dumbbell-shaped Au nanoparticles with exquisite control of particle number, cluster geometry, and orientation in THF/water mixtures. They found that individual H-PGNPs could only self-assemble into 2D clusters at relatively low yields. However, when PS-tethered Au NPs were co-assembled with PS-*b*-PAA, highly uniform and symmetrical 3D bundles were observed after the evaporation of THF

(Figure 1.5a). Here, PS-*b*-PAA copolymers served as stabilizers to protect and confine H-PGNPs after the removal of common solvents, due to an increase in hydrophobicity. Interestingly, Au nanodumbells assembled into dimers with side-by-side arrangements but twisted into unique cross-like structures during the removal of THF (Figure 1.5b).[60] The cross-like configuration was dictated by the rise in mechanical stress within the hydrophobic core of BCP stabilizers.

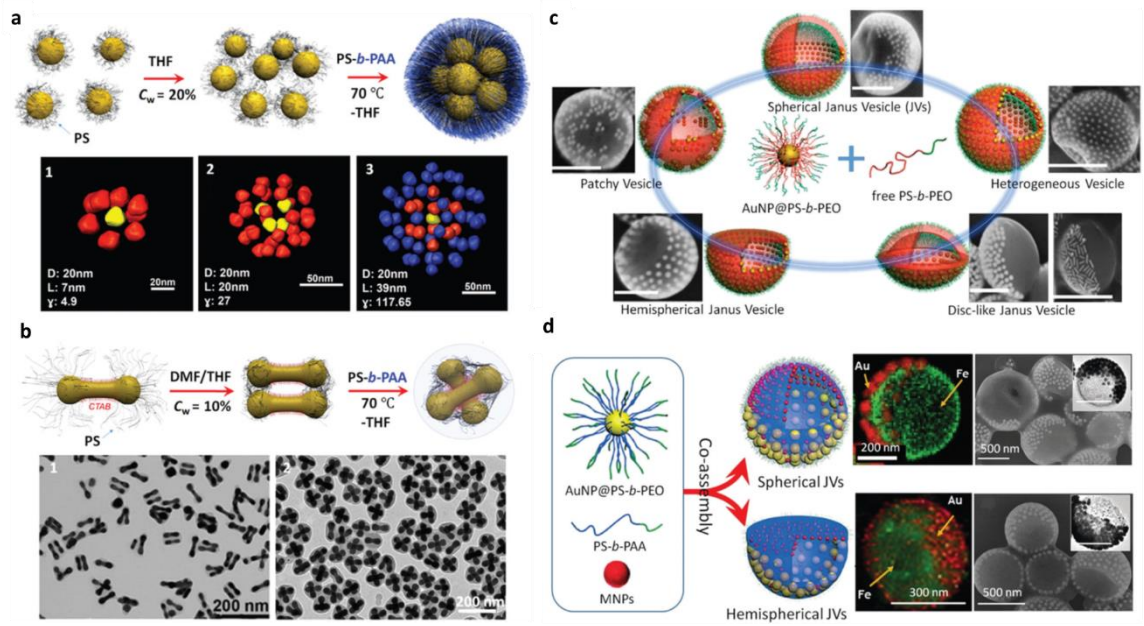

Figure 1.5 Concurrent self-assembly of PGNPs with additive components. (a) Self organization of highly symmetric nanoclusters with PS-tethered AuNPs. Adapted with permissions from ref. 59 (copyright 2014, American Chemical Society) and ref 60 (copyright 2012, American Chemical Society). (b) Self assembly of cross-like Au nanodumbbells. Adapted with permission from ref. 60 (copyright 2012, American Chemical Society). (c) Co-assembly of PS-*b*-PEO grafted AuNPs and free PS-*b*-PEO into hybrid vesicles with different morphologies. Adapted with permission from ref 61 (copyright 2013, American Chemical Society). (d) Co-assembly of PS-*b*-PEO grafted AuNPs, and free PS-*b*-PAA and MNPs into hybrid Janus vesicles with different shapes. Adapted with permission from ref. 62 (copyright 2016, WILEY-VCH).

Hydrophobic interactions are a crucial factor in the self-assembly of PNGPs with hydrophobic homopolymers or amphiphilic polymer brushes. For instance, the hydrophobicity between polymer brushes in solution can endow PGNPs with regiospecific reactivity or induce spontaneous anisotropy on NP surfaces. In aqueous solution, attractive force from the aggregation

of the hydrophobic regions in polymer brushes can combine and/or compete with other types of repulsion forces to drive the self-assembly of NPs into stable, complex structures such as micelles or vesicles. Nie *et al.* utilized the hydrophobicity phenomenon in amphiphilic BCPs to design a rich-variety of functional hybrid vesicles (Figure 1.5c).[61] For example, free amphiphilic BCPs of PS-*b*- PEO and Au NPs tethered with thiol terminated PS-*b*-PEO were co-assembled into different vesicular morphologies including, heterogeneous vesicles with a uniform distribution of Au NPs, patchy vesicles with distinct regions of small Au NPs, and Janus vesicles with two distinct halves. The distinct morphologies depended on the size of spherical Au NPs and M_w of the free and grafted BCPs. Interestingly, the authors observed additional Janus-type assemblies with hemispherical, and disk-like shapes due to the entropy-driven conformational change of free BCP chains stemming from the energetically unfavorable mixing of free polymers and B-PGNPs. The stretching and consequent loss of conformational entropy resulted in a bending modulus and line tension between two distinct halves in the Janus vesicular membranes. In another example, Nie et al. also fabricated functional hybrid vesicles from tertiary mixtures of ligand-stabilized particles, B-PGNPs, and free BCPs.[62] They demonstrated that the concurrent self-assembly of PS-*b*-PEO modified Au NPs, hydrophilic Fe_3O_4 magnetic particles capped with oleic acid, PS-*b*-PAA produced spherical and hemispherical Janus vesicles (Figure 1.5d). B-PGNPs were preferentially segregated and densely packed into one half, while magnetic nanoparticles were uniformly distributed throughout the entire vesicle, resulting in two distinct regions in the vesicular membrane. The membrane thickness was controlled by adjusting the relative weight ratio of free BCPs to B-PGNPs. In this case, the hydrophobicity of magnetic particles was modulated by the PAA blocks of PS-*b*-PAA chains that penetrated into PEO-*b*-PS brushes and binded to the surface

of magnetic nanoparticles. Thus, increasing this ratio resulted in more layers of NPs in the vesicular membrane.

Other than using molecular amphiphiles as additive components, researchers have used mixtures of binary PGNPs to extend the parameter space of co-assembled systems. For instance, Xu and Alivisatos *et al.* extended the range of 2D and 3D superlattice structures that could be produced by using co-crystallization of binary H-PGNPs.[63] They assembled binary nanocrystal superlattices from the PS-tethered Au and Fe_3O_4 NPs at the diethylene glycol/air interface and designed over a wide range of superlattice architectures. It was demonstrated that the extension, interdigitation, and graft density of polymer brushes govern the mechanical behaviors (e.g., elasticity/plasticity) of the superlattices.[64] In another example, Zhu *et al*. used the 3D confinement of emulsion droplets to co-assemble binary H-PGNPs of PS-tethered Au NPs into functional hybrid structures with increased complexity.[65] They found that binary PS-tethered Au NP co-assembled into different core shell structures, depending on the length of PS ligands. H-PGNPs with shorter polymer lengths were more hydrophilic in nature and segregated to the outer layers, while H-PGNPs with longer lengths congregated to form the core. The co-assembly of binary PNGPs is a facile strategy to expand the library of building blocks available in self-assembly, which could drastically increase the functionality of nanocomposites, compared to individual PGNPs.

Impressive progress has been made toward the expansion of accessible nanostructures with unique architectures from the concurrent assembly of multiple building blocks. It has been demonstrated that the co-assembly of PGNPs and BCPs (or binary PGNPs) gives rise to more complex and functional assemblies. Although several combinations of PGNPs and molecular amphiphiles have emerged as model systems for the design of functional hybrid materials, research

focused on the co-assembly of multiple PGNPs remains relatively unexplored. Consequently, the underlying mechanisms are also unclear, due to the increasingly complex interactions from multiple building blocks. Thus, there is an immense opportunity to utilize new multicomponent PGNP systems with precisely controlled interactions that wield novel nanocomposites or more complex collective properties from the existing library of structures.

1.4 Biomedical Applications

Over the last decade, vast amounts of research have focused on improving modern medical and biological applications by developing efficient drug delivery vehicles and contrast agents for biological imaging and therapy.[66–69] Solution-based polymeric nanostructures, largely vesicles, have been widely investigated for use at this frontier. Vesicles assembled from PGNPs offer exceptional potential as drug delivery vehicles, since the hydrophobic core of the vesicles can encapsulate a wide range of therapeutics, including small-molecule drugs, proteins, and nucleic acids.[70] In this case, the polymer brushes provide stability, protection, and controlled release of the encapsulated cargo. Additionally, the surface of the vesicles can be modified with responsive ligands to enable specific delivery to target tissues or cells.[14,71–74] Polymer-grafted nanoparticle vesicles can incorporate imaging agents, such as fluorescent dyes or contrast agents, within their structures, which generally demonstrates the ability of vesicles to enable efficient cellular uptake and localization, allowing for non-invasive imaging of tissues or cells (Figure 1.6). The tunable properties of the vesicles, such as NP size, shape, and surface chemistry determine the interparticle distances, the organization of NPs, and the mutual orientations of anisotropic NPs, which ultimately can further enhance imaging contrast, biodistribution, and targeting specificity.

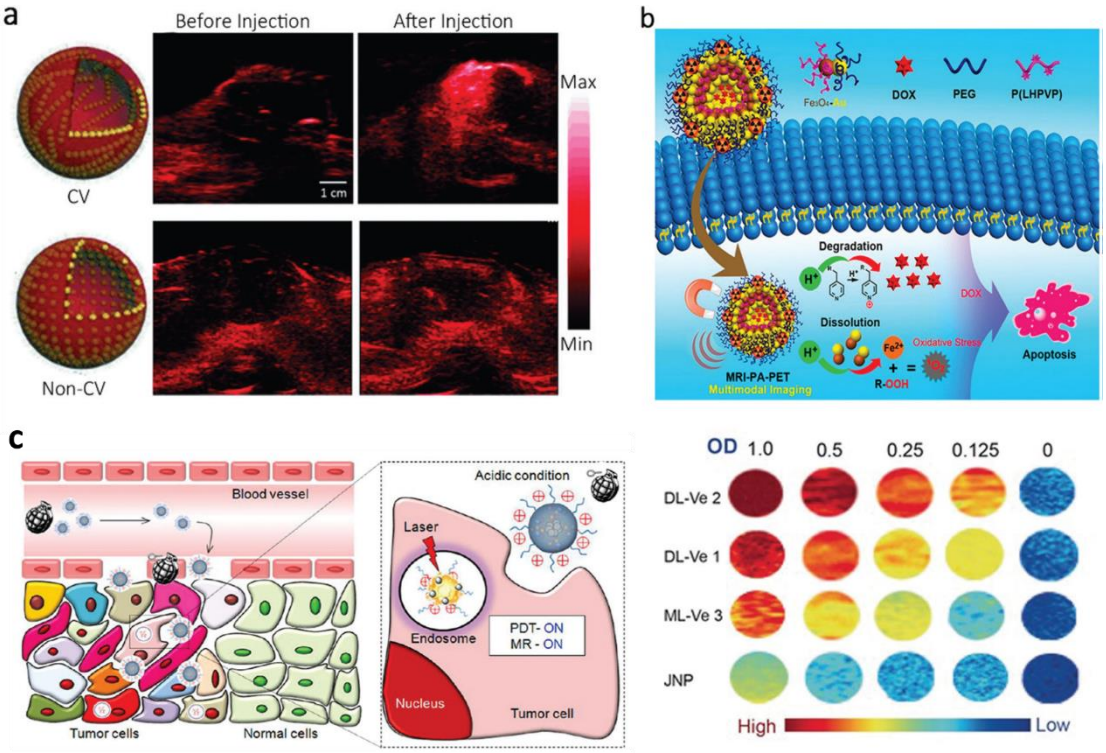

Figure 1.6 Hybrid Vesicles for Biomedical Applications. (a) Co-assembly of PS-b-PEO grafted Au NPs and free PS-b-PEO into hybrid vesicles with different morphologies. Adapted with permission from ref. 55 copyright 2013, American Chemical Society). (b) Co-assembly of PS-b-PEO grafted AuNPs, and free PS-b-PAA and MNPs into hybrid Janus vesicles with different shapes. (top) Adapted with permission from ref. 48 (copyright 2019, American Chemical Society) (bottom) Adapted with permission from ref. 47 (copyright 2017, WILEY-VCH). (c) Schematic representation of tumor pH-recognizable treatment strategy using PMNs. Adapted with permission from ref. 73 (copyright 2014, American Chemical Society).

As previously mentioned, Nie *et al*. demonstrated that chain-like vesicles with 1D strings of Au NPs functionalized with thiol-terminated polystyrene-*b*-polyethylene oxide (PEO-*b*-PS-SH) (~1 nm apart) in the membrane exhibited stronger NIR absorption (~760 nm) than their non-chain like counterparts.[55] This resulted in a tenfold signal enhancement in photoacoustic imaging of tumors *in vivo* (Figure 1.6a). In another case, Chen *et al*. were able to enhance the photoacoustic cancer images *in vivo* by controlling the orientation of the Janus M-PGNPs in magneto-plasmonic vesicles.[47,48] When Au-Fe_3O_4 Janus particles functionalized with PEO-*b*-PS and polystyrene-

block-poly(acrylic acid) (PS-b-PAA), self-assembled into vesicles, their orientation could be manipulated to have either Fe_3O_4 domains or Au domains located in the center-most region of the vesicular membranes. When Au domains were at the center, vesicles exhibited stronger plasmonic coupling between Au NPs, which resulted in and 5 times higher signal enhancement (Figure 1.6b).

Vesicles assembled from polymer-grafted nanoparticles can be engineered to possess combination or synergistic functionalities for therapeutic purposes. For instance, multifunctional vesicles can be designed from the concurrent self-assembly of different building blocks such as, free BCPs and PGNPs or multiple PGNPs.[75] When NP building blocks are designed to respond to external stimuli, such as light or magnetic fields, the controlled release of therapeutic agents or therapeutic responses can be triggered by exposure to NIR light or magnetic fields. For example, Nie *et al.* achieved bi-modal imaging and combination therapy by integrating plasmonic and magnetic nanoparticles into hybrid Janus-like vesicles (~570 nm) via co-assembly of hydrophobic Fe_3O_4 MNPs, amphiphilic block copolymer of PS-*b*-PAA, and AuNPs grafted with PEO-*b*-PS-SH.[62] Hemispherical JVs containing 50 nm AuNPs and 15 nm MNPs exhibited strong NIR absorption in the 600nm – 700 nm range and enhanced the transverse relaxation (T_2) contrast effects. An external magnetic field was used to guide the vesicles with payloads to accumulate at target sites, which drastically enhanced the photoacoustic (PA) and magnetic resonance (MR) imaging signals in tumors. Subsequently, NIR light was applied to control the release of drug payloads.

Vesicles can also be programmed to release drug payloads when polymeric components are responsive to external stimuli. For example, Hyeon *et al.* used binary pH-responsive binary BCPs to improve the localized delivery of magnetic nanoparticles to tumors (Figure 1.6c).[73] To achieve this, they designed pH-sensitive magnetic "nanogrenade" structures by co-assembling

extremely small iron oxide NPs (~3 nm) and chlorin e6 (Ce6) grafted poly(ethylene glycol)–poly(β-benzyl-l-aspartate) (PEG-PBLA-Ce6). As the hybrid structures approached the acid tumor sites, BCPs underwent a surface-charge reversal in response to the change in pH (~6.8) in the vicinity of the tumor. This triggered he disassembly of the nanogrenade structures and subsequently enhanced the magnetic resonance imaging contrast, fluorescence signal, and photodynamic activity at the target site.

Hybrid vesicles assembled from polymer-grafted gold nanoparticles have shown promise in a range of biomedical applications and are an active area of research. The ability to tailor the properties of the vesicles, such as size, surface chemistry, and cargo encapsulation, makes them highly adaptable and suitable for specific biomedical needs. However, there is a rising demand for next-generation nanocomposites designed from complex structures with new functionalities. Recent advances in nanoscience have shown that PGNPs with anisotropic shapes (i.e. rods, cubes, etc.) are promising building blocks for generating hybrid nanocomposites that could fulfill this demand.[76–79]

1.5 Scope of the Dissertation

As discussed in the previous sections, individual self-assembly and concurrent assembly of polymer-guided inorganic nanoparticles have emerged as important routes for the advancement of nanotechnology in biomedicine. Since current research studies are still in the early stages of development, successes at this frontier are limited and do not meet the rising demand for the next generation of functional materials and nanodevices. More specifically, researchers must gain a better understanding of the stability of hybrid assemblies and PGNP assembly behavior before newer systems can be upscaled for wide-scale production. Given the recent advances in the

synthetic design of gold nanoparticles with diverse geometries and BCPs with excellent controllability and complexity, the library of available building blocks has vastly increased and offers exciting opportunities for assembling structures with novel morphologies and advanced functionalities.

I have chosen gold nanoparticles grafted with amphiphilic block copolymers as building blocks for self-assembly, due to i) the unique intrinsic features of Au NPs including biocompatibility due to low toxicity and excellent surface stability for easy surface modification, ii) the soft shell interactions from the lateral diffusion of polymer ligands that can direct and control the assembly behavior of nanoparticles and iii) potential to expand the library of functional assembled structures and exploit new optical properties from the synergetic effect between BCPs and anisotropic NPs.

The objective of this dissertation is to explore: i) the self-assembly of individual B-PGNPs with anisotropic characteristics derived from the NP geometry ii) the co-assembly of B-PGNPs with distinct geometries and dimensions iii) the effect of PGNP tunable parameters (such as particle size, polymer length, particle shape, and building block combinations) on assembly behavior and resulting collective properties.

Chapter 2 describes the solution-based self-assembly of amphiphilic B-PGNPs with anisotropic shapes into 3D superstructures. The assembly process was triggered by dialyzing a solution of B-PGNPs in THF against deionized water. The versatility of the approach was explored for various anisotropic nanoparticles including cubic and trisoctahedron geometries. The size of NPs and length of BCPs were tuned to study their assembly behavior and influence on the formation of 3D nanostructures. Temperature annealing was conducted on vesicle structures in solution to study its effect on the transition in packing arrangements and aggregations of B-PGNPs with cubic shapes. To reveal any behavioral changes or lack thereof, SEM images and UV-Vis

spectra of the assembly after dialysis (25 ℃'), immediately after heating (50 ℃), and after cooling back to room temperature (25 ℃'') were compared. Statistical analysis was also performed to examine the robustness of vesicle structures after thermal treatment.

Chapter 3 explores the concurrent self-assembly of binary B-PGNPs with distinct sizes and shapes into hybrid vesicles. The volume fraction of building blocks and the BCP lengths were tuned to study their effect on the morphology of vesicle structures. Binary mixtures of B-PGNPs comprising spherical AuNPs with different size dimensions and/or shapes co-assembled into hybrid vesicles with distinct phase-separated regions.

Chapter 4 presents a systematic study on the formation of hybrid vesicles from the co-assembly of binary B-PGNPs with distinct sizes of spherical Au NPs. Depending on the size and relative molar concentration of B-PGNPs in solution, B-PGNPs are segregated laterally within or vertically from the membrane leading to different morphologies such as patchy and yolk/shell. A kinetic study was conducted to further understand the size segregation behavior of NPAMs that assemble into yolk/shell vesicles.

In Chapter 5, a summary of the completed work done in this dissertation is provided, along with recommendations for future work.

Chapter 2: Self-Assembly of Polymer Grafted Nanoparticles with Anisotropic Shape

Overview. Tremendous research efforts have focused on the self-assembly of spherical plasmonic nanoparticles and their controlled organization. However, little progress has been achieved in the controlled assembly of anisotropic NPs (i.e. non-spherical shaped NPs) into condensed structures with multiple hierarchy levels. Here we demonstrate the fabrication of hybrid vesicles from the self-assembly of B-PGNPs with anisotropic shape, which utilizes thermodynamically driven segregation of BCP polymer ligands on NP surfaces after a change in solvent quality. The resulting aggregations of anisotropic B-PGNPs was accompanied by a significant red shift in the LSPR peaks before and after dialysis. The versatility of the strategy is demonstrated for B-PGNPs with different NP shapes and sizes tethered with various lengths of polymers. In cubic-PGNP vesicle assemblies, unique transformations and optical properties were induced by thermal stimuli after the self-assembly. These hybrid vesicles have potential applications in fundamental research, diagnostics, sensing, and therapeutics.

2.1 Introduction

In the field of nanoscience, new materials with desired and tunable properties from plasmonic nanoparticle building blocks are highly sought after to program responsive, multifunctional assembly structures. It is well known that the light-matter interactions in plasmonic nanomaterials can be controlled by the shape of the nanoparticles, in addition to the NP size and properties of the surrounding medium.[80] In recent years, significant progress has been achieved in the development of plasmonic assemblies with enhanced collective, but the preparation of highly sophisticated and complex architectures requires multistep chemical functionalization in

many cases. To accelerate the development of next-generation plasmonic materials, straightforward strategies that can produce targeted assembly structures are needed. The exploration of non-spherical nanoparticles as building blocks in the self-assembly of PGNPs in solution is a feasible approach to controlling the self-assembly of plasmonic nanoparticles. Moreover, the organization of non-spherical nanoparticles in close proximity can induce unprecedented optical phenomena due to dramatic nearfield enhancements from sharp vertices and edges.[81]

Controlled assembly of anisotropic NPs into ensembles with increased complexity and hierarchy is crucial to discover their collective properties and potential uses in nanomedicine or other applications. This chapter presents an experimental investigation of the solution-based self-assembly of B-PGNPs composed of gold nanoparticles with anisotropic shape and the resulting optical properties of assembled structures. B-PGNPs were designed to have thiol-terminated polystyrene-*b*-polyethylene oxide (PEO-*b*-PS-SH) grafted to Au NP surfaces so the outer PEO blocks could provide the outer structures' steric stabilization and the deformability of the inner PS blocks could enable the assembly of NPAMs into hierarchical structures. Experimentally, we varied the BCP length, NP size, and initial BCP concentration to understand the effects on the self-assembly behavior and determine the optimal conditions for the formation of hybrid vesicles. The PEO chains were kept relatively short compared to PS chain to ensure that the hydrophobic effect is the major driving force during self-assembly. Cubic Au nanoparticles were mainly used as a model system to understand the self-assembly behavior of anisotropic nanoparticles, but the versatility of the approach was explored for trisoctahedron and transitional-type nanoparticles. B-PGNPs with different dimensions and geometric shapes self-assembled into hybrid vesicles that exhibited stronger LSPR absorption peaks in the NIR window compared to spherical NPs. With

the increase of temperature, the B-PGNPs disassembled and permitted vesicles structures to re-assemble as the temperature of solutions cooled back down to room temperature. Interestingly, the thermal treatment of vesicles comprising cubic B-PGNPs resulted in a noticeable improvement in the appearance and overall quality of the assembled structures and unique optical properties at longer wavelengths.

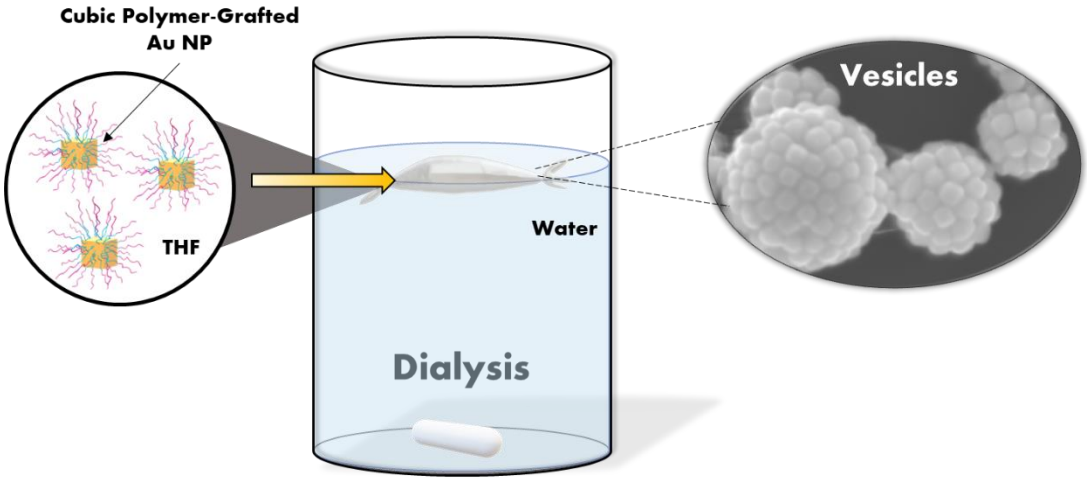

Figure 2.1 Schematic Illustration of the experimental setup for the self-assembly of anisotropic B-PGNPs into vesicles in solution via the dialysis method.

2.2 Experiments

2.2.1 Materials

Styrene, azobis(isobutyronitrile) (AIBN), 4-cyano- 4-(phenylcarbonothioylthio) pentanoic acid (CPPA), tetrahydrofuran (THF), dimethylformamide (DMF), Gold(III) chloride trihydrate (HAuCl4.3H2O, ≥ 99.9%), ascorbic acid (AA, ≥ 99.0%), sodium borohydride (NaBH4, 98%), sodium bromide (NaBr, ≥ 99.0%), cetyltri- methylammonium bromide (CTAB, 3 99%), and cetyltrimethyl- ammonium chloride (CTAC, 25 wt% in water) were all obtained from Sigma-Aldrich and used as received. Deionized water (HPLC grade) from Fisher Scientific was used for

all solution for the preparation of gold nanoparticles and assembly experiments. Polystyrene-b-poly (ethylene oxide) (PS-*b*-PEO) without functional groups was purchased from Polymer Source, Inc. Styrene was distilled under vacuum prior to use and stored in a freezer at −20 °C. AIBN was recrystallized from ethanol.

2.2.2 Synthesis of thiol-Terminated BCPs

Thiol-terminated PS-b-PEO with different molecular weights were synthesized using reversible addition fragmentation chain transfer (RAFT) polymerization reported previously. [53]

Synthesis of PEO macroRAFT chain transfer agent (PEO-CTA). To synthesize the chain transfer agent, PEO-CTA, CPPA was attached to PEO by esterification. A reaction mixture of monofunctionalized PEO45-OH (4g, 2mmol), CPPA (837 mg, 3 mmol), DCC (618 mg, 3mmol), 4- (dimethylamino)pyridine (61 mg, 0.5 mmol), and anhydrous CH_2Cl_2 was stirred under nitrogen at 0 °C and precipitated out in cooled ethyl ether. The final product was dried under vacuum for 24 h.

Synthesis of thiol-terminated BCPs of PEO-b-PS. BCPs of PEO-b-PS were synthesized by using PEO-CTA as the initial block to make CTA-PS-*b*-PEO. PEO-CTA, Styrene, and AIBN (molar ratio of 500:1:0.2) were dissolved in dioxane, degassed under vacuum for 30 minutes using nitrogen. The reaction was placed in an oil bath at 85 °C for 20 h and quenched by cooling in liquid nitrogen. After polymerization, the polymer was precipitated in hexane and THF three times and dried under vacuum for 24 h. By varying the amount of PEO-CTA, we synthesized BCPs of PEO-*b*-PS with different PS block lengths. To obtain thiol-terminated polymers, CTA-PS-*b*-PEO was mixed with THF and excess n-butylamine under nitrogen for 2 h. The polymer was precipitated in

water and ethanol twice and dried under vacuum for 24 h. The characterization details can be found below in Chapter 3 (see Table 3.3 in section 2.3.2).

2.2.3 Synthesis of Anisotropic Gold Nanoparticles

Au NPs were synthesized using a seed-mediated growth approach.[82]

Preparation of Gold Seed Solution. A 0.02 M $NaBH_4$ solution in 10 mL water was prepared and left on ice for 30 minutes. While the solution was cooling, a 10 mL aqueous solution containing 2.5×10^{-4} M $HAuCl_4$ and 0.1 M CTAC was prepared in a 20 mL vial. The ice-cold $NaBH_4$ solution (0.45 mL) was added to the mixture. The resulting solution, which quickly turned brown, was stirred for 2 minutes at 600 rpm. The seed solution was left undisturbed for 55 minutes in a 30 °C water bath. During that time, the growth solutions were prepared for the synthesis of non-spherical gold nanoparticles.

Preparation of Non-Spherical Gold Nanoparticles. Two growth solutions were prepared in 20 mL vials and labeled vials A and B. In each vial, 0.3202 g of CTAC was dissolved in a specific volume of water depending on the target shape (see Table 2.2). Both vials were incubated for at least 20 minutes in a water bath set at 30°C, except for 60 nm Au NCs which were kept at 25°C. Concurrently, two 10 mL aqueous solutions of 0.01 M $HAuCl_4$ and 0.01 M NaBr were prepared and set aside, in addition to a 5 mL solution of 0.04 M AA. To prepare the growth solutions, 250 μL of 0.01M $HAuCl_4$ solution and 10 μL of 0.01 M NaBr solution was added to both vials and mixed. Lastly, a specific volume of 0.04 M AA (see Table 2.1) was added to the mixtures and the solution color turned clear. Both vials of growth solutions were placed back in the water bath and incubated for at least 15 minutes.

Depending on the targeted size of the nanoparticle, a specific volume of seed solution was added to the solution in vial A (see Table 2.1) while gently swirling the vial for approximately 50 seconds until the solution completely turned light pink. Next, 25 uL of the solution in vial A was added to the solution in vial B and thoroughly mixed for roughly 10 seconds. The vial B growth solution was then left undisturbed for 15-20 minutes in the water bath. Lastly, the final product was centrifuged and re-dispersed in 10 mL water. It is important to mention that the temperature of the growth solution was reduced from 30 ℃ to 25 ℃ to produce Au NC with an average face length of 60 nm. Otherwise, a transitional-type shape with protruding surfaces was observed, as shown in section 2.3.1 (Figure 2.1d).

Table 2.1 Experimental parameters for the preparation of anisotropic Au NPs.

Au NP Shape	Size (nm)	Volume Water (µL)	Volume AA (µL)	Volume Seed (µL)	Centrifugation Speed (rpm)	Centrifugation Time (min)
Cube	60	9625	85	100	6,500	10
	70		85	65	3,000	10
	90		90	25	3,000	8
Transitional Product	60	9625	90	120	6,500	10
Trisoctahedron	60	9625	90	110	6,500	10
	90	9605	110	25	3,000	8

2.2.4 Synthesis of Gold Nanospheres

~60 nm Au NPs were synthesized using a successive, seed-mediated growth of single-crystal nanospheres.[83] A fresh aqueous $NaBH_4$ solution (10×10^{-3} M, 0.6 mL) was rapidly added into a thoroughly mixed 10-mL aqueous solution containing $HAuCl_4$ (0.25×10^{-3} M) and CTAB (100×10^{-3} M) using a pipette. The solution immediately turned brown upon the introduction of $NaBH_4$ while stirring at a speed of 300 rpm for two minutes. Finally, the solution was kept

undisturbed at room temperature for three hours to ensure the complete decomposition of $NaBH_4$ remaining in the reaction mixture. The product was collected by centrifugation at 14,500 rpm for 30 minutes, and then washed with water once for further use and characterization. The 15-nm Au nanospheres were dispersed in 5 mL of aqueous CTAC solution (0.02 M) after washing, which was used as seeds in the second round of growth. An aqueous solution of CTAC (0.1 M, 25 mL) and 23 mL of water were mixed in a glass jar, followed by the addition of AA (10×10^{-3} M, 130 μL) and 75 uL of seed solution. Lastly, an aqueous solution of $HAuCl_4$ (6.25×10−3 M, 2 mL) was added dropwise to the mixture using a syringe pump at an injection rate of 2 mL/h. The reaction proceeded to stir at room temperature for 10 min after the injection had been finished. The final product was collected by centrifugation at 12,00 rpm for 15 minutes and washed with water once for characterization.

2.2.5 Surface Modification and Self-Assembly of Gold NPs with Copolymers

0.1 – 2.5 mg of thiol-terminated copolymers were dissolved in 10 mL of dimethylformamide (DMF). A 10 mL aqueous solution of AuNPs was concentrated into 100 μL by centrifuging. The concentrated AuNP solution was slowly added to the copolymer solution in DMF while shaking. Subsequently, the mixture was sonicated for 1 h to avoid aggregation. Non-spherical particles and spherical particles were kept undisturbed for 1 hr and 3 hr, respectively, to complete the ligand exchange. The solution was centrifuged 6-8 times and re-dispersed in 1.5 mL of solvent to remove free BCPs from the solution. The first 1-2 cycles used DMF to prevent aggregation. Then, the particles were re-dispersed in THF after centrifugation four times. The resulting copolymer-grafted AuNPs were redispersed in 0.25 mL – 1.5 mL THF. For self-assembly, the solution of copolymer-grafted AuNPs was transferred to a dialysis bag and dialyzed

against water in a 2-Liter container for 24 hours to remove THF. Nanoparticle amphiphiles dispersed in THF were transferred to a dialysis bag and placed in a large container of water. The surrounding water gradually diffused into the dialysis bag and replaced the THF, which triggered the self-assembly of B-PGNPs. We acquired SEM images to confirm the formation of 3D assembly and determine the morphology of the assembled structures. SEM images were used to determine whether the vesicle-like structures were hollow. UV-Visible spectra were used to determine the absorption maximum of the assembled structures.

2.2.6 Temperature Annealing of Assembly Structures

Self-assembly experiments were conducted for 0.75 mL solutions of gold nanocubes modified with thiol-terminated PEO_{45}-b-PS_{130} (C_{BCP} = 0.02 and 0.6 mg/mL). Immediately after 24 hours of dialysis, solutions containing the assembled NPAMs were transferred to small vials. The vials were sealed and maintained at 50 ℃ for 30 minutes in water bath. The resulting assembly solutions were prepared for SEM and evaluated by UV-Vis Spectroscopy after dialysis, thermal treatment, and cooling back down to room temperature.

2.2.7 Characterizations

^{1}H NMR. ^{1}H NMR spectra were recorded using Bruker AV-400 MHz high-resolution NMR spectrometer.

SEM imaging. Individual Au NPs before and after surface modification and their resulting assembly structures were imaged using a Hitachi SU-70 Schottky field emission gun Scanning Electron Microscope (FEG-SEM). Samples for SEM were prepared by drying 3-4 μL of an aqueous solution of assembly structures on silicon wafers at room temperature.

UV-Vis Absorption Spectroscopy. The extinction spectra of individual Au NPs, functionalized Au NPs, and the resulting assembly structures were taken on a PERKIN LAMBDA 35 UV/Vis System.

2.3 Results and Discussion

2.3.1 Preparation of Anisotropic Building Blocks for Self-Assembly

Before the assembly process, it was crucial to produce monodisperse nanoparticles for the intricate design of 3D nanostructures. Figure 2.2 shows representative SEM images of the various geometric shapes of the gold anisotropic nanoparticle building blocks prepared for self-assembly in this study. Using a previously reported method, CTAC-stabilized cubic (NC), trioctahedral (NTO) nanoparticles, and their intermediate products termed transitional nanoparticles (NTR) (~60 – 100 nm) were synthesized using a multi-step, seed-mediated sequence. Depending on the targeted size and shape, slight medications had to be made to the volume of AA and seed solution to produce high-quality nanocrystals (section 2.2.3, Table 2.1). Analysis of SEM images along with UV-Vis spectroscopy was used to verify the structural and optical characteristics of each building block. SEM images in Figure 2.2 (a-f) show that each morphology of Au NPs is quite uniform in size and shape. Moreover, the particles maintain sharp corners with decreasing size. These observations were also validated by relatively narrow bands in UV-Vis absorption spectra of the gold particles. The surface plasmon resonance (SPR) absorption band maxima in Figure 2.2g for 60 nm, 70 nm, and 90 nm Au NC are at 551 nm, 560 nm, and 596 nm, respectively. Due to their larger sizes from protrusions on the NP surface, Au NTR, ~ 60 nm in size, shows an SPR peak at 560 nm, while SPR peaks for ~60 nm and ~100 nm Au NTO were at 570 nm and 621 nm, respectively (Figure 2.2h). During synthetic procedures, the reproduction of Au NPs with

anisotropic geometries was challenging, and samples were frequently susceptible to producing Au nanocrystals with broad shape and size distributions. To reduce the risk of error in characterizing and understanding the assembly behavior, ~60 nm Au NCs were primarily used throughout this work.

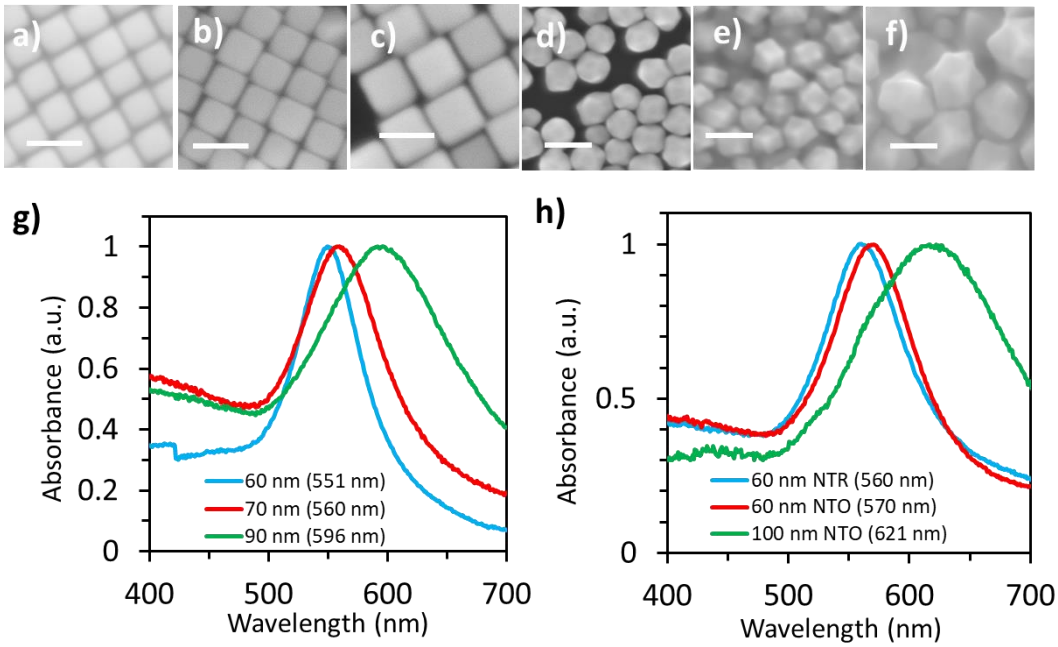

Figure 2.2 Representative SEM images of synthesized anisotropic nanoparticles with various targeted shapes and dimensions including (a) 60 nm (b) 70 nm (c) 90 nanocubes, (d) 60 nm transitional nanoparticles, and (e) 60 nm and (f) 100 nm trisoctahedron nanoparticles. Corresponding UV-Vis spectra for (g) nanocubes and (h) transitional and trisoctahedron nanoparticles. All scale bars are 100 nm.

Anisotropic NPs with different shapes and dimensions were tethered with various lengths of amphiphilic copolymers. All Au NPs throughout this work were functionalized with amphiphilic thiol-terminated polystyrene – *block* – poly (ethylene oxide) (PEO-*b*-PS-SH) using the solution ligand exchange approach (Figure 2.3a). To remove excess untethered BCPs, solutions were centrifuged and washed with THF for several cycles. The resulting solutions of B-PGNPs

were concentrated to a predetermined volume of THF that was optimal for self-assembly. To confirm the grafting of polymers to the NP surfaces, UV-Vis spectroscopy was used to characterize the Au NPs before and after the surface modification. Using 60 nm Au NCs grafted with thiol-terminated PS_{300}-b-PEO_{45} as an example, the UV-Vis spectra in Figure 2.3b exhibited a slight red shift (~ 13 nm) in the SPR peaks after surface modification due to the increase in particle sizes from the grafting of BCPs on the Au NP surfaces. Furthermore, SEM images in Figure 2.3c confirm the capping of polymer shells around the metallic core of Au NCs.

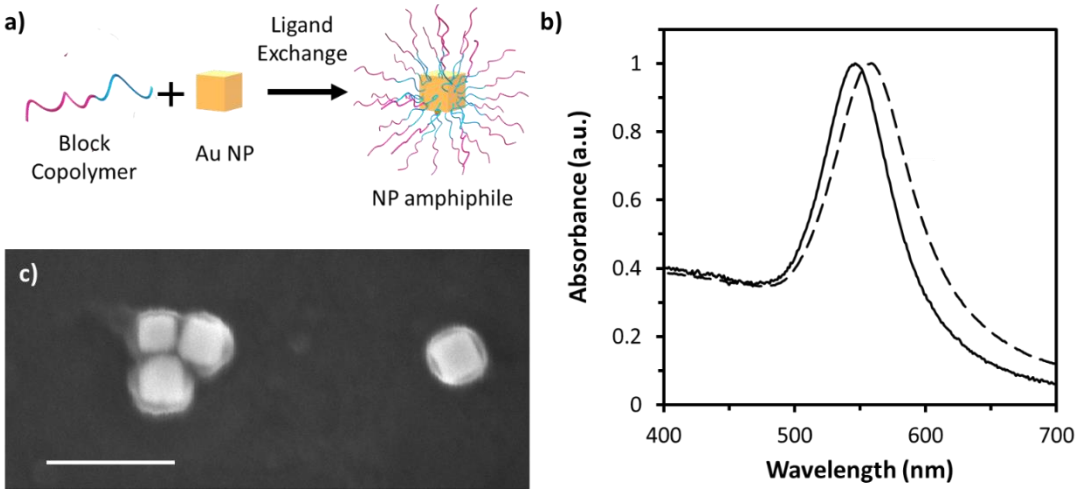

Figure 2.3 (a) Schematic illustration of the formation of amphiphilic nanoparticles via ligand exchange (b) Representative UV-Vis spectra of 60 nm Au NCs before and after surface modification with copolymer ligand $PEO_{45} - b - PS_{341}$. (c) Representative SEM image of the cubic B-PGNPs prepared with PEO_{45}-PS_{300} copolymer ligands. Scale bars: 200 nm.

2.3.2 Self-assembly of B-PGNPs into Vesicles

Anisotropic NPs with different shapes and dimensions, which were tethered with various lengths of amphiphilic copolymers, self-assembled into an array of 2D and 3D structures in solution, but the vesicle morphology was mainly observed. For instance, the self-assembly of Au NCs grafted with PEO-*b*-PS copolymers produced well-defined vesicles with average diameter

sizes measured as low as 200 nm with lengths up to several micrometers. SEM images in Figure 2.4a-d present vesicle structures produced from 60 nm Au NCs modified with PEO_{45}-*b*-PS_{130}-SH. It can be seen from the visibly buckled and broken vesicles that the vesicle structures are hollow in nature (Figure 2.4c and d). The wrinkling of the membranes is common in giant vesicles and is attributed to the surface collapsing under drying conditions. Analysis of SEM images showed that hexagonal geometric configurations (6-membered rings) were common amongst different-sized vesicles. However, higher-order packing configurations, like heptagonal orientations (7-membered rings) or disordered packing, where uniform arrangements of Au NPs are disrupted, were observed for vesicles with relatively larger dimensions (~ 400 nm or greater).

The self-assembly of anisotropic PGNPs was triggered by dialyzing a solution of the modified particles in THF against water to remove the organic solvent. After the addition of water to well-dispersed solutions of 60 nm Au NCs functionalized with PEO_{45}-*b*-PS_{130}-SH, we observed a color change from pink to dark pink indicating the aggregation of Au NPs. After 24 hours, the solution eventually turned slightly opaque or clear, which signaled the formation of the final assembly structures (Figure 2.4e). The color change was accompanied by a noticeable increase in the SPR peaks to longer wavelengths for the Au NCs in vesicle assemblies compared to their dispersed states. For instance, the absorption bands of ~ 60 nm Au NCs before and after surface modification with different lengths of thiol-terminated copolymers exhibited narrow absorption bands with SPR peaks below 600 nm. After self-assembly, the UV- Vis spectra show a broad absorption band maxima at 686 nm (Figure 2.4f). Similar trends were observed for the self-assembly of larger anisotropic Au NCs and other shapes modified with various lengths of BCPs.

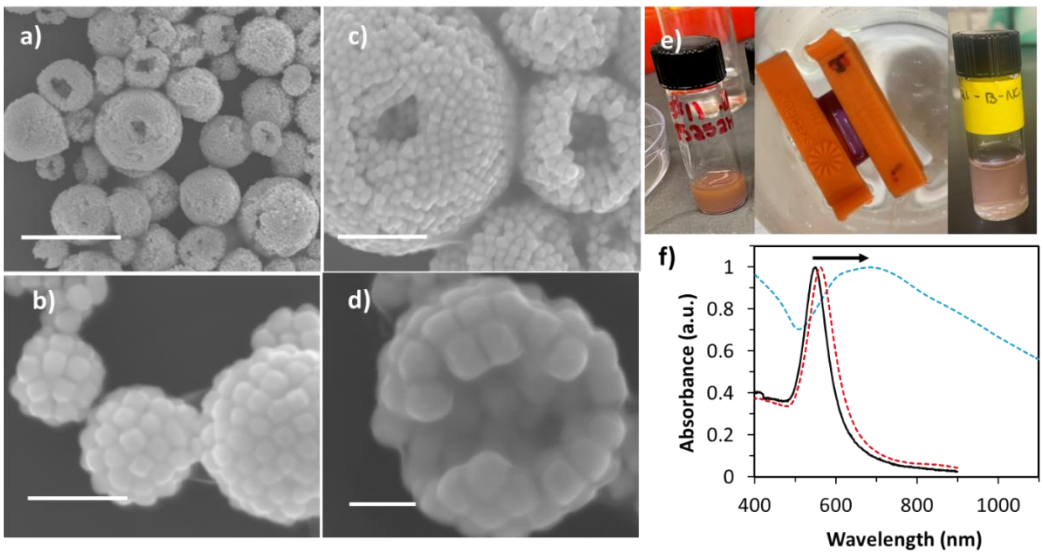

Figure 2.4 (a-d) Representative SEM images of in-tact (Left) and broken vesicles (Right) produced from the self-assembly of 60 nm Au NCs modified PEO_{45}-*b*-PS_{300}. Scale bars: 2 μm (a), 300 nm (b), 500 nm (c) 100 nm (d). (e,f). (e) Representative images of changes in solution color before, during, and after dialysis (from left to right). (f) UV-Vis spectra of individual CTAC-stabilized Au NCs, BCP-modified Au NCs in THF, and assembled Au NCs after dialysis against water.

Interestingly, the self-assembly of tethered Au NTOs (~100 nm), produced vesicle structures with unique geometric frustrations. In addition to the typical spherical geometry, SEM images in Figure 2.5 show elongated oval-shaped and heart-shaped structures produced from the self-assembly Au NTO tethered with PEO_{45}-*b*-PS_{300} (Figure 2.5b1-3) and PEO_{82}-*b*-PS_{652} (Figure 2.5c1-3), respectively. In each case, the SPR peaks shifted from having one peak around 635 nm before assembly to having two plasmonic bands around 600 nm (shoulder peak) and 730 nm after assembly (Figure 2.5d and e). The splitting in SPR could be the result of plasmon hybridization from the symmetric and asymmetric plasmon coupling between Au NPs in the vesicle shell.[13]

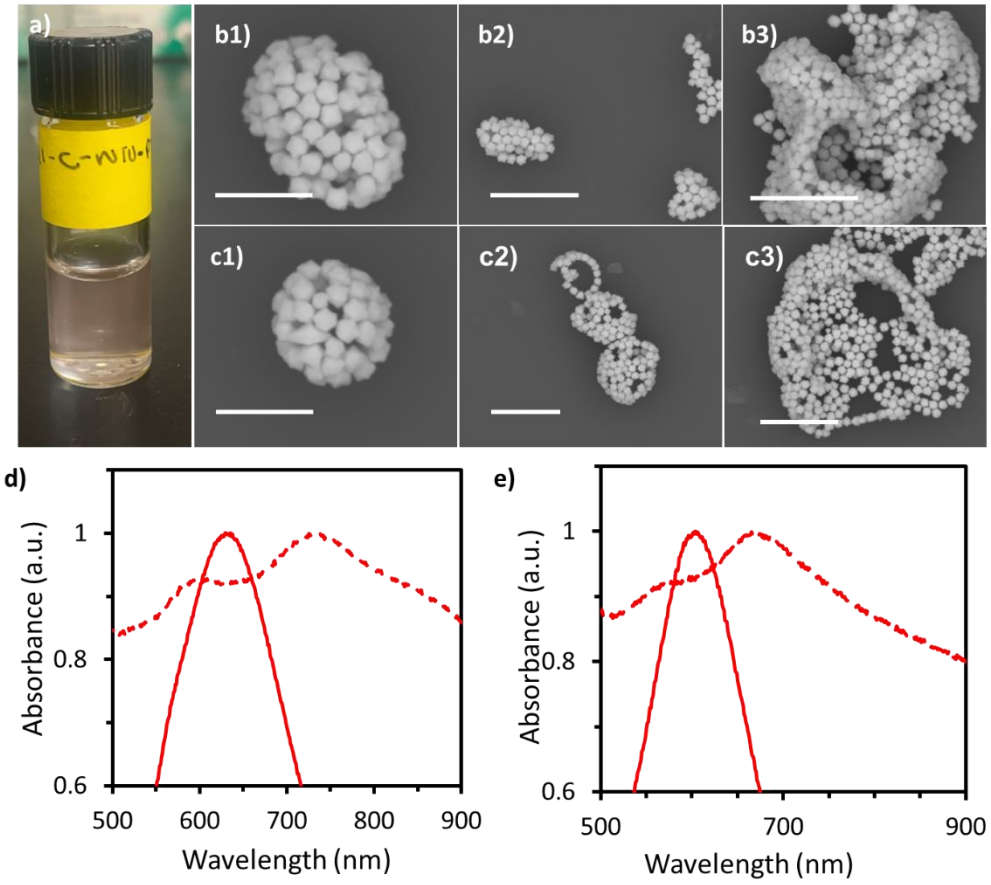

Figure 2.5 (a) Solution of relatively large Au NTOs after dialysis. (b-e) SEM images of network-like assemblies produced from ~100 nm Au NTOs: vesicles (Top) and aggregates (Bottom) grafted with PS_{341}-b-PEO_{45} (b1-b3) and PS_{652}-b-PEO_{82} (c1-c3). Scale bars: 500 nm (b1, c1), 1 μm (b2, b3, c2), 3 μm (c3). Corresponding UV-Vis spectra of plasmonic shifts before and after dialysis for large Au NC modified with PS_{341}-b-PEO_{45} (d) and PS_{652}-b-PEO_{82} (e).

The solution-based self-assembly of PGNPs is a promising approach for the organization of anisotropic Au NPs with different geometric shapes into vesicles. It is well known that the distinct surface characteristics of anisotropic nanoparticles (i.e., surface area, curvature, and exposed facets) endow NPs with unique properties. Therefore, the optical properties should be more enhanced for vesicles composed of anisotropic NPs compared to spherical NPs. To shed light on the practical implications of anisotropic vesicles, the UV-spectra of vesicles produced from

cubic (Figure 2.6a), trisoctahedron (Figure 2.6c), and transitional-shaped (Figure 2.6d) Au NPs (~ 60 nm) were compared to vesicle assemblies fabricated from spherical Au NPs of similar size at a constant M_w of BCP (Figure 2.6b). Analysis of SEM images in Figure 2.6a-d show that the self-assembly of different geometries prepared produced relatively small vesicles (~300 nm to 500 nm). The corresponding UV-Vis spectra of nanosphere and nanocubes both show splitting of the plasmon peaks. For instance, vesicles assembled from Au NS exhibited plasmonic peaks at 609 nm and 704 nm, while Au NC vesicle assemblies displayed significantly red-shifted peaks at 625 nm and 770 nm. The absorption bands of Au NTO and Au NTR have weak should peaks, but the resulting structures for both PGNPs exhibit distinct LSPR peaks around 630 nm. Hollow vesicles assembled from plasmonic nanoparticles are of great interest for biomedical applications, due to their excellent optical properties originating from LSPR peaks in the NIR region. The significant redshift in the LSPR peak and the broadening of SPR bands relative to the initial spectrum in conjunction with the difference in color changes before and after dialysis implies that the formation of assembly structures occurred in the solution. Additionally, the larger redshifts in LSPR peaks of anisotropic NP assemblies compared to spherical NP assemblies show the potential for improving plasmonic devices with enhanced LSPR sensing.

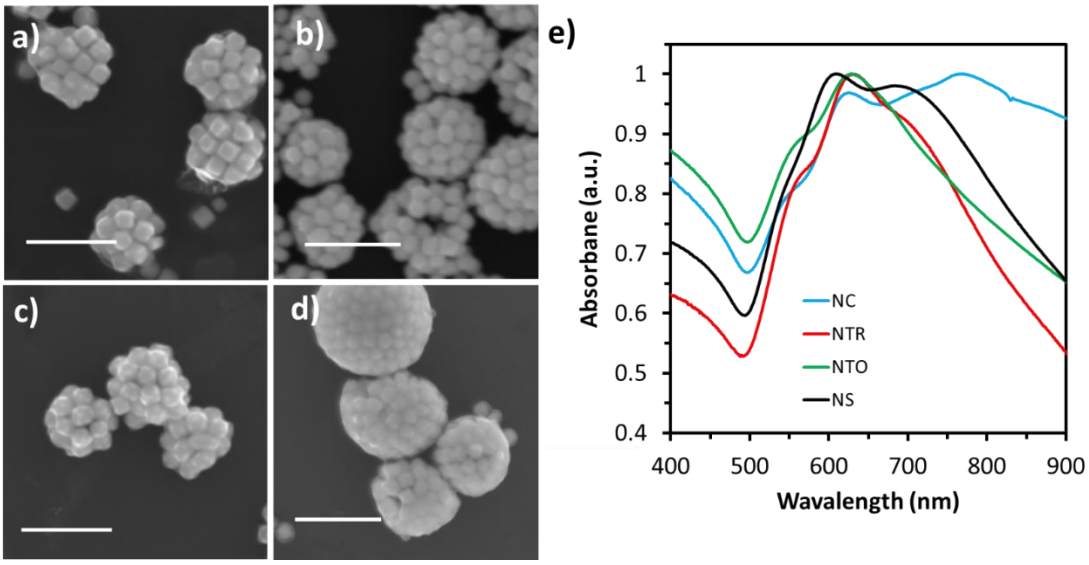

Figure 2.6 SEM images of vesicles produced from the self-assembly of different anisotropic Au NPs tethered with PS_{300}-b-PEO_{45} : (a) nanocubes (b) nanospheres (c) trisoctahedron nanoparticles and (d) transitional type nanoparticles. Scale bars: 300 nm (a, c) and 400 nm (b, d). (e) corresponding UV-Vis spectra of vesicles assembled from B-PGNPs with different geometric shapes.

The formation of vesicle structures suggests that the self-assembly processes for these anisotropic nanoparticles resemble the organization of PGNPs with spherical nanoparticles. In this case, self-assembly favoring geometrically frustrated architectures is also achieved by the delicate balance of enthalpic/entropic forces following the thermodynamic drive to reduce conformational entropy after the collapse of hydrophobic blocks onto NP surfaces. Therefore, the assembly behavior and final assembly of structures of B-PGNPs with anisotropic Au NPs should strongly correlate to changes in the hydrophilic/hydrophobic balance, which can be dictated by tuning the NP size and length of BCPs grafted to NP surfaces.[53] To explore this effect, we studied the self-assembly of Au NCs with varying dimensions and compared their final assembly morphologies.

2.3.3 Impact of NP size and BCP length on the formation of vesicles

We started by investigating the self-assembly of 60, 70, and 90 nm Au NCs functionalized at a constant M_w of BCP to understand the influence of Au NC size on the formation of assembled structures. Compared to vesicle structures assembled from 60 nm tethered Au NCs, 70 nm and 90 nm Au NCs modified with PEO_{45}-*b*-PS_{130}-SH copolymers produced drastically different assembly structures. SEM images in Figure 2.7 show that 70 nm Au NCs tethered with amphiphilic BCPs self-assembled into 3D sheet-like aggregates, while B-PGNPs consisting of 90 nm Au NCs self-assembled into large 2D aggregates. Since the self-assembly of larger Au NCs did not lead to the formation of vesicles, preliminary results would suggest that the vesicular morphology strongly depends on the NP dimensions. However, SEM images of 70 nm particles also reveal extremely broken vesicles, indicating the potential to organize relatively large Au NCs into high-curvature arrangements (Figure 2.7a). According to the equation $R_0 = bN^{1/2}$, the root mean square end-to-end distance of BCPs is estimated to be 7.79 nm for PS_{130}. As the dimensions of the Au NC core increase, enthalpic contribution of BCPs becomes less significant, which results in stronger Van der Waals forces between approaching Au NCs during assembly.[84] Thus, a morphological transition from vesicles to disordered aggregates with increasing dimensions of the Au NCs may also occur from the inability of the PEO_{45}-*b*-PS_{130}-SH copolymer brushes to efficiently stabilize larger NC cores after self-assembly.[54]

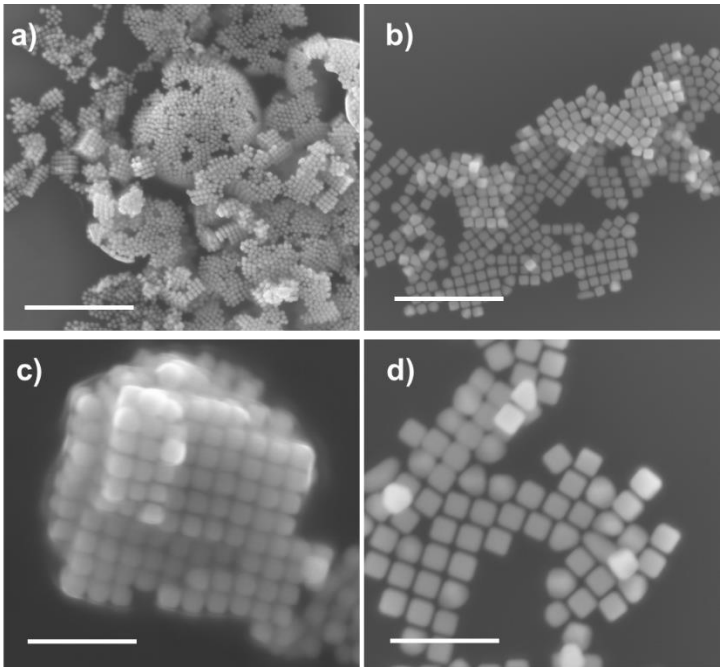

Figure 2.7 Large area and close-up SEM images of aggregate assemblies produced from relatively large Au NCs grafted with PS_{130}-b-PEO_{45} (a,c) 70 nm Au NCs and (b,d) 90 nm Au NCs. Scale bars: 1 μm (a,b), 400 nm (c,d).

90 nm Au NCs functionalized with PEO_{45}-*b*-PS_{341}-SH produced vesicles with closer-packing arrangements in the vesicular membrane compared to vesicles produced from Au NCs tethered with longest chain length (Figure 2.8a1 and a2). 90 nm Au NC tethered with even longer chain lengths, PEO_{82}-*b*-PS_{652}-SH, produced a mixture of "web-like" vesicles with Au NCs packed in network arrangements in the vesicular membrane (Figure 2.8b1). The SPR peak shifted from having one peak around 606 nm before assembly to having two plasmonic bands with peaks at 597 nm (shoulder peak) and 681 nm after assembly (Figure 2.8c). Although, significant attention is needed to improve the packing efficiency and monodispersity of vesicles. SEM images in Figure 2.8a3, b2, and b3 also show large chain-like aggregates assembled large anisotropic B-PGNPs,

which may have resulted from kinetic trapping due to the slower mobility of Au NPs with larger dimensions. Even so, the self-assembly of anisotropic NPs with sharp faces into high-curvature structures is uncommon, especially for NPs with relatively large dimensions (50 nm or more).[84]

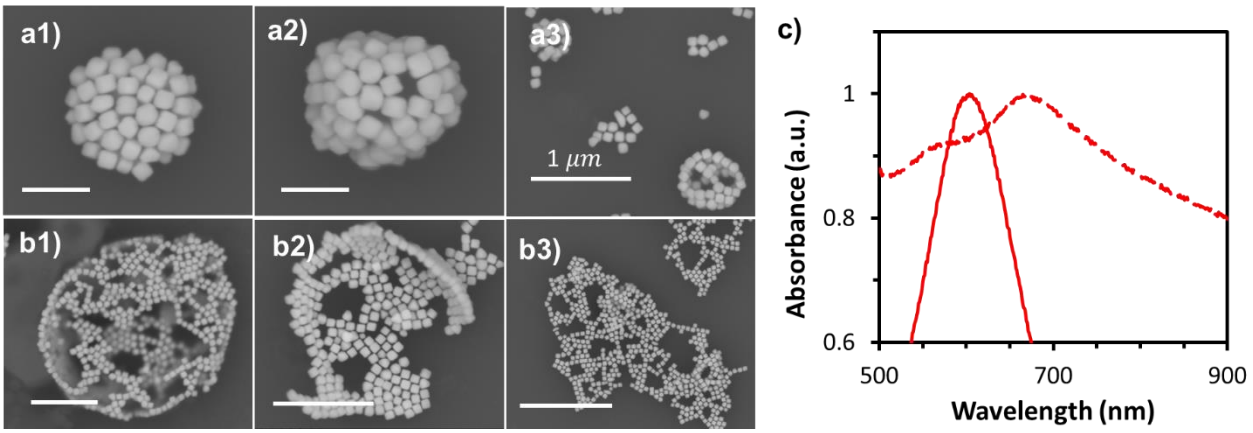

Figure 2.8 (a-d) SEM images of network-like assemblies produced from relatively large Au NCs (~90 nm): vesicles (Top) and aggregates (Bottom) grafted with PS_{341}-*b*-PEO_{45} (a1-a3) and PS_{652}-*b*-PEO_{82} (b1-b3). Scale bars: 300 nm (a1, a2), 1 μm (a3, b1, b2), 500 nm (b3). (c) Corresponding UV-Vis spectra of plasmonic shifts before and after dialysis for large Au NC modified with PS_{652}-*b*-PEO_{45}.

While the relationship between the hydrophilic/hydrophobic balance and vesicle formation remains relatively unexplored for cubic nanoparticles, our results show that the morphology of assembly structures and final packing arrangements of NCs within vesicular membranes is influenced by the length of PEO-*b*-PS copolymers. The enhanced ordering of 90 nm Au NC from 2D aggregates to vesicle structures with increasing BCP chain lengths further emphasize that BCPs grafted to inorganic NPs not only manipulate the interparticle interactions but also play a key role in stabilizing NPs during the self-assembly process.

Previous studies of polymer-grafted nanocubes have shown that the packing arrangements and orientations within 2D structures depend on the polymer chain length, rigidity, or grafting

density.[21,24,85,86] To further elucidate the role of BCPs, we systematically investigated the effect of BCP length on the self-assembly of 60 nm Au NCs grafted with 4 different copolymers: PEO_{45}-*b*-PS_{97}-SH (10.8 K) , PEO_{45}-*b*-PS_{130}-SH (13.5 K), PEO_{45}-*b*-PS_{300}-SH (31.2 K) and PEO_{45}-b-PS_{652}-SH (71.5 K). SEM images in Figure 2.9 show a morphological transition of assembly structures from clusters to vesicles for increasing BCP lengths. In comparison to the NCs modified with PEO_{45}-*b*-PS_{130}-SH (Figure 2.9b and f),the self-assembly of B-PGNPs grafted with a relatively shorter BCP, PEO_{45}-b-PS_{97}-SH (Figure 2.9a and e) generated 2D clusters and aggregates. It is visibly clear from SEM images that Au NCs tethered with relatively longer BCPs, PEO_{45}-b-PS_{300}-SH (Figure 2.9c and g) and PEO_{45}-b-PS_{652}-SH (Figure 2.9d and h),are more loosely packed inside the vesicular membrane. An increase in interparticle spacing is no surprise due to the increased volume of hydrophobic blocks concentrated between neighboring NPs.[53,84] As BCP length increases, polymer brushes generally extend away from the NP surfaces much farther than their natural dimensions to avoid steric overcrowding. Moreover, the formation of vesicles with frequent gaps and random packing arrangements arise as a consequence to alleviate the competition between the surface tension of the spherical structures and the increased bending rigidity of tethered polymer brushes.[87]

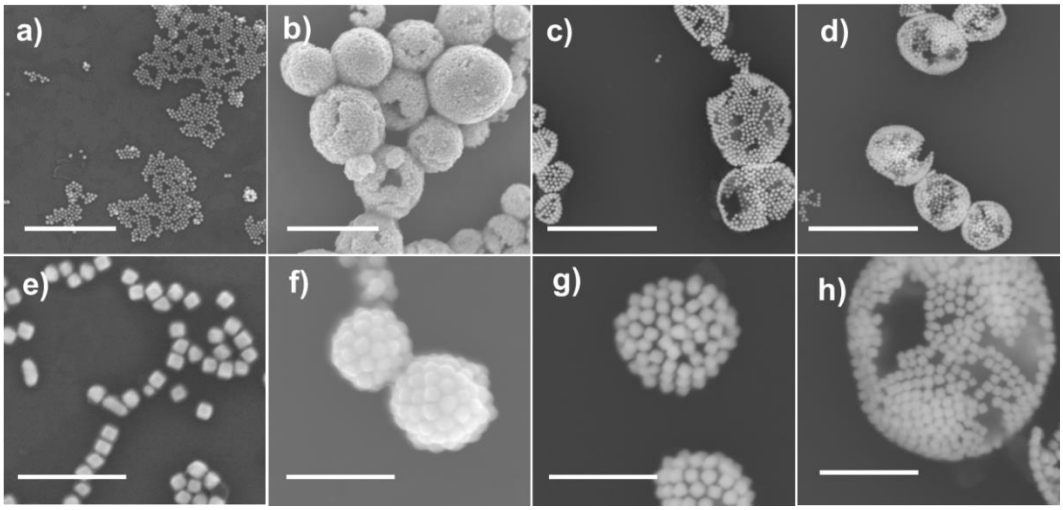

Figure 2.9 Large area and close-up SEM images of assemblies produced from 60 nm Au NCs tethered with different BCP lengths: (a,e) PS_{97}-b-PEO_{45} and (b,f) PS_{130}-b-PEO_{45} (c,g) PS_{300}-b-PEO_{45} and (d,h) PS_{652}-b-PEO_{82} Scale bars: Scale bars: 2 μm (a-d), 500 nm (e-g) 600 nm (h).

2.3.4 Geometric Considerations on Self-Assembly Behavior

To explore the effect of graft density on the self-assembly behavior of anisotropic NPs, we varied the adsorption of amphiphilic copolymer brushes to Au NC surfaces by changing the initial concentration of BCPs, C_{BCP}, in the ligand exchange procedure. Self-assembly experiments were conducted for 60 nm Au NCs prepared with the following BCP concentrations in THF, C_{BCP} = 0.01, 0.02, 0.06, and 0.25 mg/mL. For example, SEM images in Figure 2.10a present ~60 nm Au NC functionalized with PEO_{45}-*b*-PS_{300}-SH before assembly. Close examination of Au NCs prepared with different BCP concentrations revealed that the coatings of polymer layers have different types of corona shapes. At the lowest concentration, C_{BCP} = 0.01 mg/mL, the polymer shell is conformed to a cubic shape around the NP surface. As the concentration increases, there is a visible increase in the convexity of the shell on the flat surfaces, which results in a spherical corona at the highest concentration, C_{BCP} = 0.25 mg/mL. The increase in shell convexity was also

reflected by an increase in the shell thickness (Figure 2.10b). This can be explained by an increase in steric hinderance of polymer brushes due to the self-limiting nature of the ligand-exchange process. Assuming that BCPs preferential avoid attaching to areas with high curvature (i.e. corners & edges), the local environment for each polymer brush becomes more crowded and subsequently stretched at the center regions with increasing graft density on flat Au NC surfaces. As the polymer adsorption increases, the already attached polymer chains impose a steric barrier for the incoming polymer chains, which causes a thicker polymer shell at the flat regions compared to the corners and edges.

Depending on the initial concentration of copolymers, 60 nm tethered Au NCs self-assembled into structures with distinct packing arrangements. For instance, 60 nm Au NCs tethered with PEO_{45}-*b*-PS_{130}-SH transition from sheet-like aggregates to vesicles structures with distinct configurations (Figure 2.10c-h). SEM images in Figure 2.10c and 2.10f show that Au NCs align face-to-face in stacked arrangements at relatively low C_{BCP} of 0.01 and 0.02 mg/mL, respectively. In comparison, Au NCs are geometrically frustrated in curved structures at higher C_{BCP} of 0.06 mg/mL (Figure 2.10d and g) and 0.25 mg/mL (Figure 2.10e and h). Even though the vesicular morphology is consistent, the dimensions and surface topologies of vesicles are quite different. The average size of vesicles for C_{BCP} of 0.06 mg/mL is ~800 nm with lengths up to several micrometers, while the average size of vesicles for C_{BCP} of 0.25 mg/mL is ~300 nm. Larger vesicles have significantly more face-to-face arrangements with low geometric frustration. Thus, a smoother topology of Au NC faces is present in the membrane. In contrast, face-to-face packing is drastically reduced and the topology is more defined with corners and edges due to the significant degree of geometric frustration in smaller vesicles. Similar trends are observed for 60 nm Au NC tethered with PEO_{45}-*b*-PS_{300}-SH and PEO_{82}-*b*-PS_{652}-SH. A recent experimental study

revealed that the self-assembly and packing arrangements of cubic NPs depended on the shell shape around the cubic surfaces (i.e. corona morphology).[86] Therefore, we suspect that the observed morphological transitions could be dictated by the corona morphology of PGNPs.

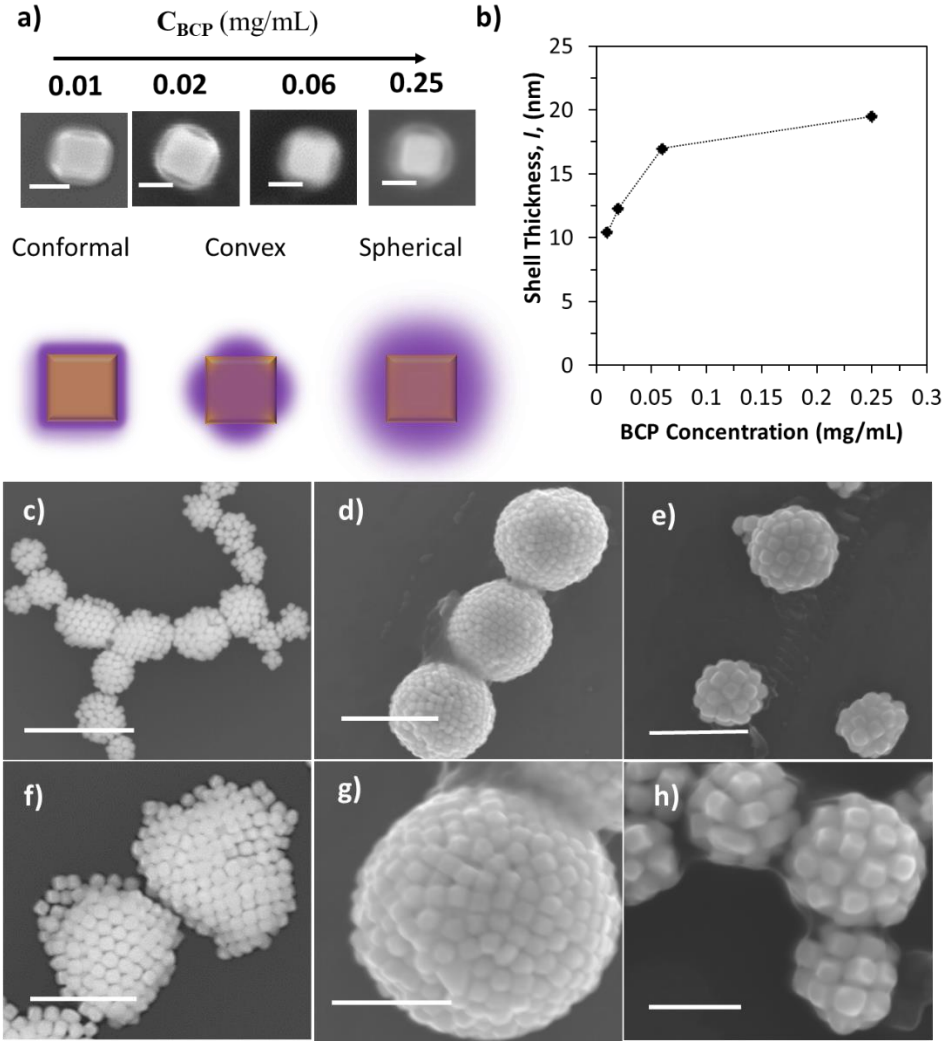

Figure 2.10 (a) Schematic illustration of corona morphology dependence on BCP concentration and representative SEM images of B-PGNPs of Au NCs prepared with different concentrations of thiol-terminated polystyrene-*b*-polyethylene oxide: 0.01, 0.02, 0.06, 0.25 mg/mL (left to right). All scale bars: 50 nm. (b) Ligand shell thickness, *l*, measured from SEM images as a function of BCP concentration for 60 nm Au NCs in the dried state. Representative SEM images of (c,f) sheet-like aggregates, relatively (d,g) large and (e,h) small vesicles assembled from 60 nm Au NCs modified with PS_{130}-b-PEO_{45} copolymers. Scale bars: 1 μm (c,d) 400 nm (e,g), 500 nm (f), and 200 nm (h).

2.3.5 Stability of Vesicles with cubic PGNPs

Hybrid vesicles assembled at room temperature were subject to defects after dialysis. For instance, an inspection of SEM images in Figure 2.11(a-c) shows the degradation of membranes in some of the vesicle structures after dialysis. This suggests that the attractive hydrophobic interactions are insufficient to overcome the steric hindrance between Au NCs.[60] To investigate the stability of vesicles, solutions of vesicle assemblies were incubated at 50 ℃. SEM, UV-Vis, and statistical analysis of different vesicle assemblies (I, II, and III) produced from 60 nm Au NC functionalized with PEO_{45}-b-PS_{130} were taken after dialysis at room temperature (25 ℃′), immediately after thermal treatment (50 ℃), and after samples completely cooled back down to room temperature (25 ℃′′). To confirm the behavioral changes, SEM observations were compared with statistical analysis of the hybrid vesicle dimensions and the plasmonic peaks at each stage. Examination of SEM images prior to heat show that roughly 50% or more of vesicles were defective after sample were left undisturbed at room temperature. However, SEM of samples that were incubated at 50 ℃ and left to cool at room temperature display a clear improvement in the quality of vesicles and roughly 30% or less of the vesicles were defected (Figure 2.11d-f). The noticeable transition was also reflected by changes in the absorption spectra. For instance, Figure 2.11h shows broad absorption bands at 25 ℃’ with a single SPR peak at 662, 673, and 686 nm for the different vesicle assembly solutions I, II, and III, respectively. In contrast, all the solutions display two well-defined (or one peak and shoulder) plasmonic peaks at 25 ℃’’ Figure 2.11i. A comparison of the average vesicle diameters at each stage for samples I, II, and III revealed that the vesicle dimensions were not significantly affected, but a slight decrease in the average sizes was observed after exposure to 50 ℃ heat (Figure 2.11g). However, transformations in the UV-

Vis spectra strongly suggest that the structural changes occurred in the solution and that the vesicle morphology is a metastable structure for cubic B-PGNPs.

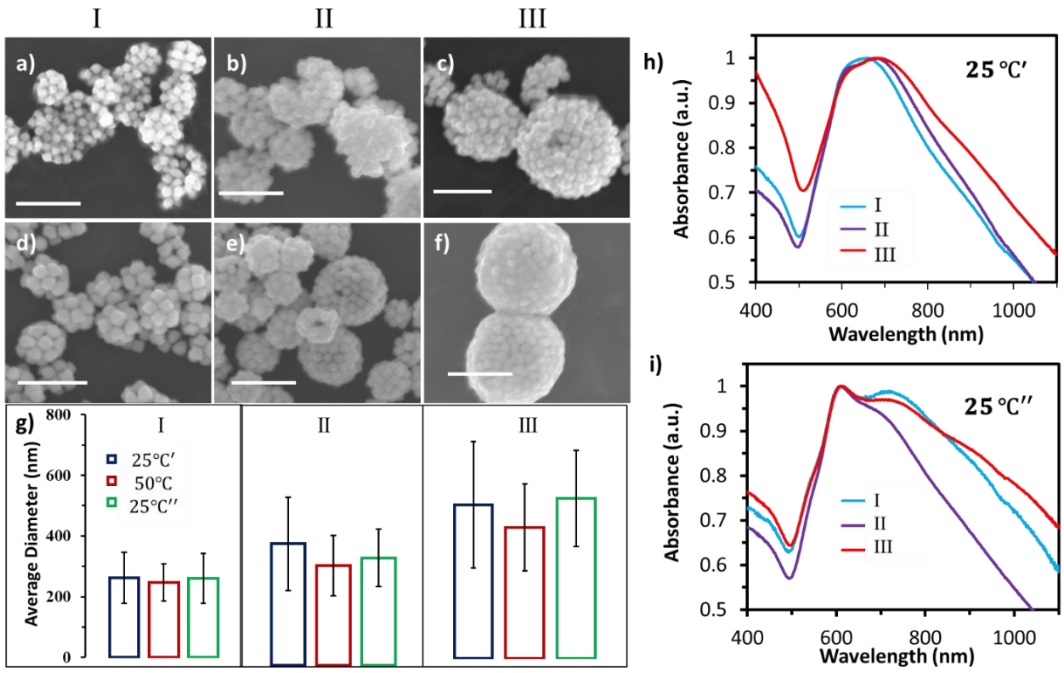

Figure 2.11 Representative SEM images of (a-c) defected vesicles before thermal treatment and (d-f) vesicle structures after thermal treatment in 3 different samples. All scale bars: 500 nm. (g) statistical analysis of vesicle dimensions in different samples. Corresponding UV-Vis spectra of vesicle assemblies taken (h) after dialysis at room temperature 25 ℃' and (i) after cooling down to room temperature after thermal treatment 25 ℃''.

These structural changes were confirmed by SEM images of assemblies immediately after heating. SEM images in Figure 2.12a-f, not only show intermediate states of vesicle assemblies with disrupted membranes for samples I, II, and III, but also show a larger presence of aggregates and spherical clusters. It is clear from the increased presence of aggregated clusters that vesicles were unstable and disassembled into smaller structures. This is also supported by the fact that a blue-shift in the LSPR peaks around 610 nm occurred for all samples. Interestingly, the SPR peaks of the UV-Vis spectra in Figure 2.12g obtained immediately after heating also show that a distinct peak emerged around 960 nm. We suspect that the rise in temperature increased the number of

optically excited energetic electrons in Au NCs which generated higher-multipolar order plasmon modes from the junctions of highly localized hot spots between nanoparticles.[88] At the end of the cooling cycle, the LSPR peaks at ~610 nm was maintained, and a weaker secondary peak emerged at ~715 nm for each of the samples, which suggests that a portion of Au NCs re-configured into vesicles upon cooling. SEM images show that ~70% or more of samples I, II, and III contained high-quality vesicles with intact vesicular membranes.

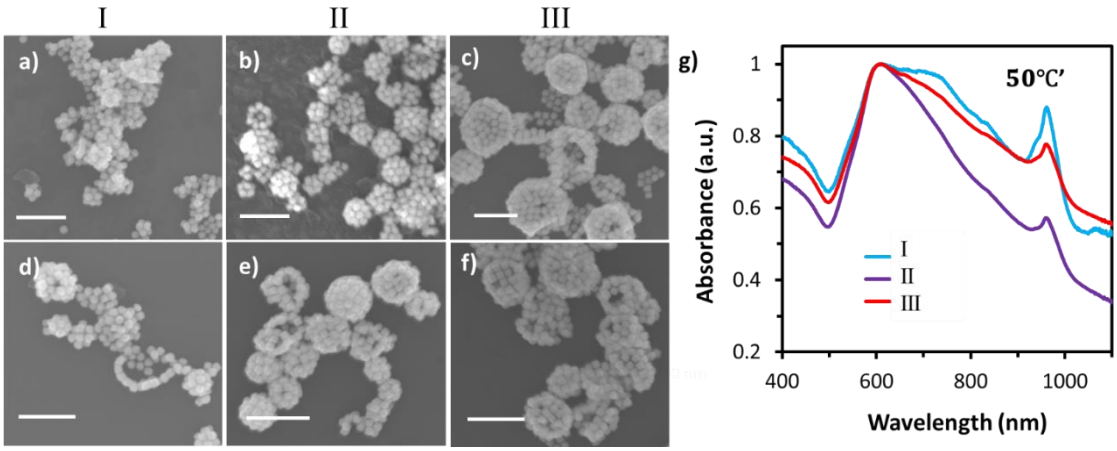

Figure 2.12 (a-f) Representative SEM images of morphological transitions induced by thermal treatment at 50 ℃ in 3 different samples of vesicular assemblies. All scale bars: 500 nm. (g) Corresponding UV-Vis spectra of different samples taken immediately after thermal treatment.

2.4 Conclusion

The solution-based self-assembly anisotropic Au NPs tethered with amphiphilic BCPs is a versatile strategy for guiding the organization of NPs with different geometric shapes into well-defined structures, such as vesicles. Exploratory investigations indicate that the formation of vesicles strongly correlates to the shape and characteristics of the grafted polymer shell around nanocubes. The stability and structure of hybrid vesicles and the resulting optical properties were influenced by the BCP length and heat stimuli. Preliminary findings highlight the optical benefits

of designing and tailoring nanostructures with anisotropic shapes. However, a more in-depth understanding of the factors that dictate vesicle formation is crucial for advancing the rationale design of nanostructures with tailored functionalities. Thus, continued exploration in this area is needed to fully realize their potential before advancements in the field of self-assembled nanomaterials are possible.

Chapter 3: BCP Length Effect on Co-assembled Vesicles

Overview. The fabrication of complex nanostructures integrated with different physical and chemical properties from multiple building blocks has gained significant attention from researchers in recent years. To date, the concurrent self-assembly of multiple molecular amphiphiles (i.e. lipids, surfactants, and or polymers) or a combination of amphiphilic polymers and inorganic nanoparticle amphiphiles have mainly been used as building blocks for the production of highly complex, multifunctional nanostructures. In this chapter, we report the design of hybrid vesicles from the co-assembly of binary B-PGNPs with amphiphilic copolymers in solution. Several combinations of binary hybrid building blocks containing a mismatch of NP sizes and/or a mix of Au NP shapes were studied for co-assembly the effect of NP size and BCP length was explored in each system. Hybrid vesicles with phase-separated domains were observed, which likely occurred from attractive depletion forces and the conformational entropy gain of tethered BCP chains. These distinct vesicular morphologies include patchy vesicles (PVs) with distinct domains of small and large B-PGNPs, yolk/shell vesicles (YVs) with large B-PGNPs randomly distributed or located in the center of the vesicular membrane of small B-PGNPs.

3.1 Introduction

The concurrent self-assembly of multiple molecular and/or colloidal amphiphiles (i.e. lipids, surfactants, BCPs, inorganic nanoparticles) has attracted intense research interest in constructing novel nanomaterials and devices with desired architectures and properties.[75] This strategy enables the design of increasingly complex multicomponent nanostructures that are otherwise not easy to achieve by the self-assembly of individual entities. Highly-complex multicomponent nanostructures have been fabricated from two or more molecular amphiphiles

(i.e. lipids, surfactants, and or polymers) or a combination of amphiphilic polymers and inorganic nanoparticle amphiphiles. In fundamental and clinical biomedical research, nanostructures endowed with plasmonic and magnetic nanoparticle amphiphiles can be used for more robust therapy treatments on cancerous tumors through the combination of accurate imaging, controlled drug release, and precise treatment of tumor sites.[64-77] Currently, the structure and compositional diversity of multicomponent plasmonic nanostructures are limited due to the field being in the early stages of development. Thus, it is vital to expand the library of assembled nanostructures to meet the rising demand for novel functional materials that can enhance current applications or develop new avenues. However, the self-assembly of multiple B-PGNPs with different sizes or shapes and their resulting nanostructures have rarely been investigated. Therefore, we explored the self-assembly of spherical and non-spherical NPs to extend the library of available building blocks and hybrid assemblies with desired architectures and properties.

Using the solution-based self-assembly strategy, we explored the preparation of hybrid vesicles with well-defined morphologies from the co-assembly of PGNPs tethered with amphiphilic BCPs in solution. As shown in Figure 3.1, an experimental study was conducted on the self-assembly behavior in two binary systems: (A) spherical B-PGNPs with different-sized Au NPs and (B) mixed-shaped B-PGNPs. Hybrid building blocks were modified with the same BCP to ensure that entropy was a dominant factor in addition to the hydrophobic interactions induced by a change in solvent quality. To generate organized hybrid nanostructures, several combinations of binary hybrid building blocks containing a mismatch of NP sizes and/or a mix of Au NP shapes were studied for co-assembly at varying volume fractions of B-PGNP dispersions. Specifically, the size ratio of Au NPs and the volume ratio of building blocks were tuned for binary components modified with identical BCP lengths. B-PGNP mixtures in Binary systems A and B were also

modified with mismatch lengths of grafted BCPs to study the effect of hydrophobic and hydrophilic brushes on the morphology of assemblies and determine the optimal assembly conditions for the generation of discrete multi-component structures. Preliminary investigations revealed that patchy or yolk/shell vesicle structures with distinct regions of relatively large spherical Au NPs (>60 nm) were observed when co-assembled with small Au NPs (~10 nm), depending on the length of BCPs, size ratio of Au NPs, and volume ratio of B-PGNPs in solution. Inspired by these results, BCP tethered Au nanospheres (~10 nm) were systematically utilized as depletants to control the NP location of larger B-PGNPs with different anisotropic shapes. We varied the concentration of small B-PGNPs to understand the effect on the phase separation within vesicle structures. Additionally, a kinetic study was also conducted using binary mixtures in Binary System A to further elucidate the controlled assembly of phase-separated vesicles and understand the assembly mechanism. A detailed discussion of the systematic study conducted in Binary System A will be provided in the next chapter. The purpose of this chapter is to provide insights into the effect tunable of parameters on the co-assembly B-PGNPs with distinct NP sizes and shapes. This work provides a facile route to readily access multicomponent hybrid assemblies from multiple B-PGNPs that have drastically different dimensions and/or geometries, which is promising for the design of exceedingly complex nanodevices with increased functionalities and advanced properties.

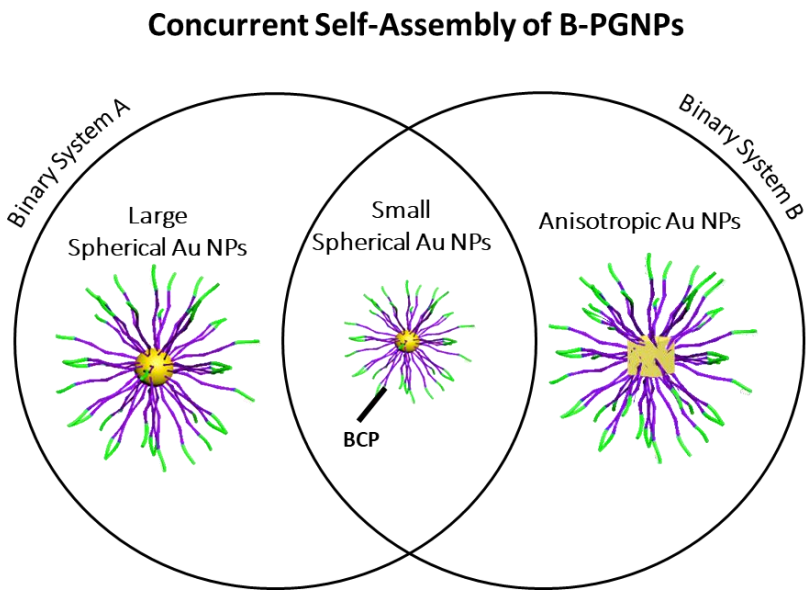

Figure 3.1 Schematic Illustration of building blocks in different binary mixtures used for the concurrent self-assembly of B-PGNPs.

3.2 Experiments

3.2.1 Materials

Styrene, azobis(isobutyronitrile) (AIBN), 4-cyano-4-(phenylcarbonothioylthio) pentanoic acid (CPPA), tetrahydrofuran (THF), dimethylformamide (DMF), Gold(III) chloride trihydrate (HAuCl4.3H2O, ≥99.9%), ascorbic acid (AA, ≥99.0%), sodium borohydride (NaBH4, 98%), sodium bromide (NaBr, ≥ 99.0%), cetyltri-methylammonium bromide (CTAB, ≥99%), and cetyltrimethyl-ammonium chloride (CTAC, 25 wt% in water) were all obtained from Sigma-Aldrich and used as received. Polystyrene-b-poly (ethylene oxide) (PS-b-PEO) without functional groups was purchased from Polymer Source, Inc. Styrene was distilled under vacuum prior to use and stored in a freezer at −20 °C. AIBN was recrystallized from ethanol. Hydrochloric acid (36.5-38.0%), sodium chloride were purchased from Sigma Aldrich and used as received unless otherwise noted. Deionized water (HPLC grade) from Fisher Scientific was used in all gold

nanoparticle synthetic and modification procedures and assembly experiments. Deionized water (Millipore Milli-Q grade) with resistivity of 18.0 MΩ was used in all the polymer synthesis experiments.

3.2.2 *Synthesis of Gold Nanoparticles*

Non-Spherical Au NPs. CTAC-stabilized, anisotropic gold nanoparticles were synthesized by the same seed-mediated approach described in Chapter 2 (see section 2.2.3). A summary of the experimental conditions for various sizes of anisotropic Au NPs that were synthesized, including the type of seed and the corresponding volume, can be found in Table 3.1. Additionally, the characterization details for non-spherical Au NPs that were used for self-assembly can be found in Chapter 2 (see Figure 2.2 in section 2.3.1).

Table 3.1. The type of seeds and volume of seed solution used in the synthesis of various anisotropic AuNPs with targeted diameters.

Au NP Shape	Size (nm)	Volume Water (µL)	Volume AA (µL)	Volume Seed (µL)	Centrifugation Speed (rpm)	Centrifugation Time (min)
Cube	60	9625	85	100	6,500	10
Transitional Product	60	9625	90	120	6,500	10
Trisoctahedron	60	9625	90	110	6,500	10

Spherical Au NPs. CTAC-stabilized nanospheres were synthesized using a successive, seed-mediated growth of single-crystal nanospheres with minor modifications.[83]

Preparation of the Initial, CTAB-Capped Au cluster.

A fresh aqueous NaBH4 solution (10×10^{-3} M, 0.6 mL) was rapidly added into a thoroughly mixed 10-mL aqueous solution containing $HAuCl^4$ (0.25×10^{-3} M) and CTAB (100×10^{-3} M) using

a pipette. A brown solution immediately formed upon the introduction of NaBH4 while stirring at a speed of 300 rpm for 2 min. Finally, the solution was kept undisturbed at room temperature for three hours to ensure complete decomposition of $NaBH_4$ remaining in the reaction mixture.

Preparation of 10 and 15 nm Au Nanospheres.

A solution of CTAC (0.1 M, 47.5 mL), AA (100×10−3 M, 7.5 mL), and the initial, CTAB-capped Au clusters were mixed in a 20-mL glass vial, followed by one-shot injection of an aqueous HAuCl4 solution (10×10^{-3} M, 1.25 mL). Refer to Table 3.2 for more detailed information about the volume of seed solution and the corresponding diameter of final nanospheres. The reaction was allowed to continue at 27 ○C for 15 min. The product was collected by centrifugation at 14,500 rpm for 30 min, and then washed with water once for further use and characterization. The 15-nm Au nanospheres were dispersed in 5 mL of aqueous CTAC solution (0.02 M) after washing, which was used as seeds in the second round of growth.

Preparation of 30 - 100 nm Au Nanospheres

A solution of CTAC (0.1 M, 25 mL), 23 mL of Millipore water, AA (10×10−3 M, 130 μL), and the 15-nm seeds were mixed in a 20-mL glass vial, followed by dropwise addition of aqueous HAuCl4 solution (6.25×10−3 M, 2 mL) using a syringe pump at an injection rate of 2 mL/h. Please see Table 3.2 for more detailed information about the volume of seed solution and the corresponding diameter of final nanospheres. The reaction was allowed to proceed at 27 ○C for 10 min after the injection had been finished. The final product was collected by centrifugation at 12,00 rpm for 15 minutes and washed with water once for characterization.

Table 3.2 The type of seeds and volume of seed solution used in the synthesis of spherical AuNPs with targeted diameters.

Diameter of Nanosphere (nm)	Type of Seed	Volume (μL)
10	Cluster	800
20	Cluster	250
30	15-nm sphere	90
60	15-nm sphere	75
75	15-nm sphere	40

3.2.3 Preparation of B-PGNPS for Co-Assembly

Au NPs were modified with a series of thiol-terminated PEO-*b*-PS BCPs with different molecular weights. The synthetic procedure for thiol-terminated BCPs were obtained from a previously reported reversible addition-fragmentation chain transfer (RAFT) polymerization procedure.[53] (see Section 2.2.2) The characterization details can be found below in Table 3.3. Different concentrations of BCPs (C_{BCP}) were dissolved in 10 mL of dimethylformamide (DMF) and added slowly to 100 uL aqueous solution of AuNPs that was concentrated from 10 mL via centrifugation. Co-assembly experimental studies were conducted for mixtures of spherical gold nanoparticles (C_{BCP} = 0.2 mg/mL) and non-spherical nanoparticles (C_{BCP} = 0.6 mg/mL) modified with PEO-*b*-PS-SH. The characterization of spherical B-PGNPs details can be found below in Table 3.4. Subsequently, the mixture was sonicated for 1 h to avoid any aggregation and then kept undisturbed for 24 h to complete the ligand exchange. The procedure was repeated for non-spherical nanoparticles, except the time to complete ligand exchange was shortened to 1 hr to prevent the etching of edges and corners by copolymers. Dispersions of B-PGNPs in DMF were

washed for several centrifugation cycles and redispersed in 1.5 mL tetrahydrofuran (THF) for nanospheres or 0.75 mL for anisotropic nanoparticles. After excess free BCP was removed, B-PGNPs demonstrated good colloidal stability in THF, a good solvent for the ligands.

Table 3.3 Characterization of thiol-terminated PS-*b*-PEO copolymers.

PEO_x-*b*-PS_y-SH	x	y	M_n [a] (kg/mol)^{GPC}	M_n [b] (kg/mol)^{NMR}	PDI	R_0 [c]
P1	45	99	-	10.3	-	6.8
P2	45	130	9.7	13.5	1.11	7.8
P3	45	211	16.0	23.9	1.15	9.7
P4	45	300	24.0	31.2	1.12	11.8
P5	45	421	68.7	45.8	1.08	14.4
P6	82	652	67.9	71.5	1.07	17.9

*[a]Number-average molecular weight (M_n, GPC) determined by GPC using polystyrene standards for calibration. [b]Number-average molecular weight calculated from NMR measurements. [c]Root mean square end-to-end distance of PS blocks, calculated from $R_0 = bN^{0.5}$, where b is the Kuhn length (b = 0.18 mm for PS) and N is the number of Kuhn segments.

Table 3.4 Characterization of Au NS modified with thiol-terminated PS_{130}-*b*-PEO_{45} and PS_{421}-*b*-PEO_{45} copolymers.

Au NS Diameter (nm)	M_n [b] (kg/mol)^{NMR}	Graft Density	l	R_0/l
10	13.5	0.48	1.4	5.4
10	45.8	0.13	2.8	5.2
60	13.5	0.56	1.3	5.8
60	45.8	0.18	2.4	6.1

3.2.4 Characterizations

^{1}H NMR. ^{1}H NMR spectra were recorded with a Bruker AV-400 Mhz high resolution NMR spectrometer in $CDCl_3$.

Gel permeation chromatography (GPC). GPC measurements were performed using a Viscotek system equipped with a refractive index detector (RI 410) and four columns at 45 ^{o}C. THF was used as the eluent at an elution rate of 1 mL min^{-1}, and polystyrene standards were used for calibration.

Thermogravimetric Analysis (TGA). TGA was used to characterize the grafting density of BCPs on the surface of the NPs. A10.0 mL stock solution of building blocks was centrifuged for 6-8 cycles in THF to remove excess BCPs. After removal of the supernatant, samples were left to dry for 1 hr to evaporate the remaining solvent. The experiments were carried out in an Argon atmosphere with the following temperature program: heat from 100 ^{o}C to 700 ^{o}C at a scan rate of 10 ^{o}C / minute with a purge rate of 20 mL/minute. During the scan process, the temperature was maintained at 150 ^{o}C for 30 minutes to further remove moisture.

UV-Vis Spectroscopy. The extinction spectra of AuNPs, modified particles, and assembly structures were taken on a PERKIN LAMBDA 35 UV/Vis System.

DLS Measurements. The hydrodynamic diameters of AuNPs, modified particles, and assembly structures were conducted on Zetasizer Nano-ZS system (Malvern), equipped with a He-Ne 633 nm laser as the light source.

SEM and TEM imaging. The assembly structures were imaged using a Hitachi SU-70 Schottky field emission gun Scanning Electron Microscope (FEG-SEM) and a JEOL FEG Transmission Electron Microscope (FEG-TEM). Samples for SEM and TEM were prepared by drying ~3-4 μL of aqueous solution of assembly structures on silicon wafers and copper grids at room temperature, respectively.

Image J measurements. The data collected from SEM images was further analyzed using ImageJ software to further confirm the dimensions and size distribution of diameters in samples of individual Au NPs. Statistical analysis on SEM images of hybrid vesicle structures with yolk/shell morphology was also performed to determine the diameter size distribution and morphological properties of assembled structures.

3.3 Results and Discussion

3.3.1 Characterization of B-PGNPs for Co-assembly

Co-assembly experiments were conducted for binary combinations of B-PGNPs with various sizes and shapes of gold nanoparticles (Au NPs). Figure 3.1 illustrates the type of co-assembly systems used in this study, which are distinguished by the variation in the larger building blocks. The different systems are referred to as Binary System A and Binary System B throughout this work, where Binary System A consists of spherical Au NPs with different sizes and Binary System B consists of Au NPs with different shapes including nanocubes (NC), trioctahedral nanoparticles (NTO), and transitional type nanoparticles (NTR). Au NPs were synthesized by previously reported literature procedures and grafted with various lengths of amphiphilic BCPs. We synthesized monodisperse CTAC-capped Au nanospheres with different diameters using a seed-mediated growth method with modifications to the seed volume. Figure 3.2 shows representative SEM images of Au nanospheres (NS) with different dimensions (10-100 nm) prepared for self-assembly and the corresponding UV-Vis spectra. SEM and UV-Vis characterizations of the anisotropic Au NPs are found in Chapter 2 (see section 2.3.1, Figure 2.2).

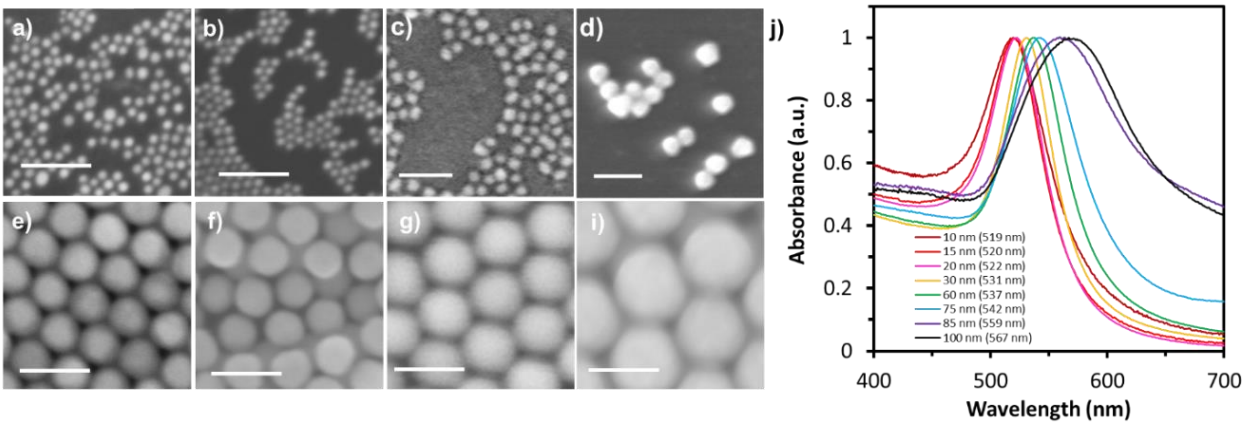

Figure 3.2 SEM images of AuNSs with different sizes: (a) 10 nm, (b) 15 nm, (c) 20 nm, (d) 30 nm, (e) 60 nm, (e) 75 nm, (g) 85 nm and (h) 100 nm and the corresponding All scale bars: 100 nm. (j) UV-Vis absorption spectrum of Au nanospheres with different dimensions.

Using a ligand exchange approach, B-PGNPs were prepared by grafting PS-*b*-PEO to the surfaces of CTAC-stabilized to ensure assembly occurs in solution.[89] In the solution exchange approach, amphiphilic BCPs are covalently grafted to the surfaces of Au NPs via Au-S bonds. The characterization details of the various BCPs used in this study are summarized in Table 3.1. Co-assembly experiments were primarily conducted for Binary System A, but the versatility of the approach was explored for Binary System B. Each dispersion of B-PGNPs in THF was combined in small vials with different volume ratios and thoroughly mixed under sonication prior to dialysis. Using B-PGNPs in Binary System A with 10 nm and 60 nm Au NS as an example, the grafting densities (σ) of relatively short (M_n = 13.5 K) and long (M_n = 45.8 K) copolymer ligands were derived from thermal gravimetric analysis (TGA) for different sized Au NPs (Figure 3.3). The B-PGNP building blocks are donated as NS_D-PS_x-*b*-PEO_y, where D indicates the diameter, and x and y are the corresponding repeating units of individual blocks of tethered BCPs.

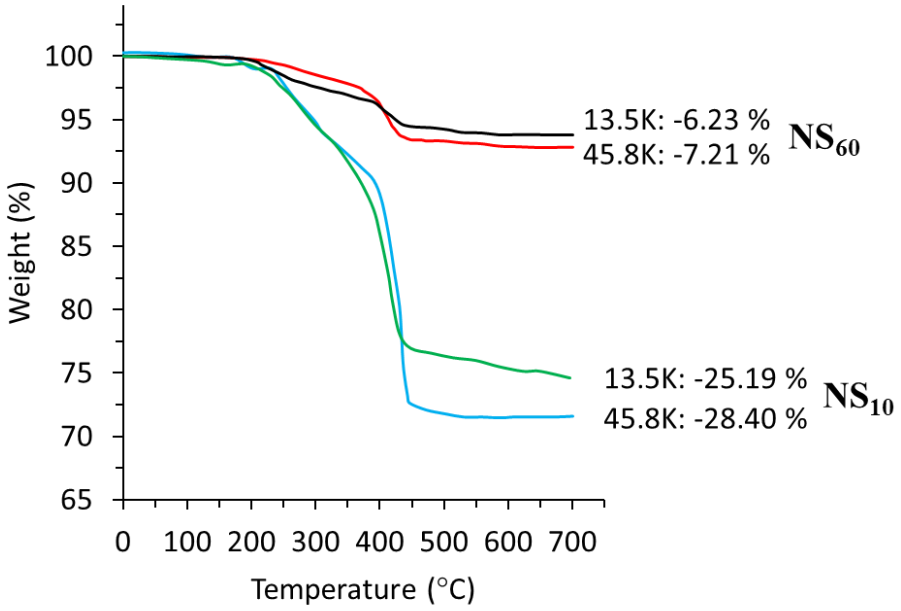

Figure 3.3 TGA of copolymer ligand weights for different hybrid building blocks.

The σ can be calculated using Equation 1 based on the weight loss of BCPs at elevated temperatures above 200 ºC ($wt\ \%_{BCP}$) and the residual mass of Au NPs above 450 ºC ($wt\ \%_{Au\ NP}$).

$$\sigma = \frac{wt\ \%_{BCP} \times N_A \times \rho \times V}{wt\ \%_{Au\ NP} \times M_n \times A} \qquad \text{Equation 1}$$

Where N_A is the Avogadro's number, ρ is the bulk density of gold, V is the volume of a single Au NP, M_n is the number-average molecular weight of BCPs determined by NMR. From TGA measurements in Figure 3.3, 10 nm Au NS tethered with the short and long BCPs showed a weight loss of 25.19% and 28.40%, respectively Moreover, 60 nm Au NS tethered with M_n 13.5 K and 45.8 K copolymers showed a weight loss of 6.23% and 7.21%., respectively.

The σ of polymer chains is a significant factor in determining the conformational regimes NP surfaces, which strongly dictate the assembly behavior of polymer grafted particles. The

structural conformations of grafted BCP chains depends on the distance (l) between adjacent polymer ligands on the NPs. Assuming an individual BCP chain size occupies the space of a circular 'blob' with a radius equal to half of the distance between adjacent chains, the l for copolymer ligands on the surface of Au NPs were estimated to be 1.4, 2.8, 1.3, 2.4 nm for NS_{10}-PS_{130}-*b*-PEO_{45}, NS_{10}-PS_{421}-*b*-PEO_{45}, NS_{60}-PS_{130}-*b*-PEO_{45}, and NS_{60}-PS_{421}-*b*-PEO_{45}, respectively For simplification, the radius of gyration of the BCP chain, R_g, is set equal to R_0 of PS blocks. (R_0 can be found in Table 3.3) If $R_0/l \leq 1$, adjacent polymer chains do not overlap and form a 'mushroom'-like conformations on the grafting surface. If l is smaller than R_0 ($R_0/l > 1$) individual chains interact with adjacent chains and the PS chains stretch in radial direction away from the particle surface to avoid steric crowding. In this case, the strained conformations decrease with increasing distance from the NP surface. The copolymers in our study are understood to be in a brush state on the surface of the Au nanospheres, as indicated by the $R_0/l \geq 5.2$ for all sizes (Table 3.4). In a brush conformation, interparticle particle interactions resulting from the interpenetration of complementary BCPs are more feasible due to the deformability and flexibility of polymer brushes.

3.3.2 Co-assembly of B-PGNPs

To demonstrate the potential of multiple B-PGNPs to self-assemble into ordered structures, the co-assembly of binary, amphiphilic B-PGNPs, a.k.a. nanoparticle amphiphiiles (NPAMs) was initiated by introducing water into a THF solution of homogeneously mixed building blocks followed by dialysis against water to completely remove THF from the system. As previously mentioned, the addition of water is known to cause energetically unfavorable hydrophobic interactions between PS polymer chains and the solvent, which can facilitate the aggregation of

PGNPs into stable nanostructures. In typical assembly experiments, relatively large B-PGNPs designed with large plasmonic NP cores (~60-80 nm) were mixed with B-PGNPs that contained relatively smaller Au NP cores (~10-20 nm) at various volume ratios (v/v). Table 3.5 shows the binary combinations of Au NPs that were used in co-assembly experiments. Each hybrid building block was modified with amphiphilic PEO-*b*-PS-SH BCPs to ensure entropy was a dominant factor during the assembly process. The co-assembly mixtures of binary building blocks designed with

Table 3.5. Different binary combinations of Au NPs used for co-assembly experiments.

Binary System	D_1	D_2					
A	NS_{10}	NS_{20}	NS_{30}	NS_{60}	NS_{75}	NS_{85}	NS_{100}
	NS_{20}	NS_{60}					
B	NS_{10}	NC_{60}	NTR_{60}	NTO_{60}			
	NS_{30}	NC_{60}					

different BCP lengths are denoted as NP_{D1}-PS_{x1}-*b*-PEO_{y1}**:**NP_{D2}-PS_{x2}-*b*-PEO_{y2}, where NP indicates the NP shape, D_1, and D_2, indicate the diameters, and x_1, y_1, x_2, and y_2 are the corresponding repeating units of individual blocks of tethered BCPs. Binary mixtures of Au NPs modified with the same BCP length are denoted as NP_{D1}**:**NP_{D2}-PS_x-*b*-PEO_y.

In Binary System A, the co-assembly of BCP-PGNPs resulted in the formation of phase-separated vesicles for various binary mixtures. For example, patchy vesicles (PVs) with distinct domains of small and large nanoparticles in the vesicular membrane were produced from the co-assembly of B-PGNPs. SEM images in Figure 3.4a and 3.4b show different types of patchy vesicles produced from the co-assembly of binary nanospheres with different sizes. Relatively large PVs or popcorn-like PVs could be fabricated depending on the size ratio of Au NPs. When large Au NS-PGNPs (60 nm) were co-assembled with 10 nm Au NS-PGNPs, patchy vesicles with

average diameter sizes up to several micrometers in length were observed. Close inspection of SEM images with broken vesicle membranes revealed their hollow nature. When 60 nm Au NS-PGNPs were co-assembled with 20 nm Au NS-PGNPs, the co-assembly process produced unique "popcorn-like" clusters and vesicle structures, where the domains of the small and large NPs are much smaller Figure 3.4c and 3.4d. The formation of patchy and popcorn vesicles was characterized by the change in hydrodynamic diameters from DLS measurements. Figure 3.4e, shows an increase in the hydrodynamic diameter of particles in the assembly system before and after assembly, which confirmed the formation of vesicles occurred in solution.

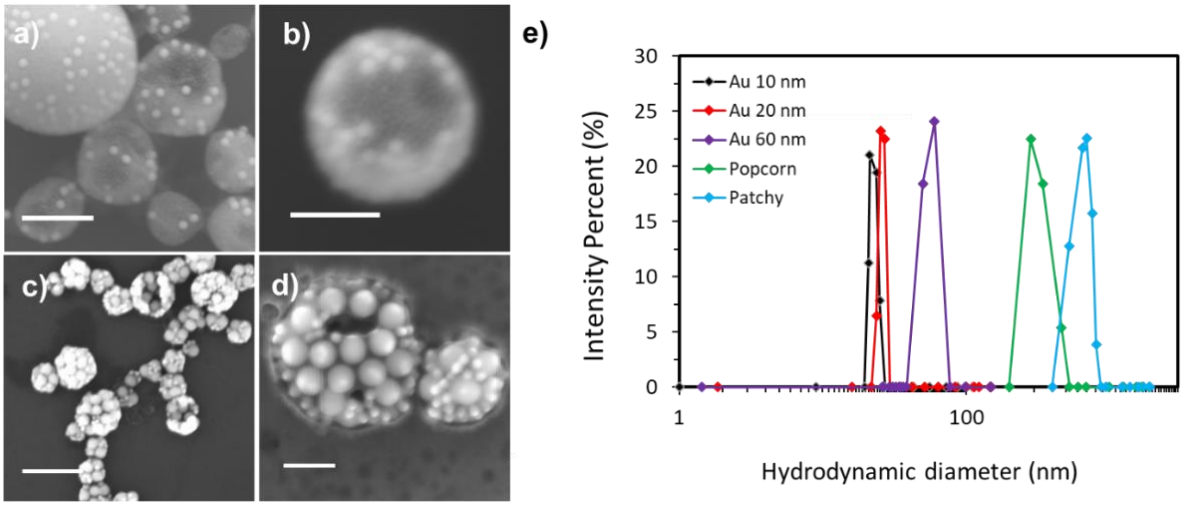

Figure 3.4 Representative SEM images of patchy vesicles assembled from a binary mixture of (a, b) 10 nm and 60 nm and (c, d) 20 nm and 60 nm Au nanospheres grafted with PS_{421}-b-PEO_{45} copolymer ligands. Scale bars: 500 nm (a), 300 nm (b), 200 nm (c), 100 nm (d). (e) DLS spectrum of modified Au NPs before and after self-assembly.

The segregation of Au NP with distinct sizes also occurred in Binary B when small B-PGNPs were mixed with different anisotropic shapes. Using Au NC as an example, qualitatively similar vesicle structures with a patchy morphology were observed when 10 nm Au NC-PGNPs were

mixed with large Au NC-PGNPs. Figure 3.5a and 3.5b display representative SEM images of vesicle membranes with patches of 60 nm Au nanocubes surrounded by patches of 10 nm Au nanospheres, which were both modified with thiol-terminated PS_{211}-*b*-PEO_{45}. SEM images show patchy vesicles contained wrinkled surface textures, which is a common feature of vesicular assemblies and suggests that the assemblies have a hollow cavity. Popcorn-like structures and irregular aggregates were produced when 60 nm Au NC-PGNPs were co-assembled with larger Au NS-PGNPs (Figure 3.5c and d)

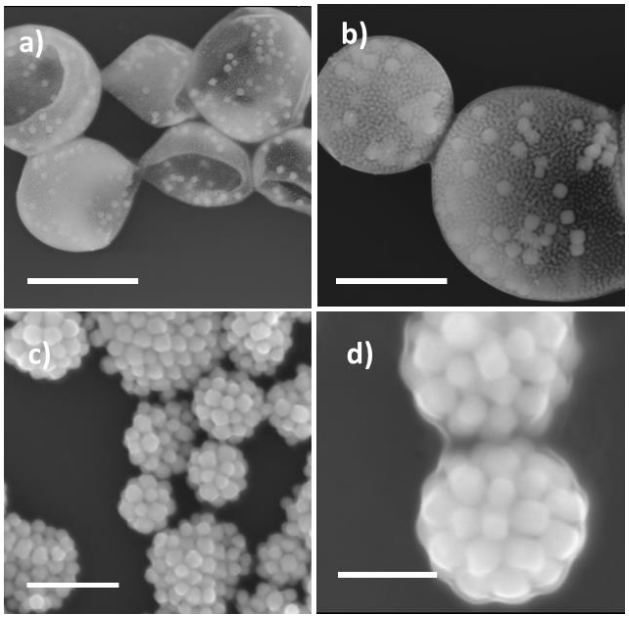

Figure 3.5 Large are and close-up SEM images of patchy vesicles assembled from a binary mixture of (a, b) 10 nm Au NS and 60 nm Au NC grafted with PS_{211}-b-PEO_{45} and (c, d) 30 nm Au NS and 60 nm Au NC grafted with PS_{130}-b-PEO_{45} copolymer ligands. Scale bars: 1 μm (a), 500 nm (b), 400 nm (c), and 200 nm (d).

We hypothesized that the lateral phase separation of small and large B-PGNPs in the vesicle membrane was due to depletion effects which was derived from Asakura and Oosawa's theory on

the depletion-driven assembly of hard spheres in a polymer solution. In their system, the free energy is purely entropic, and dependent only on the center of each polymer's accessibility to the volume.[90,91] Based on this argument, depletion effects could arise as smaller B-PGNPs become excluded from the volume of large PGNPs. Thus, small B-PGNPs serve as depletants to induce short-range attraction between large b-PGNPs. However, our system is conceptually different due to the dominant role of entropy during assembly. In this case, the conformational entropy of copolymers in small B-PGNPs increases during their exclusion, which reduces the overall free energy of the system. Therefore, the lateral phase separation of small and large BCP-PGNPs is mainly attributed to the conformational entropy gain of the grafted polymers. In addition to the dominant role of thermodynamics, the co-assembly behavior of PGNPs is also affected by kinetic factors (i.e. entanglement of polymer chains).[89] To probe the kinetics and understand the underlying assembly mechanism, a time-dependent study was conducted on the formation of phase-separated vesicles, which is discussed in detail in the next chapter (see section 4.3.3).

3.3.3 Effect of BCP length on the co-assembly behavior of B-PGNPs

BCP length is a critical factor in the self-assembly behavior of PGNPs. Therefore, we modified Au NPs in Binary System A and B with identical or mismatched lengths of BCPs. We examined the resulting assemblies of building blocks functionalized with different copolymers to understand how the length of copolymers impacts the co-assembly behavior and phase separation of B-PGNPs with distinct sizes. Using Binary System A as an example, we systematically grafted thiol-terminated PEO-*b*-PS copolymers with M_n of 13.5 K, 23.9 K, and 45.8 K onto the surfaces of NS_{10} and NS_{60}. To optimize assembly conditions, the volume ratio of small and large B-PGNPs (v_s: v_L) in binary mixtures where v_s: and v_L: indicate volume ratios of PGNPs with smaller and large Au

NPs, respectively. SEM images in Figure 3.6 show the resulting assemblies of different binary mixtures for v_s: v_L= 1:1. When one or both building blocks were tethered with BCPs consisting of relatively long PS chains (~M_w), PVs were produced from binary mixtures of NS_{10}-PS_{421}-*b*-PEO_{45}:NS_{60}-PS_{211}-*b*-PEO_{45}, NS_{10}-PS_{130}-*b*-PEO_{45}:NS_{60}-PS_{421}-*b*-PEO_{45}, NS_{10}-PS_{211}-*b*-PEO_{45}:NS_{60}-PS_{421}-*b*-PEO_{45}, NS_{10}:NS_{60}-PS_{421}-*b*-PEO_{45}. Outside of this criterion, SEM images show small clusters or complete segregation between different sizes of B-PGNPs, which suggests the formation of PVs depends on the BCP length. NS_{10}-PS_{211}-*b*-PEO_{45}:NS_{60}-PS_{421}-*b*-PEO_{45} and NS_{10}:NS_{60}-PS_{421}-*b*-PEO_{45}.

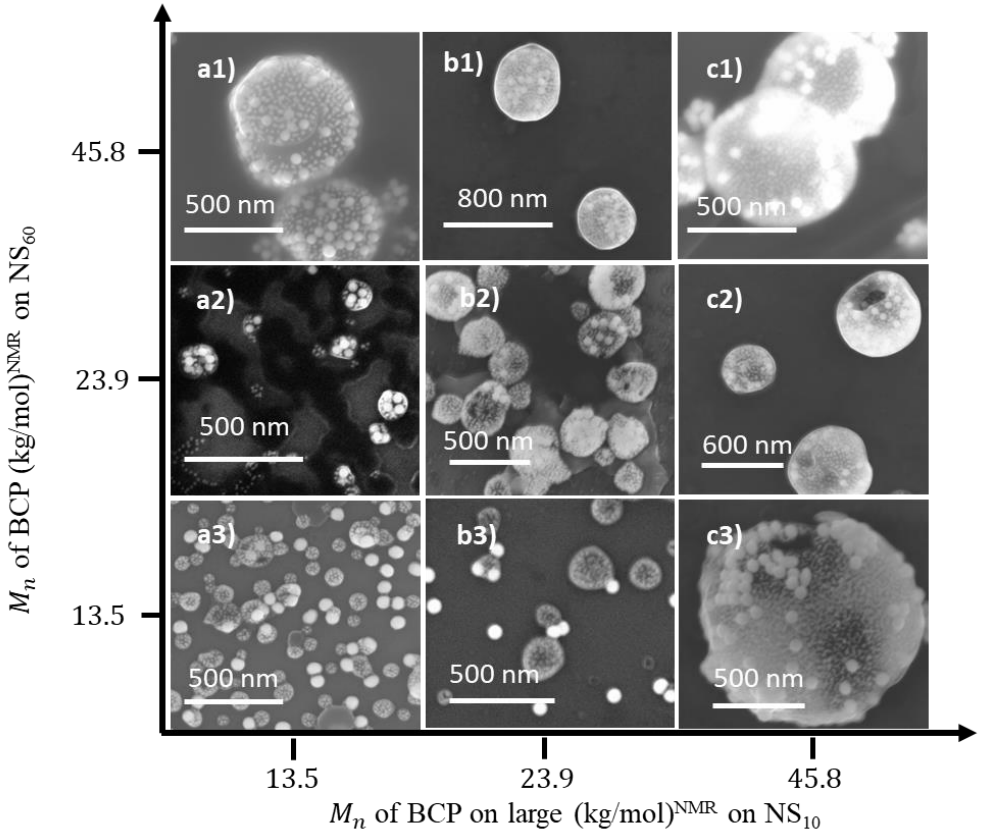

Figure 3.6 SEM images of the resulting assemblies produced from binary mixtures of 10 nm and 60 nm gold nanospheres grafted with different BCP lengths. Binary mixtures were prepared at a 1:1 volume ratio.

It is well known that the hydrophobic polymer length strongly dictates the mobility of inorganic nanoparticles in the solution-based assembly strategy. Therefore, it is possible that during the reorganization of polymer chains on NS surfaces, BCPs with longer hydrophobic chains provided sufficient conformational flexibility needed for the formation of vesicles. A systematic investigation on the effect of BCP length on small and large Au NP was also conducted at v_s: v_L = = 1:3 and 3:1. The effect of BCP length at each volume ratio is summarized in phase-like diagrams in Figure 3.7. The formation of vesicles drastically increases as the volume ratio v_s: v_L changes from 1:3, 1:1, and 3:1. At 1:3 volume ratio, the formation of vesicles significantly depended on the length of BCPs on both NS_{10} and NS_{60}. For instance, a heterogeneous mix small and large B-PGNPs in vesicular membranes was only observed for NS_{10}-PS_{211}-*b*-PEO_{45}:NS_{60}-PS_{421}-*b*-PEO_{45} and NS_{10}:NS_{60}-PS_{421}-*b*-PEO_{45} (Figure 3.7a). At v_s: v_L = 1:1 and 1:3 most binary combinations produce patchy vesicles (Figure 3.7b and c).

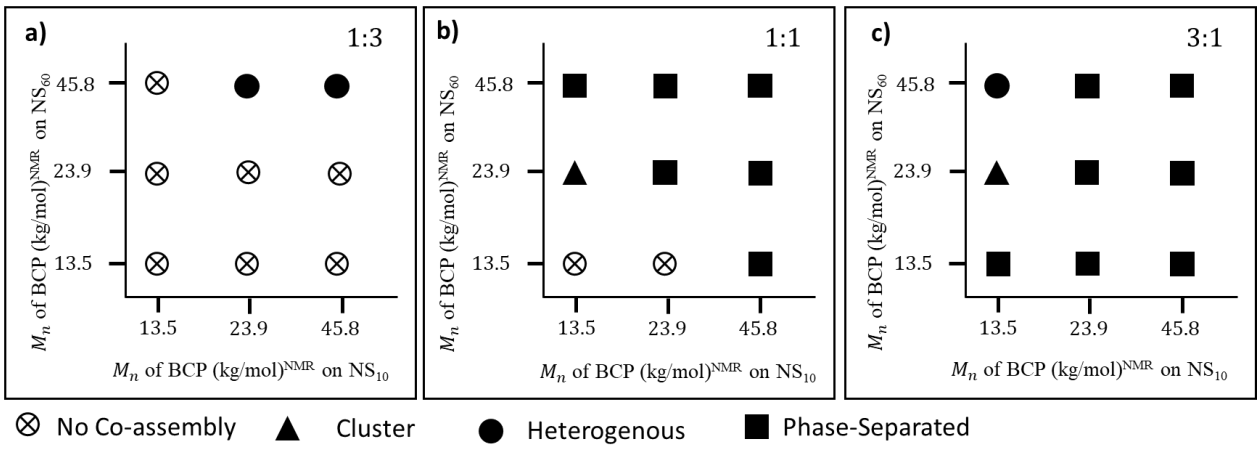

Figure 3.7 Phase diagrams of different assembly morphologies produced from binary mixtures of 10 nm and 60 nm gold nanospheres grafted with different BCP lengths for 3 different volume ratios of small to large B-PGNPs, v_s: v_L including 1:3 (a) 1:1 (b) and 3:1 (c).

We also examined the effect of BCP length in Binary system B for a mixture of large Au nanocubes and small Au nanospheres (Figure 3.8). When the polymer length increased on NC_{60} and the polymer length on NS_{10} was held constant at a relatively short BCP length of NS-10-PS_{97}-*b*-PEO_{45}, the co-assemblies of PGNPs transition from 2D chain aggregates to 2D clusters, and eventually vesicles (Figure 3.8a-c). In contrast, when NS_{10} was held constant at a long BCP length of PS_{652}-b-PEO_{82}, vesicles with a uniform size distribution and enhanced structural integrity were observed as the BCP length increased on NC_{60}. UV -Vis spectra of the resulting assemblies in Figure 3.8d-f) show the split plasmonic peaks red-shifted as the BCP length increased (Figure 3.8g). The observed transition from aggregates to the formation of stable vesicles, suggests that the relatively long BCPS provided a higher degree of stabilization, leading to the organization of PGNPs within vesicular membranes . Like Binary System A, shorter BCPs led to the formation of aggregates that lacked a well-defined vesicular structure. The observed morphological transition to hybrid vesicles at longer BCP lengths is likely attributed to the increased surface coverage and steric hindrance provided by longer block copolymers, which also suggests that the observed trend may be general for a range of different anisotropic NPs. Further exploration is needed to determine the exact assembly mechanisms of binary B-PGNPs in solution.

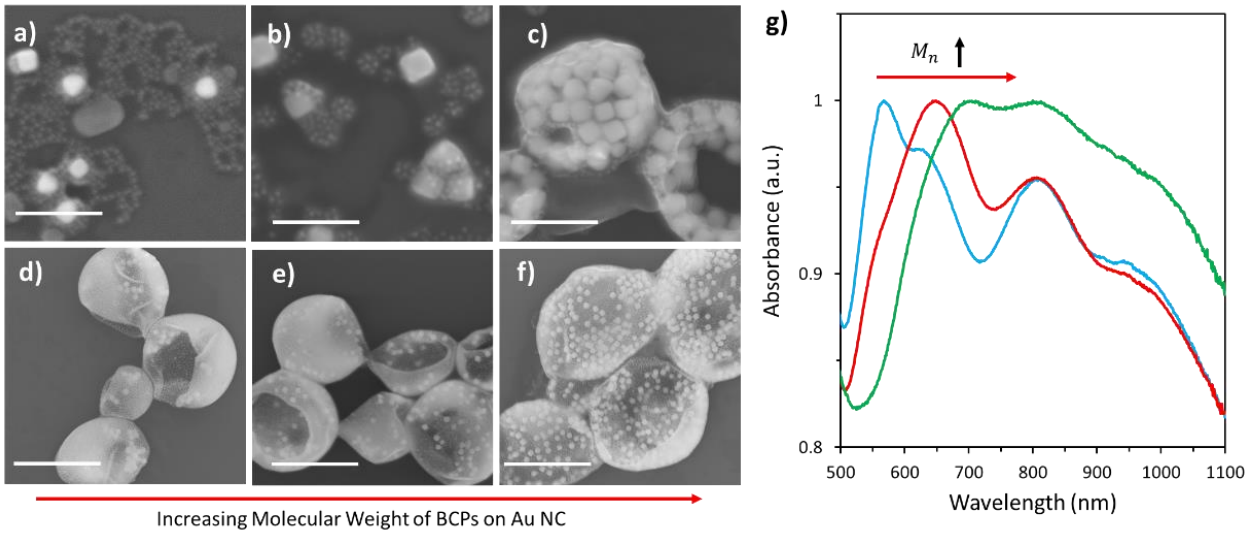

Figure 3.8 The effect of BCP lengths grafted to Au NC on the co-assembly behavior. SEM images of the resulting assemblies produced from binary mixtures of NS-10-PS_{97}-b-PEO_{45} mixed with (a) NC-60-PS_{97}-b-PEO_{45} (b) NC-60-PS_{250}-b-PEO_{45} (c) NC-60-PS_{652}-b-PEO_{82} and of NS-10-PS_{652}-b-PEO_{82} mixed with (d) NC-60-PS_{130}-b-PEO_{45} (e) NC-60-PS_{250}-b-PEO_{45} (f) NC-60-PS_{652}-b-PEO_{82}. Scale bars: 300 nm (a, c) , 200 nm (b) 1 μm (d-f). (g) corresponding UV-Vis absorption spectrum of NS-10-PS_{652}-b-PEO_{82} grafted with different BCP lengths.

3.3.4 Effect of Feeding Ratio on the Vesicle Morphology

In solution-phase, the ratio of amphiphilic copolymers to B-PGNPs influences the assembly process and final morphology of co-assembled structures. Therefore, it was important to consider the effect of the volume fraction of small and large B-PGNPs in solution on the assembly process. SEM images in Figure 3.9 present different assemblies of binary B-PGNPs modified with the same BCP length at v_s: v_L = 1:3, 1:1, and 3:1. At a constant molecular weight of BCPs, the volume ratio has a noticeable impact on the vesicle morphology. As the feeding ratio of small B-PGNPs to large B-PGNPs increases (bottom to top), SEM images show a morphological transition from heterogeneous to patchy vesicles for M_n = 23.9 K, 45.8K, and 71.5 K. At 1:3, small and large BCP-

PGNPs are evenly distributed in the vesicular membrane. At $v_s: v_L$ of 1:1 and 3:1, vesicular membranes are visibly patchy with distinct domains of small and large BCP-PGNPs.

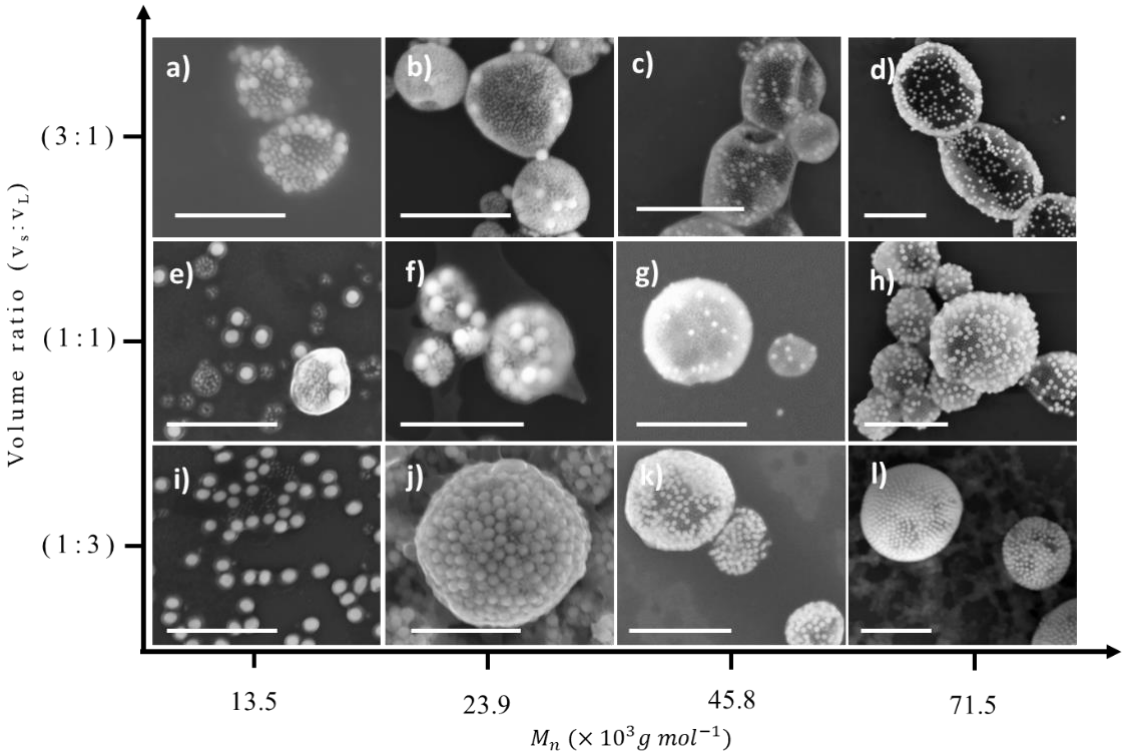

Figure 3.9 The effect of feeding ratio on the formation of hybrid vesicles in Binary System A. Representative SEM images of the resulting assemblies produced from B-PGNPs with 10 nm and 60 nm gold nanospheres at a 3:1 volume ratio of small and large B-PGNPs. Scale bars: 500 nm (a, b, e, i, j), 1 μm c, d, g, h, k, l), and 400 nm (f).

When relatively long copolymers were used as ligands for NS_{10} and NS_{75}, the lateral segregation of NPs became even stronger. SEM images in Figure 3.10 display vesicles produced from the co-assembly of NS_{10}:NS_{75}-PS_{421}-*b*-PEO_{45} and NS_{10}**:**NC_{75}-PS_{652}-*b*-PEO_{82} at different volume ratios. The binary BCP-PGNPs drastically phase-segregated to form vesicles with large patchy domains as the volume ratio of small to large B-PGNP increased, which eventually resulted in complete segregation within vesicle structures. For instance, large spherical Au NPs visibly reside inside the hollow cavities rather than being dispersed within the vesicular membrane of

yolk/structures at v_s: v_L = 4:1 in Figure 3.10d and 3:1 in Figure 3.10f. These hybrid vesicles are referred to as yolk/shell morphology (YSVs), which include large B-PGNPs (the yolk) inside the hollow cavities of vesicular membranes containing small B-PGNPs (the shell). Scanning electronic microscope (SEM) image of occasionally broken m-YSVs shows that there is an empty space between the encapsulated NPAMs and vesicular membranes, indicating the yolk/shell morphology of the vesicles Figure 3.10g. Over 90% of the vesicles produced from NS_{10}**:**NC_{75}-PS_{652}-*b*-PEO_{82} contained at least one yolk and the average number of yolks per shell was estimated to be ~3.1. Figure 3.10h shows the distribution of yolk number per shell in the vesicles.

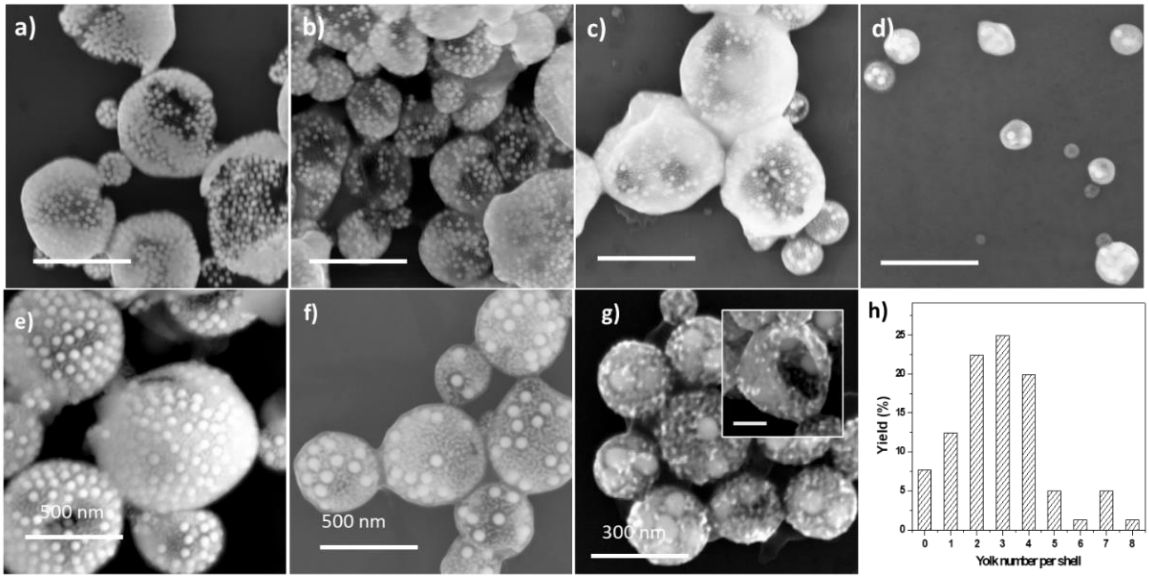

Figure 3.10 Representative SEM images of (a, b) heterogeneous vesicles, (c) patchy vesicles, (d) yolk/shell vesicles produced from the co-assembly 10 nm and 75 nm Au NSs grafted with with PS_{421}-b-PEO_{45} copolymer ligands. The NPAMs were assembled from a binary mixture of NPAMs with varying feeding ratios of small to large B-PGNPs (μL): 4:1 (a) 3:1 (b), 1:1 (c) 1:3 (d). All scale bars: 1 μm.

Yolk/shell vesicles were also observed for co-assembly experiments with other copolymer grafted anisotropic Au NPs at high yields. Figure 3.11a, 3.11b, and 3.11c. displays YSVs produced from binary mixtures comprised of NC, NTO, and NTR, respectively. All anisotropic Au NPs

were modified with PS_{652}-*b*-PEO_{82} and co-assembled with NS_{10}-PS_{652}-*b*-PEO_{82}. Close inspection of SEM images show that the large NP cores are randomly distributed or centrally located inside the hollow cavity of the membranes. The average number of yolks per shell was estimated to be ~6.8, ~17.4, and ~16.8 for NC_{60}:NS_{10}-PS_{130}-*b*-PEO_{45}, NTR_{60}-PS_{130}-*b*-PEO_{45}:NS_{10}-PS_{652}-*b*-PEO_{82}, and NTO_{60}-PS_{130}-*b*-PEO_{45}:NS_{10}-PS_{652}-*b*-PEO_{82}, respectively. Figure 3.11d shows the distribution of yolk number per shell in the vesicles for each binary mixture. The formation of hybrid vesicles composed of spherical or anisotropic nanoparticles indicates that the co-assembly of B-PGNPs in solution with significantly different dimensions is a versatile approach to feasibly integrate a range of different types of building blocks into complex hybrid nanostructures.

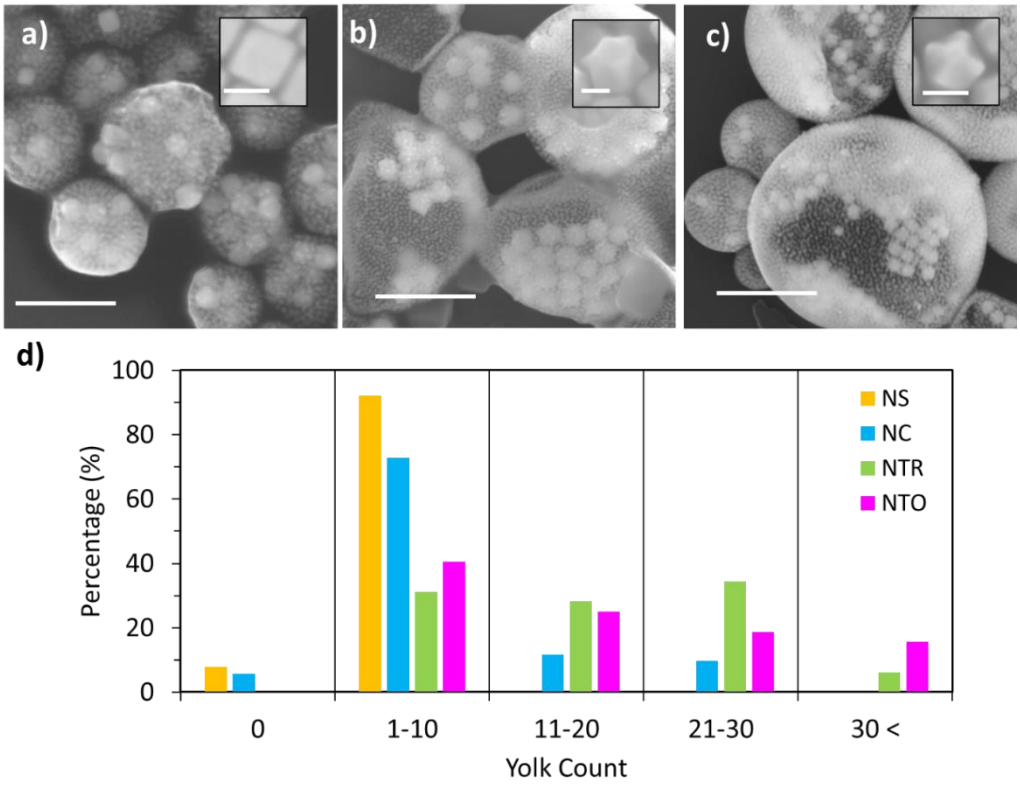

Figure 3.11 Representative SEM images of yolk/shell vesicles produced from the co-assembly of 10 nm nanospheres and relatively larger gold nanoparticles with various geometric shapes: a) cubic b) trisoctahedron and c) transitional type. Scale bars: 300 nm (a) 500 nm (b, c) and all inset scale bars: 50 nm. (d)

3.4 Conclusion

Au NPs with various geometric shapes in binary mixtures of B-PGNPs can co-assemble into hybrid vesicles with well-defined morphologies, including patchy vesicles (PVs) with distinct domains of small and large B-PGNPs and yolk/shell vesicles (Yvs) with large B-PGNPs randomly distributed or centrally located inside the hollow cavities of vesicular membranes containing small B-PGNPs. The formation of these hybrid assemblies was observed for several building block combinations of B-PGNPs including binary mixtures of spherical Au NPs with distinct sizes and binary mixtures composed of spherical and non-spherical Au NPs with distinct sizes. This work shows that the co-assembly of multiple B-PGNPs is a useful strategy to design complex structures by simply manipulating the structural parameters of Au NPs and length of polymer grafts, in addition to the volume ratio of B-PGNPs in solution. Furthermore, the concurrent self-assembly of binary PGNPs into vesicles represents a promising approach for the controlled formation of multicomponent vesicles with increased complexity, which is attractive for a variety of applications including drug delivery and biosensors.

Chapter 4: NP size and Concentration Effects on Co-assembled Vesicles

This chapter is adapted from the manuscript published in the following article: Lamar, C., Liu, Y., Yi, C., Nie, Z. Entropy-driven segregation and budding in hybrid vesicles of binary nanoparticle amphiphiles, Giant, 2020, 1, 100010.

Overview. Self-assembly of giant building blocks beyond conventional molecules offers tremendous opportunities for the fabrication of new-generation structural materials. In the previous chapter, we reported the size segregation phenomenon in the vesicular self-assembly of binary nanoparticle amphiphiles (NPAMs) consisting of block copolymer-grafted nanoparticles (BCP-PGNPs) in solution. This chapter aims to establish a predictive framework for the co-assembly of BCP-PGNPs with spherical gold nanoparticles (Au NS). Depending on the relative size and concentration, binary BCP-PGNPs with distinctive sizes assemble into hybrid vesicles with different morphologies, namely, homogeneous vesicles, patchy vesicles, and yolk/shell vesicles. The segregation of NPAMs confined within or escaped from the vesicular membrane is driven by the conformational entropy gain of end-grafted copolymer ligands. The effect of NPAM size and concentration on the morphological transition of vesicles is mapped in a phase diagram. Moreover, a mechanism for the observed vesicular fusion/budding is proposed to illustrate the formation of uniform vesicles with yolks inside.

4.1 Introduction

Self-assembly of amphiphilic molecules (e.g., lipids, peptides, block copolymers) offers great opportunities for constructing functional nanoarchitectures, such as micelles, vesicles, sheets, tubes and nanowires.[92–96] These nanostructures are attractive for applications in biomedical

imaging[97], drug delivery[98], nano-reactors[60], and tissue engineering[99]. To meet the rising demand for novel materials, efforts have been made to incorporate inorganic nanoparticles (NPs) with different sizes, shapes and compositions into organic assemblies to achieve composite nanostructures with advanced functionalities.[81] At this frontier, NP amphiphiles (NPAMs) consisting of polymer-grafted inorganic NPs have emerged as an intriguing class of building blocks for assembling next-generation functional nanocomposites.[53,54,100–108] In analogy to amphiphilic molecules, BCP-PGNPs have the ability to self-organize into a wealth of well-defined hybrid nanoarchitectures, such as unimolecular micelles, clusters, chains, tubes, and vesicles in selective solvents.[109,110] Especially, such giant amphiphiles naturally combine the unique physical properties of organic polymers and inorganic NPs in one system, enabling better control over NP organization and coupling interaction (e.g., plasmon-plasmon, plasmon-exciton, and magnetic-magnetic) between NPs.[55,111,112]

A variety of NPAM assemblies (e.g., plasmonic vesicles) with tunable collective optical and magnetic properties have been demonstrated for controlled release of therapeutic drugs, efficient multimodality imaging (e.g., photothermal, photoacoustic, and magnetic resonance imaging) and therapy (e.g., photothermal, photodynamic, and chemotherapy) of cancers (see Chapter 1 section 1.4). The dimension of NPAMs (inorganic core plus polymer grafts) is usually in the range of ~10–120 nm, which is one to two orders of magnitude larger than molecular amphiphiles.[104] Because of their giant size (relative to molecules) and complex geometry, NPAMs exhibit assembly behaviors that are distinctive from amphiphilic molecules from both thermodynamic and kinetic aspects.[54,89,106] For instance, recent studies showed that the concept of classic molecular packing parameter, which is widely used to guide the rational design of molecular self-assembly, is not always successful in predicting the morphologic transition in B-

PGNPs assembly.[54] In contrast to molecular assembly, the kinetic pathways of B-PGNPs assembly can be readily manipulated to generate nanostructures with different morphologies via microfluidic techniques.[113] Moreover, because of the constrain of grafted ends, the conformational entropy of polymer ligands plays a crucial role in determining the phase separation of NPAMs and amphiphilic block copolymers in vesicular membranes.[89,114] Nevertheless, to date the assembly behavior of NPAMs is still not well understood. Moreover, there has been no study on the macro-phase separation of NPAM blends in solution.

In this chapter, we report the polymer conformational entropy-driven colloidal segregation in the self-assembly of binary mixture of polymer-grafted NPs with distinctive sizes to generate hybrid vesicles with different morphologies. As shown in Figure 4.1, amphiphilic block copolymer-grafted gold NPs (AuNPs) with different size combinations serve as NPAMs for assembly in selective solvents. Au NPs were surface-modified with a typical block copolymer (BCP): thiol terminated poly (ethylene oxide) – *block* – polystyrene (PEO-*b*-PS-SH). A series of binary systems with varying sizes and concentrations were systematically studied to understand the phase behavior of NPAMs. Depending on their relative molar concentration and size, binary NPAMs assembled into hybrid vesicles with four distinctive morphologies including, homogeneous vesicles (HVs) with binary NPAMs randomly distributed in the membrane, patchy vesicles (PVs) with large NPAMs segregated in the membrane, multi-yolk/shell vesicles (m-YSVs) with several large NPAMs segregated into the hollow cavity, and single-yolk/shell (s-YSVs) with single yolk per shell (Figure 4.1). A phase diagram was plotted to summarize the size and concentration effect of NPAMs on the structural transition of hybrid vesicles. Additionally, we further studied the time-dependent morphological evolution of YSVs and proposed a formation mechanism involving the fusion and budding of vesicles. This work provides new insights into the

use of polymer-grafted NPs for the fabrication of functional nanocomposites with potential applications in such as biomedical imaging, drug delivery, and biosensing.

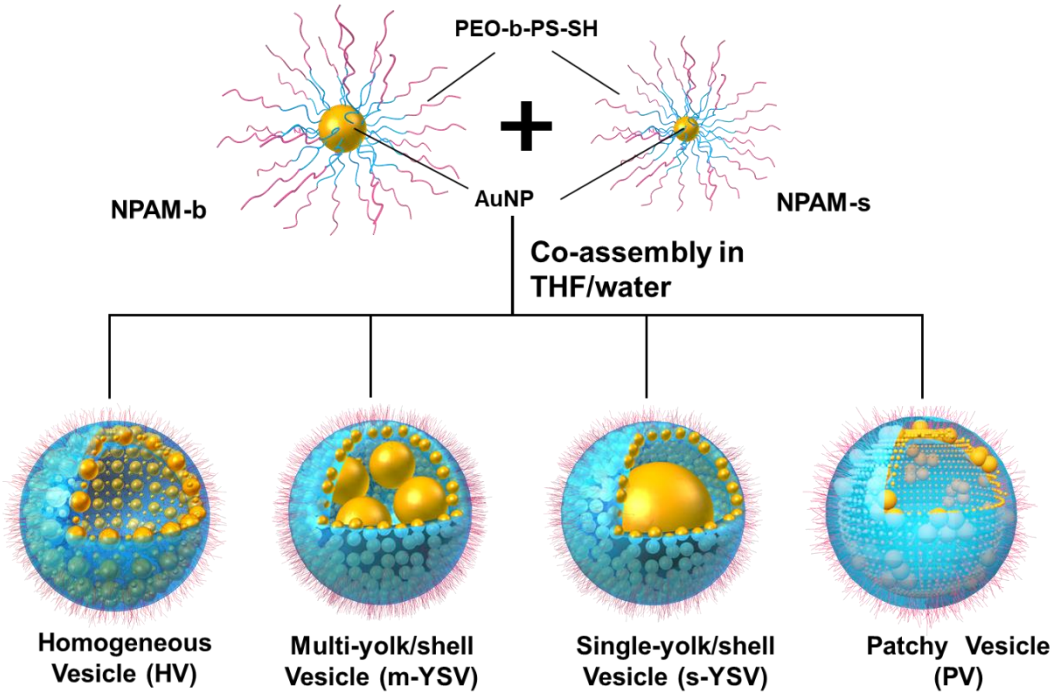

Figure 4.1 Schematic illustration of the co-assembly of binary mixtures of NPAMs with different dimensions into hybrid vesicles with distinct morphologies.

4.2 Experiments

4.2.1 Materials

Styrene, azobis(isobutyronitrile) (AIBN), 4-cyano-4-(phenylcarbonothioylthio) pentanoic acid (CPPA), tetrahydrofuran (THF), dimethylformamide (DMF), Gold(III) chloride trihydrate (HAuCl4.3H2O, ≥99.9%), ascorbic acid (AA, ≥99.0%), sodium borohydride ($NaBH_4$, 98%), cetyltri-methylammonium bromide (CTAB, ≥99%), and cetyltrimethyl-ammonium chloride (CTAC, 25 wt% in water) were all obtained from Sigma-Aldrich and used as received. Deionized

water (HPLC grade) from Fisher Scientific was used in all the experiments. Polystyrene-b-poly (ethylene oxide) (PS-b-PEO) without functional groups was purchased from Polymer Source, Inc. Styrene was distilled under vacuum prior to use and stored in a freezer at −20 °C. AIBN was recrystallized from ethanol.

4.2.2 Synthesis of Gold Nanospheres

AuNPs were synthesized using a successive, seed mediated growth of single-crystal nanospheres with minor modifications. See Chapter 3, section 3.2.2 for synthetic procedures.

Table 4.1 The type of seeds and volume of seed solution used in the synthesis of spherical AuNPs with targeted diameters.

Diameter of Nanosphere	Type of Seed	Volume (μL)
10 nm	Cluster	800
20 nm	Cluster	250
30 nm	15-nm sphere	90
60 nm	15-nm sphere	60
75 nm	15-nm sphere	40
85 nm	15-nm sphere	20
100 nm	60-nm sphere	10

4.2.3 Surface Modification of Gold Nanospheres with Copolymers

Thiol-terminated PS_{652}-b-PEO_{82} were synthesized using reversible addition-fragmentation chain transfer (RAFT) polymerization reported previously (see Chapter 2 section 2.2.2). 2 mg of thiol-terminated copolymers were dissolved in 10 mL of dimethylformamide (DMF). A 10 mL aqueous solution of AuNPs was concentrated into 100 μL by centrifuging. The concentrated AuNP solution was slowly added into the copolymer solution in DMF while shaking. Subsequently, the mixture was sonicated for 1 h to avoid aggregation and then kept undisturbed for 24 h to complete

the ligand exchange. The solution was centrifuged 6-8 times and re-dispersed in THF each time to remove free BCPs from the solution. The resulting copolymer grafted AuNPs were redispersed in 1.5 mL THF and served as stock solutions for the assembly of NPAMs. Molecular weights characterized by gel permeation chromatography (GPC) and ^{1}H NMR are 67.9 kg/mol and 71.5 kg/mol, respectively. From GPC measurements using polystyrene (PS) standards, the polymer sample has a polydispersity index (M_w/M_n) PDI of 1.07. The root mean square end-to-end distance of PS blocks was estimated for a series of Au NP sizes, which was calculated from $R_0 = bN^{0.5}$, where b is the Kuhn length (b = 0.18 mm for PS) and N is the number of Kuhn segments. The length for other BCPs and additional characterization details can be found in Chapter 3 Table 3.3 (see section 3.2.3).

4.2.4 Self Assembly of B-PGNPs

The concentration of NPAMs with different sizes in stock solutions was determined by quantifying the amount of Au element using inductively coupled plasma mass spectrometry (ICP-MS). The solutions of two different NPAMs in THF were mixed in a predetermined ratio and the mixture was dialyzed against water using dialysis bags for 24 h to remove THF.

4.2.5 Calculation of NPAM Concentrations

Inductively coupled plasma mass spectrometry (ICP-MS) was used to quantify the mass of Au element in each sample. The diameter of AuNPs was estimated by analyzing SEM or TEM images of AuNPs. By assuming a shape of the AuNPs, we calculated the molar concentration, φ of AuNPs in the sample using the following equation:

$$\varphi = \frac{m}{N_A \rho (4/3\pi r^3)} \text{ (mol)}$$

Where NA, m, ρ and r is the Avogadro's number, the mass of Au determined by ICP, the density of bulk gold, and the radius of spherical AuNPs, respectively.

Table 4.2 The concentration (g/mL) of different-sized Au NSs in solution measured from ICP-MS and corresponding calculated molar concentrations (nM).

Au NP size (nm)	Concentration (g/mL)	Concentration (nM)
10	$3.66\ x\ 10^{-5}$	0.60
30	$3.08\ x\ 10^{-5}$	$1.9\ x\ 10^{-2}$
60	$1.12\ x\ 10^{-4}$	$8.5\ x\ 10^{-3}$
75	$1.33\ x\ 10^{-4}$	$5.2\ x\ 10^{-3}$
100	$9.39\ x\ 10^{-5}$	$1.5\ x\ 10^{-3}$

4.2.6 Characterizations

^{1}H NMR. ^{1}H NMR spectra were recorded with a Bruker AV-400 Mhz high resolution NMR spectrometer in $CDCl_3$.

Gel permeation chromatography (GPC). GPC measurements were performed using a Viscotek system equipped with a refractive index detector (RI 410) and four columns at 45 ^{o}C. THF was used as the eluent at an elution rate of 1 mL min^{-1}, and polystyrene standards were used for calibration.

Thermogravimetric Analysis (TGA). TGA was used to characterize the grafting density of BCPs on the surface of the NPs. A10.0 mL stock solution of building blocks was centrifuged for 6-8 cycles in THF to remove excess BCPs. After removal of the supernatant, samples were left to dry for 1 hr to evaporate the remaining solvent. The experiments were carried out in an Argon atmosphere with the following temperature program: heat from 100 ^{o}C to 700 ^{o}C at a scan rate of 10 ^{o}C / minute with a purge rate of 20 mL/minute. During the scan process, the temperature was maintained at 150 ^{o}C for 30 minutes to further remove moisture.

Inductively Coupled Plasma – Mass Spectroscopy (ICP-MS). ICP- MS measurements were collected to determine the concentration of Au NP samples with different sizes. Samples were suspended in 1% aqua regia and diluted with 3% HNO_3 before characterization.

UV-Vis Spectroscopy. The extinction spectra of AuNPs, modified particles, and assembly structures were taken on a PERKIN LAMBDA 35 UV/Vis System.

SEM and TEM imaging. The assembly structures were imaged using a Hitachi SU-70 Schottky field emission gun Scanning Electron Microscope (FEG-SEM) and a JEOL FEG Transmission Electron Microscope (FEG-TEM). Samples for SEM and TEM were prepared by drying ~3-4 μL of aqueous solution of assembly structures on silicon wafers and copper grids at room temperature, respectively.

4.3 Results and Discussion

4.3.1 Hybrid Building Blocks used for self-assembly

We examined the co-assembly of binary B-PGNPs in Binary System A and B. We synthesized monodispersed CTAC-capped Au nanospheres with different diameters and anisotropic nanoparticles, using seed-mediated growth methods. The characterization and analysis of Au NPs are referred to in Chapters 2 (see section 2.3.1) and 3 (see section 3.3.1). To ensure assembly occurs in solution, the surface of AuNPs was functionalized with thiol-terminated PS-*b*-PEO with different number-average weights (M_n) through ligand exchange. Unless noted otherwise, a typical copolymer, PS_{652}-b-PEO_{82}, will be referred to throughout the remaining of this chapter. The root-mean-square end-to-end distance of an unperturbed copolymer chain, $R_0 = nN^{1/2}$, was estimated to be 17.9 nm, where b is the Kuhn length of PS = 0.18 mm and N is the number of Kuhn segments. Untethered free copolymers were removed by centrifugation and the

concentration of residual free copolymers was estimated to be below 10^{-16} M in the final solution. This is ≈ 10^{-6} to 10^{-7} times lower than the concentration of NPs in assembly systems. The resulting NPAMs were dispersed in tetrahydrofuran (THF), a good solvent for the ligands, and demonstrated good colloidal stability in the solution. The solubility parameters for PS, PEO, and THF are 16,6 -20.2, 18.6, and 18.0-19.1$[MP\alpha]^{1/2}$, respectively.

Table 4.3. Characterizations of B-PGNPs with different sized Au NS.

Diameter Au NS	σ (chain/nm^2)	l (nm)	R_0/l
10 nm	0.09	3.3	5.4
30 nm	0.13	2.8	6.5
60 nm	0.23	2.1	8.6
75 nm	0.22	2.1	8.4
85 nm	0.29	1.9	9.6
100 nm	0.26	2.0	9.1

UV-Vis Spectroscopy was used to assess the grafting of BCPs to the Au NP surfaces after modification (Figure 4.2a). For example, the localized surface plasmon resonance (LSPR) peaks of 75 nm particles before and after modification with BCPs exhibited a slight redshift (≈ 12 nm). This suggests that the particle size increased due to the outer layer of grafted polymers on the surface of Au NPs. Using the same procedures in the previous chapter (see section 3.3.1), the grafting densities (σ) of the copolymer ligands on different-sized Au NS were calculated from thermal gravimetric analysis (TGA). For example, 75 nm Au NPs grafted BCPs exhibited a weight loss of 8.50% (Figure 4.2b), which corresponds to a σ of 0.22 chain/nm^2 (Table 4.3). The l for copolymer ligands on the surface of Au NPs were estimated to be in the range of 1.9 nm – 3.3 nm. For simplification, the radius of gyration of the BCP chain, R_g, is set equal to R_0 of PS blocks. The

copolymers in our study are understood to be in a brush state on the surface of the Au nanospheres, as indicated by the $R_0/l \geq 5.4$ for all sizes, which facilitates the effective deformability and flexibility of polymer brushes.

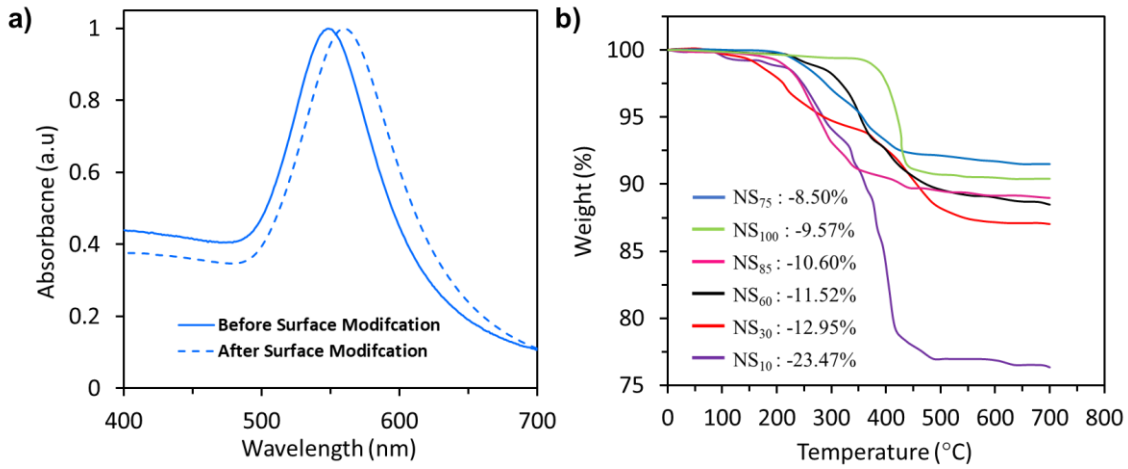

Figure 4.2 Representative UV-Vis spectroscopy curve of 75nm-sized AuNPs before and after surface modification with PS_{652}-b-PEO_{82}. TGA curves of Au NS with different diameters modified with PS_{652} - *b* - PEO_{82} copolymers.

4.3.2 Structural Characterizations of Hybrid Vesicles

The self-assembly of NPAMs was triggered by dialyzing a solution of the NPAMs (either single type or binary mixture) in THF against deionized water. Our previous studies showed that the self-assembly of NPAMs is strongly dependent on the size of NPs and M_n of copolymer ligands.[54] In the previous chapter, we demonstrated that NPs tethered with short BCP chains could not produce co-assembled structures or could only aggregate into small clusters due to the limited mobility of the hydrophobic chains. When M_n of copolymers is sufficiently large, the effect deformability of the chains increases, which allows the hydrophobic chains to adopt new configurations. As a result, NPs with a broad size range can assemble into vesicular structures. Therefore, we chose long PS_{652} - *b* -PEO_{82} copolymers as ligands for the majority of our studies

in binary mixtures. In consistence with reported results, SEM images in Figure 4.3 confirmed that all the copolymer-grafted NPs with different sizes that we studied here (from 10 nm to 100 nm) could assemble into hollow vesicles with a monolayer of densely packed NPs in the membrane, although a small population of incomplete vesicular structures and small clusters were coexisted in the assembly systems of large NPs (Figure 4.3c and d).

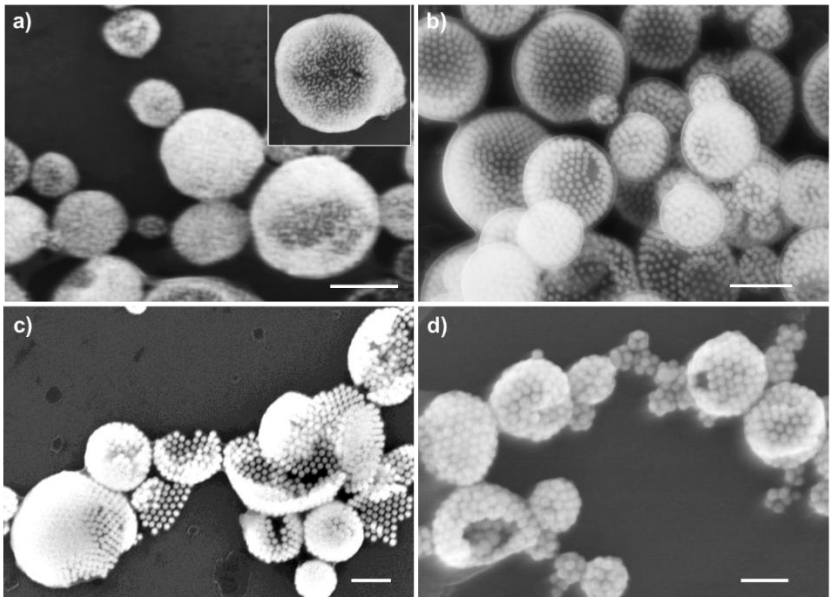

Figure 4.3 Representative SEM images of single-component vesicles assembled from PS_{652}-*b*-PEO_{82}-grafted AuNPs with different sizes: (a) 10 nm, (b) 20 nm, (c) 60 nm and (d) 85 nm. The scale bars: 200 nm (a, b) and 400 nm (c, d).

The co-assembly process generated stable, spherical hybrid vesicles with three typical morphologies, including heterogeneous vesicles (HVs), multi-yolk shell vesicles (m-YSVs), and single-yolk shell vesicles (s-YSVs), patchy vesicles (PVs). The co-assembly mixtures of binary building blocks are all modified with the same BCP and are denoted as D_L/D_S, where D_L and D_S are the size of large and small NPAMs. SEM images in Figure 4.4 show different binary mixtures of NPAMs can produce high-yields of HVs, YSVs, and PVs. For example, D_L/D_S = 30 nm /10 nm produced PVs with segregated domains of small and large NPAMs confined in the membranes,

while D_L/D_S = 60 nm /10 nm produced HVs with a uniform distribution. Moreover, SEM images in Figure show YSVs with multiple yolks produced from D_L/D_S = 80 nm /10 nm and YSVs with a single yolk D_L/D_S = 100 nm /10 nm, respectively). Figure X presents YSVs with a single yolk produced from D_L/D_S = 100 nm /10 nm. We note that in this case, empty vesicles without any yolk are present in Figure 4.4d, which is likely due to the complete consumption of large NPAMs in the mixture.

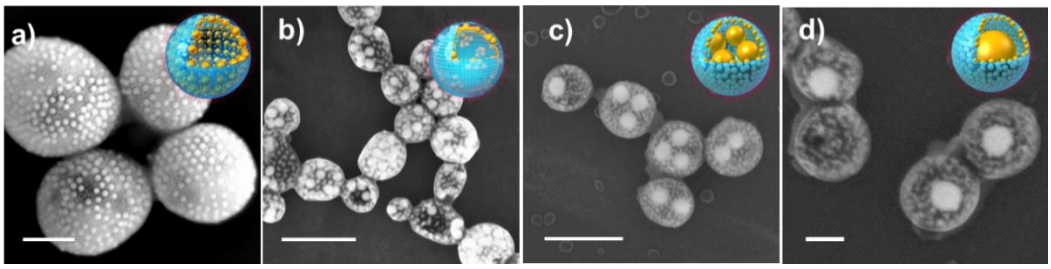

Figure 4.4 Representative SEM images of hybrid vesicles produced from the co-assembly of B-PGNPs. Scale bars: 500 nm (a), 300 nm (b, c), and 100 (d).

To establish a predictive framework, we varied the molar concentrations of small NPAMs at a constant molar concentration large NPAMs and examined the assembly of binary mixtures of NPAMs in solution. Using 10 nm-sized and 75 nm-sized as an example, the molar concentrations of small NPAMs were varied from 0.30 to 0.60 nm, while that of large NPAMs was kept constant at 5.2 x 10^{-3} nM in the mixture. At a lower φS (0.30 nM), the binary NPAM assembly produced PVs with large NPAMs associated together to form small patches within the vesicular membranes (Figure 4.4 a,b). At φS = 0.48 nM, the large NPAMs were segregated into the interior of the vesicles to form m-YSVs with multiple yolks inside (Figure 4.5c). At a higher concentration, φS = 0.60 nM, the binary NPAMs assembled into s-YSVs with a single yolk in each shell (Figure 4.5d). However, ~45% of the vesicles were empty (without any yolk). As previously stated, this is

likely due to complete consumption of large NPAMs in the mixture. The optimization of φS / φL may further increase the yield of s-YSVs.

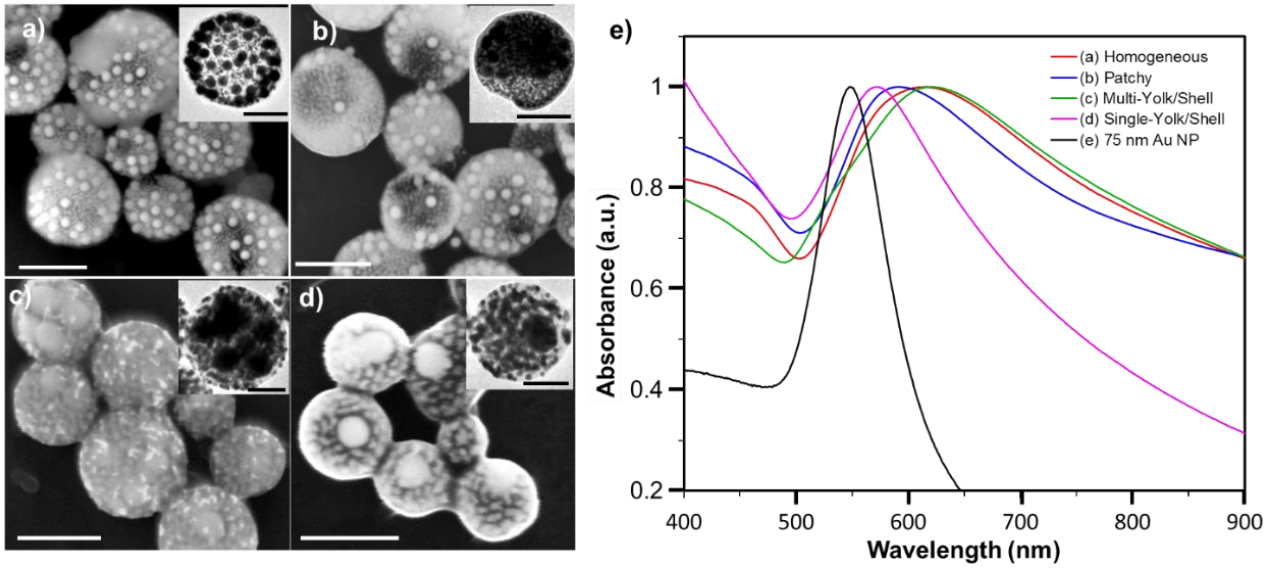

Figure 4.5 (a-d) SEM and TEM images of assembled structures via the co-assembly of binary mixture: Au-10-PS_{652}-b-PEO_{82}/Au-75-PS_{652}-b-PEO_{82} at different concentrations of 10 nm Au NPs: $0.30\,nM$(a), $0.36\,nM$(b), $0.48\,nM$(c), and $0.60\,nM$(d). (e) The corresponding UV-vis spectra of assemblies in (a-d). The scale bars in SEM: 400 nm (a,b) and 200 nm (c,d). The scale bars in TEM: 250 (a,b) and 100 nm (c,d).

The formation of hybrid vesicles with different morphologies is associated with a noticeable redshift in the LSPR band due to the plasmonic coupling interactions between AuNPs (Figure 4.5 e).[115,116] The redshift in LSPR of coupled Au nanospheres, λ, is related to the diameter of NPs, d, as $\Delta\lambda \sim e^{-1/d}$. Thus, the large NPAMs plays a dominant role in determining the optical response of hybrid vesicles. Referring back to characterization of hybrid build blocks, unmodified and modified 75 nm Au NPs produced LSPR peaks at 548 nm and 560 nm, respectively. After self-assembly, the m-YSVs exhibited a larger redshift (~72 nm) in LSPR peak than s-YSVs (~21 nm), due to the close colocalization of large NPAMs inside the shell. Similarly, the segregation of

large NPAMs in small patches of PVs also resulted in a 64 nm redshift in the LSPR peak of the vesicles.

4.3.3 Phase Separation Behaviors in Binary Mixtures of NPAMs

We performed a mechanistic study on the assembly of binary NPAMs into PVs and YSVs in Binary System A. In both cases, we studied the formation process of vesicles using a model system of 10 and 75 nm Au NPs grafted with PS_{652}-*b*-PEO_{82} copolymers. For instance, SEM images of PV formation show the morphologic changes in the vesicle membrane at different time points during dialysis (Figure 4.6a). About 30 minutes after dialysis against water, HVs are present in the system. As time evolves, there is a noticeable change in the distribution of particles in the vesicle membrane. Eventually, the patchy formation was observed after 24 hr. We attribute the driving force of macroscopic segregation of small and large NPs in vesicular membranes to the conformation entropy gain of end-grafted copolymer ligands on the surface of NPs, which differs from depletion-driven segregation of NPs.[116–118] Such entropy-driven phase separation in vesicular membranes was confirmed in the binary assembly system of NPAM and free amphiphilic block copolymers through experiments and simulations in our previous work.[89] Schematics illustrating the cross-section of vesicles and packing of binary NPAMs in the membranes. The mismatch in the effective thickness of vesicular membrane of pristine small and large NPAMs is significant for binary NPAMs with 10 and 75 nm AuNPs. When the binary NPAMs are randomly distributed in the membrane to form HVs, the copolymer chains on the surface of NPs must be compressed or stretched in the direction normal to the membrane due to the influence of neighboring NPAMs (Figure 4.6 b). The stretching/compressing constrain on the conformation of grafted polymer chains can be reduced by laterally segregating equally-sized NPAMs together to form PVs with patchy

domains where the conformational entropy of polymers is maximized (Figure 4.6c). At a high φS / φL , the number of large NPAMs in each vesicle is low and the conformational entropy gain of polymers from patch formation is not sufficient to compensate the interfacial energy loss at the phase boundary of patches. As a result, the large NPAMs segregated from the membrane into the interior of vesicles to lower the free energy of the system resulting in a yolk – shell morphology. (Figure 4.6d)

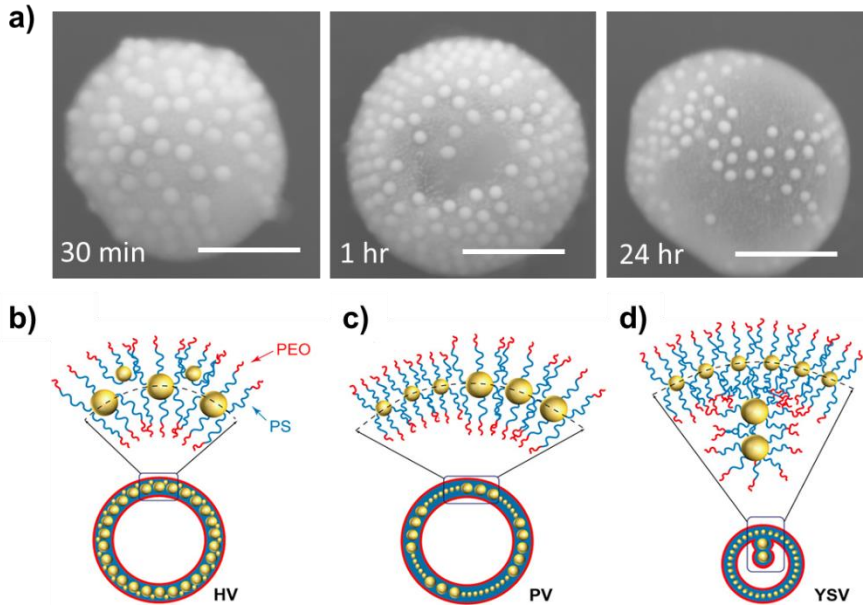

Figure 4.6 (a) SEM images of the assembly structures during the formation of PVs at different time points. (b-d) Schematics illustrating the cross-section of vesicles and packing of binary NPAMs in the membranes. The scale bars are 500 nm.

We also observed the time-dependent assembly process of binary NPAMs into YSVs (Figure 4.7a). After the mixture was dialyzed against water for ~15 min, the binary NPAMs assembled into polydisperse hybrid vesicles with an average size of 319.7 ±159.4 nm (Figure 4.7b). Among them, ~27.5% of the vesicles contained more than 7 yolks per shell and ~49.6% were

empty (Figure 4.7c). As time progressed, the average size of vesicles gradually decreased, and the size distribution became more uniform. The population of small, empty vesicles drastically reduced over time. In the meantime, the yolks were also redistributed more evenly within the vesicle. At ~24 h, the average diameter of the vesicles reduced down to 213.0 ±51.6 nm. More importantly, the fraction of empty vesicles reduced down to ~7.8% and ~87.8% of the vesicles contained ~1–6 yolks. The gradual increase in the uniformity of vesicle size and yolk distribution suggests the fusion of large vesicles with small ones and the budding of large vesicles into smaller yet uniform vesicles containing yolks in the course of forming uniform YSVs. Indeed, TEM images of intermediate assembly structures showed the presence of distorted vesicles with smaller sections of NPAMs budding from the vesicle membrane (Figure 4.8a-f). Moreover, the LSPR bands of the assembly structures drastically blue shifted and then red shifted over time (Figure 4.8g), which further confirms the continuous morphological transformation of vesicles during assembly process illustrated in Figure 4.7d. At the early stage, large vesicles containing many yolks fuse with small ones to reduce the interfacial free energy between vesicles and solvent media. With time, one or more buds develop on the surface of large vesicles. Finally, the buds grow and separate from the parent vesicles to form uniform vesicles.[119]

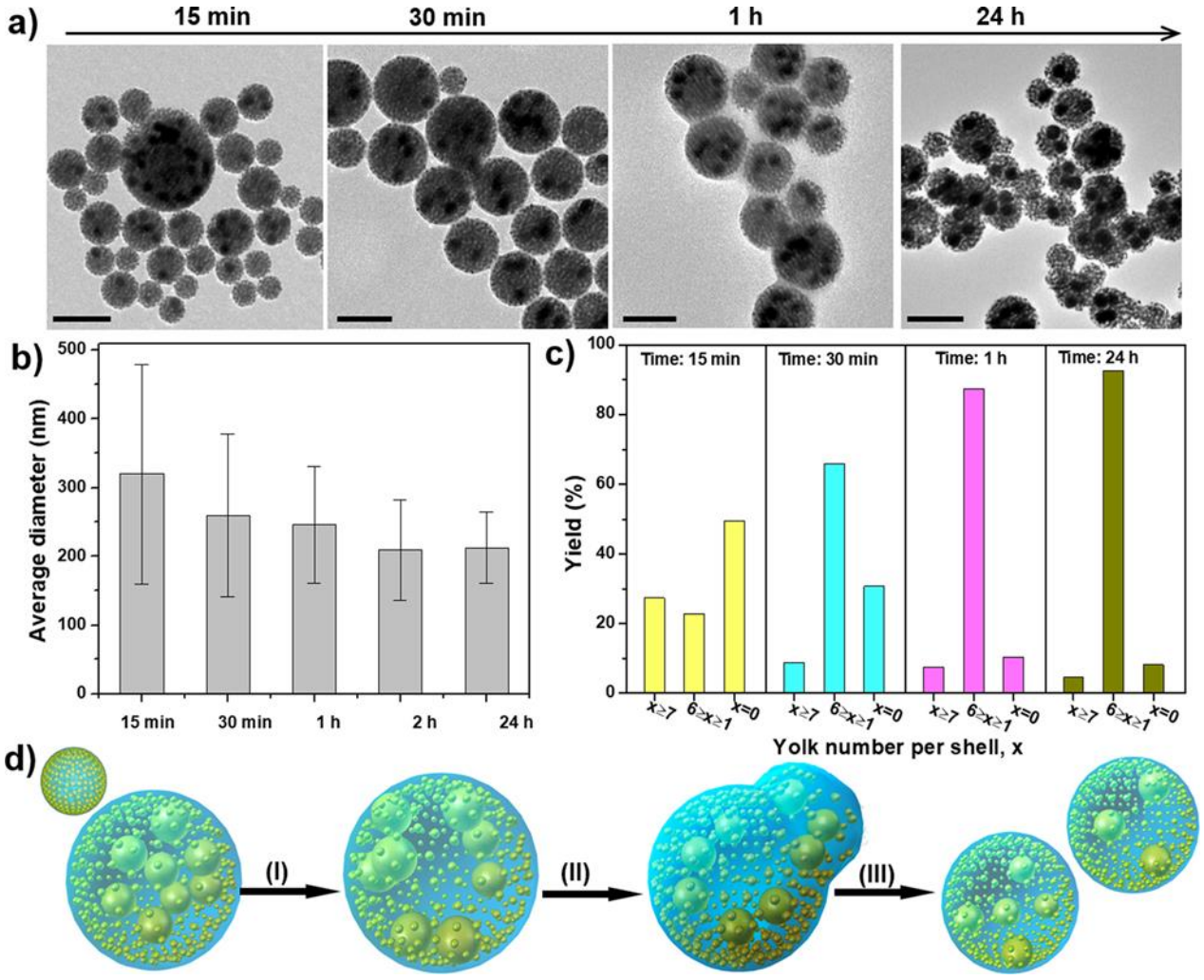

Figure 4.7 (a) TEM images of the assembly structures at different time points. (b,c) The average diameter of vesicles (b) and distribution of yolk number per shell (c) at different time points. (d) Schematic illustration of the proposed formation mechanism of YSVs that involves: the fusion of large vesicles with small ones (I), the development of buds (II), and division of the vesicles. The scale bars: 300 nm

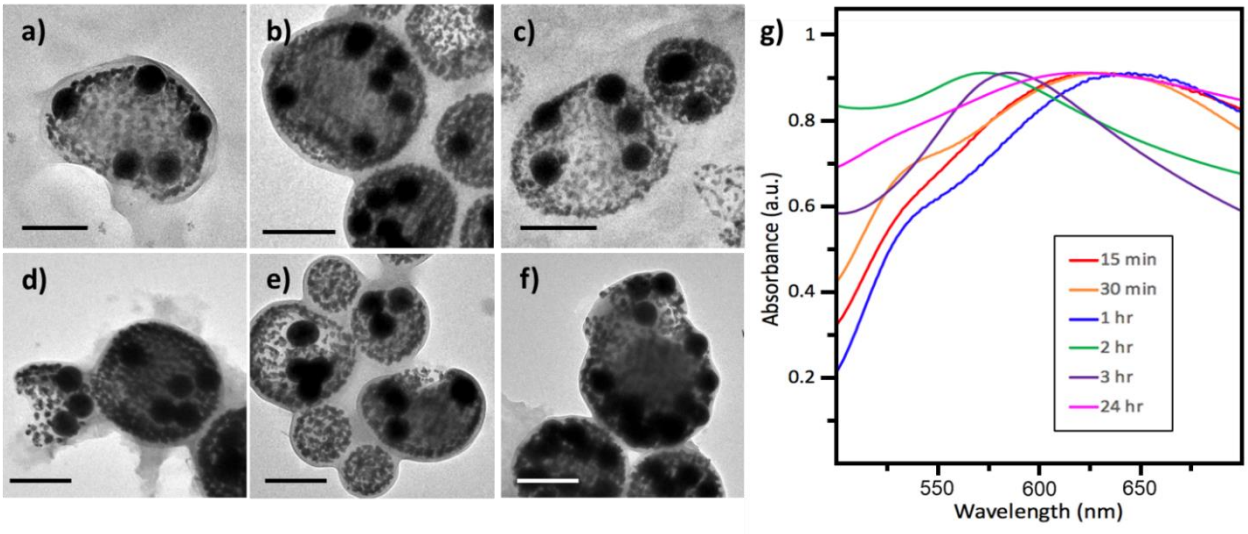

Figure 4.8 (a-g) Representative TEM images and UV-Vis spectra from a binary mixture: Au NS_{10} and Au NS_{75} grafted with PS_{652}-b-PEO_{82}. (a-f) TEM images of membrane budding observed in the assembly of m-YSVs from binary mixture (g) Time-dependent UV-Visible spectra of assembly structures in the assembly of NPAMs in THF/water. The scale bars are 200 nm.

4.3.4 Effect of size ratio and concentration of NPAMs on Assembly

The effect size ratio of small (D_S) and large (D_L) NPAMs and relative molar concentrations (ϕ_S / ϕ_L) strongly influenced the phase separation behaviors in assembled structures. First, we investigated the size effect of NPAMs on their assembly behavior in solution. Small NPAMs with D_S = 10 nm were mixed with one of the larger NPAMs with D_L = 20, 60, 75 and 100 nm. The measured ϕ_L of the large NPAMs are found in Table 4.2. Depending on their relative size, the binary NPAMs assembled into hybrid vesicles with different morphologies, including HVs, PVs, m-YSVs and s-YSVs (Figure 4.9). At D_L / D_S = 20 nm/10 nm, the assembly produced HVs where two types of NPAMs randomly distributed in the membranes without obvious segregation. At D_L / D_S = 60 nm/10 nm, the binary NPAMs laterally segregated in vesicular membranes to form PVs. With further increasing D_L / D_S to 75 nm/10 nm, all the large NPAMs were segregated inside the vesicles to form m-YSVs with multiple yolks, rather than stabilized in the vesicular membranes. When the size difference between the NPAMs was even larger (D_L / D_S = 100 nm/10 nm), the

interior space was not sufficient to accommodate multiple yolks with a larger D_L. The number of yolks inside vesicles reduced to yield s-YSVs with a single yolk.

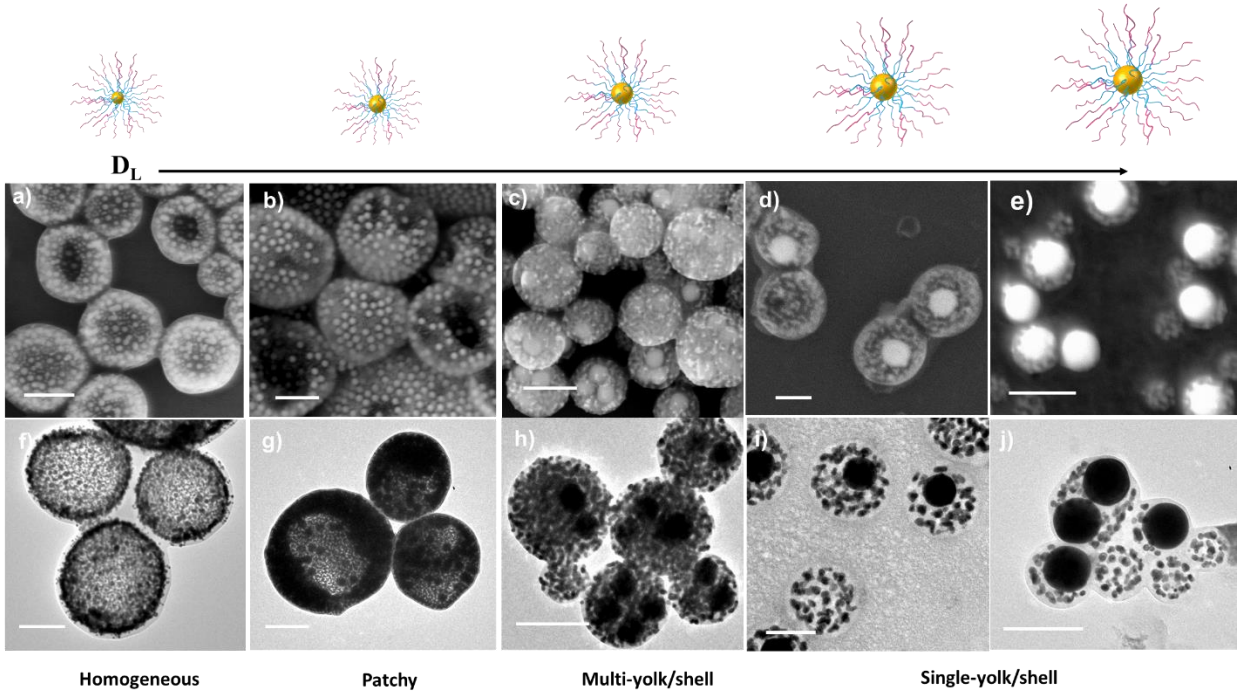

Figure 4.9 Hybrid vesicles formed from NPAMs with different dimensions (a-h). SEM (a-d) and TEM (e-h) images of homogeneous vesicles (a,e), patchy vesicles (b, g). multi-yolk/shell vesicles (c, h), and single-yolk/shell vesicles(d, e, i, j). The hybrid vesicles were assembled from different binary mixtures Au-10-PS_{652}-b-PEO_{82}/Au-D_L-PS_{652}-b-PEO_{82}: D_L = (a, f) 20 (b, g) 60 (c, h) 75, (d, i) 85 (e, j) 100. Scale bars: 100 nm (d, i), 200 nm (a, c, e, f, h, j), and 300 nm (g).c

We systematically varied the size and relative molar concentration of NPAMs in the binary mixture. The effect of the two factors on assembly structures was summarized in a phase-like diagram (Figure 4.10). The relative size of binary NPAMs (i.e., D_L / Ds) is crucial to the morphological transition of hybrid vesicles. When D_L / Ds is small, the binary NPAMs are confined within the membranes as uniform distribution or segregated domains. Above a threshold value of D_L / Ds , the large NPAMs are excluded from the membranes into the interior of vesicles. Moreover, the morphology of assembled vesicles is strongly dependent on (ϕ_S / ϕ_L). The increase

in (ϕ_S / ϕ_L) leads to a transition of the assembly structures from HVs to PVs, to m-YSVs and eventually to s-YSVs.

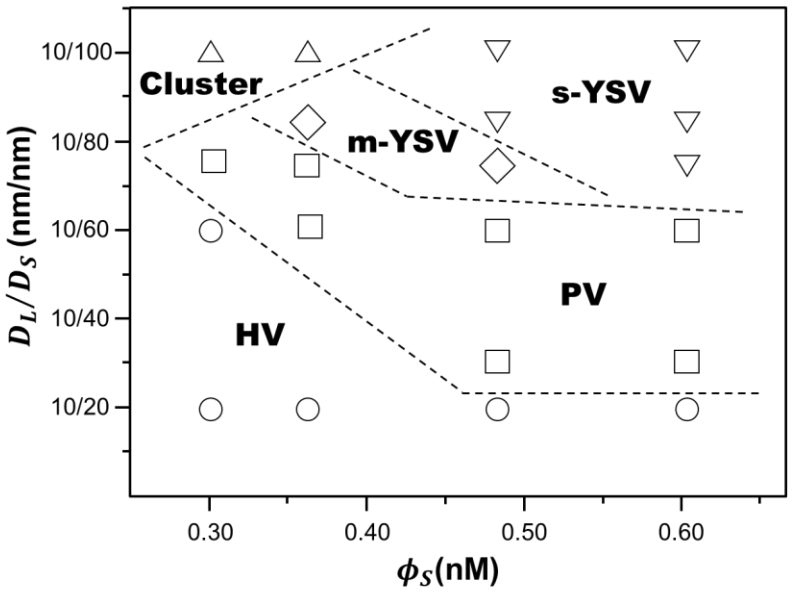

Figure 4.10 Phase diagram of the co-assembly of large NPAMs with varying D_L of Au NS and small NPAMs (D_L = 10 nm) with varying ϕ_S. The dashed lines are used for eye guidance.

4.4 Conclusion

In summary, we have demonstrated the co-assembly of binary NPAMs with distinct sizes into hybrid vesicles with different morphologies. Depending on their relative size and concentration, the binary NPAMs segregated laterally within the vesicular membranes or vertically into the vesicles along the direction normal to the membrane, driven by the conformational entropy gain of end-grafted copolymer ligands. Moreover, our kinetic study suggests that the formation of YSVs is a multi-step process involving the re-organization of NPAMs. Specifically, the fusion and budding of vesicular membranes is essential to the formation of uniform vesicles with yolks inside. This study may provide guidance for the development of advanced drug delivery vehicles, such as multi-compartmental nanostructures.[120]

Chapter 5: Conclusions

5.1 Conclusions

This dissertation makes valuable contributions to the field of nanoscience by providing a comprehensive investigation into the self-assembly of PGNPs in selective solvents. The objective of this dissertation was to fabricate hierarchal structures from the self-organization of PGNPs utilizing a cost-effective and scalable approach, with the intention to exploit the optical properties for biomedical applications.

First, we demonstrated that vesicular structures could be produced from the self-assembly of polymer grafted anisotropic Au NPs. Vesicles were metastable structures, and the resulting optical properties were influenced by the, NP shape, BCP length and heat stimuli. Preliminary findings highlighted the optical benefits of designing and tailoring nanostructures with anisotropic shapes.

Second, we demonstrated that the co-assembly of PGNPs is a scalable and versatile assembly approach to prepare hybrid vesicle structures with distinct morphologies that can accommodate various nanoparticle shapes and dimensions. Au NPs with various geometric shapes in binary mixtures of B-PGNPs can co-assembled into hybrid vesicles with well-defined morphologies, including patchy vesicles (PVs) with distinct domains of small and large B-PGNPs and yolk/shell vesicles (YVs) with large B-PGNPs randomly distributed or centrally located inside the hollow cavities of vesicular membranes containing small B-PGNPs. The formation of these hybrid assemblies depended on the BCP length, ration of NP dimensions, and concentration of small B-PGNPs.

Third, we focused on developing a practical guide for the co-assembly of spherical PGNPs with distinct sizes into well-defined hybrid vesicles, in addition to understanding the phase

separation mechanisms of PGNPs in the vesicular membrane. Small and large B-PGNPs segregated laterally within the vesicular membranes or vertically into the vesicles along the direction normal to the membrane, driven by the conformational entropy gain of end-grafted copolymer ligands, depending on their relative size and concentration. Our kinetic study suggests that the formation of YSVs is a multi-step process involving the re-organization of B-PGNPs. Specifically, the fusion and budding of vesicular membranes is essential to the formation of uniform vesicles with yolks inside.

By unveiling the self-assembly of behavior of PGNPs in selective solvents, this research provides insights that can expand our understanding of assembly mechanisms, develop predictive models, and explore practical applications. The research outcomes presented in this dissertation further enhance our ability to harness the power of self-assembled PGNPs for the creation of functional nanomaterials with tailored properties and applications.

5.2 Future Work

The self-assembly of polymer grafted anisotropic NPs in solution represents a fascinating area of research with significant implications for modern medical and biological studies. However, current research on PGNP self-assembly is still in the early stages, which opens many avenues for further exploration and refinement. For instance, vesicles exhibited irregular shapes and disordered packing from the self-assembly of large anisotropic NPs (70-90 nm) and Au NC tethered with long BCP lengths, indicating limited control over their organization. Future research efforts should focus on elucidating the underlying mechanisms, developing predictive models, and expanding the repertoire of functional applications. The remaining section outlines a few potential points for further investigations.

Multidisciplinary Collaboration: Interdisciplinary research is vital to address complex challenges at the nanoscale level. Preliminary investigations have highlighted the importance of various factors such as copolymer length, nanoparticle size, and thermodynamic principles in governing the self-assembly anisotropic PGNPs and co-assembly process PGNPs with different dimensions. For instance, our results also suggest that the organization of anisotropic nanoparticles, such as cubes, depends on the shape of the grafted polymer shell. Although a more robust quantitative analysis of how geometric constraints imposed by anisotropic NPs affect the relationship between brush conformation and vesicle formation is needed, the methodologies presented here provide a foundation for researchers from chemistry, materials science, and bioengineering to engage in collaborative efforts.

Advanced Characterization Techniques: Precise characterizations of PGNPs and the resulting structures are crucial to accurately predict their self-assembly behavior. The combination of advanced characterization techniques, such as high-resolution in-situ imaging and spectroscopy, is essential to providing insights into the assembly processes of PGNPs. Attenuated total reflectance FTIR (ATR-FTIR) could further provide information about the surface coverage and intermolecular interactions of grafted polymer brushes. This can potentially bridge the gap between the solvent-polymer interactions and self-assembly outcomes. Additionally, cryo-TEM paired with electron tomography could be employed to elucidate complex morphologies of PGNP structures in the solvated state.

Theoretical Modeling and Simulation: Computational approaches, such as molecular dynamics simulations and coarse-grained modeling, should be utilized to predict and reproduce the self-assembly behavior based on the shape of the grafted polymer shell. These simulations would offer a deeper understanding of the underlying mechanisms, elucidating how specific

polymer shell shapes influence the organization and resulting structures of anisotropic PGNPs. Moreover, computational modeling and theoretical studies can further elucidate the thermodynamic and entropic effects associated with the self-assembly process. The organization of anisotropic nanoparticles, driven by the shape of the grafted polymer shell, imparts distinct properties and functionalities. The resulting structures may exhibit unique optical, electronic, or catalytic properties that arise from the specific spatial arrangement of the nanoparticles. By tailoring the shape of the polymer shell, it becomes possible to control the organization and, consequently, the properties of anisotropic nanoparticles for targeted applications.

Exploration of Multi-Component Systems: The co-assembly of PGNPs in solution enables the scalable design of nanostructures with synergistic properties for nanomedicine. We have shown that hybrid vesicles produced from anisotropic Au NPs tethered with PEO-*b*-PS copolymers exhibit extraordinary optical properties due to the plasmon coupling between sharp vertices and edges. To fully realize the functional implications of hybrid vesicles, other nanoparticles compositions, like magnetic NPs should be implemented as building blocks. By continuing to advance our understanding of PGNP self-assembly and tailoring the components of hybrid vesicles, we can unlock the full potential of these nanoscale building blocks and pave the way for innovative technologies and materials with tailored properties and functionalities.

Appendices

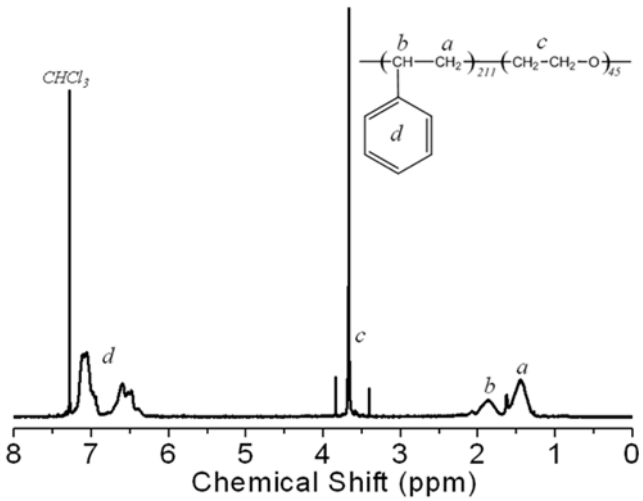

Figure 3.S1 ^{1}H NMR spectrum of PEO$_{45}$-*b*-PS$_{211}$-SH.

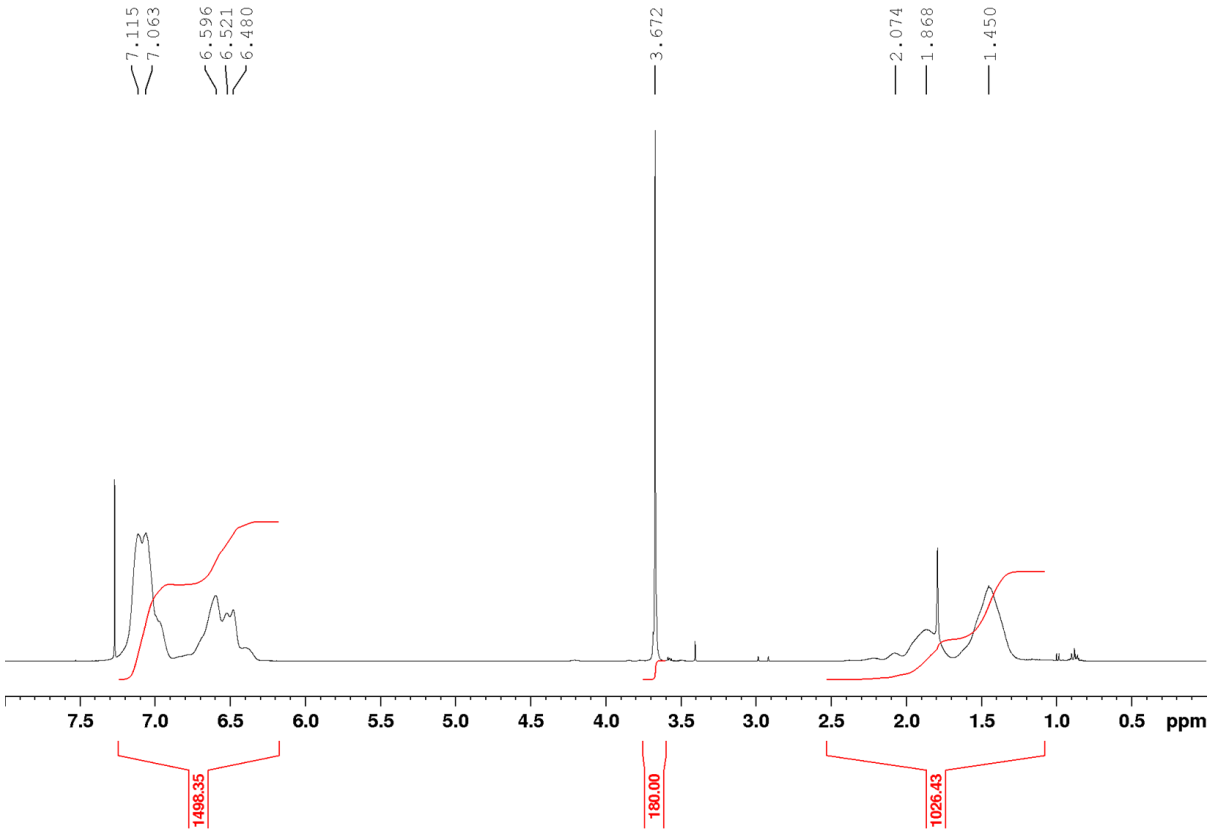

Figure 3.S2 ^{1}H NMR spectrum of PEO$_{45}$-*b*-PS$_{300}$-SH.

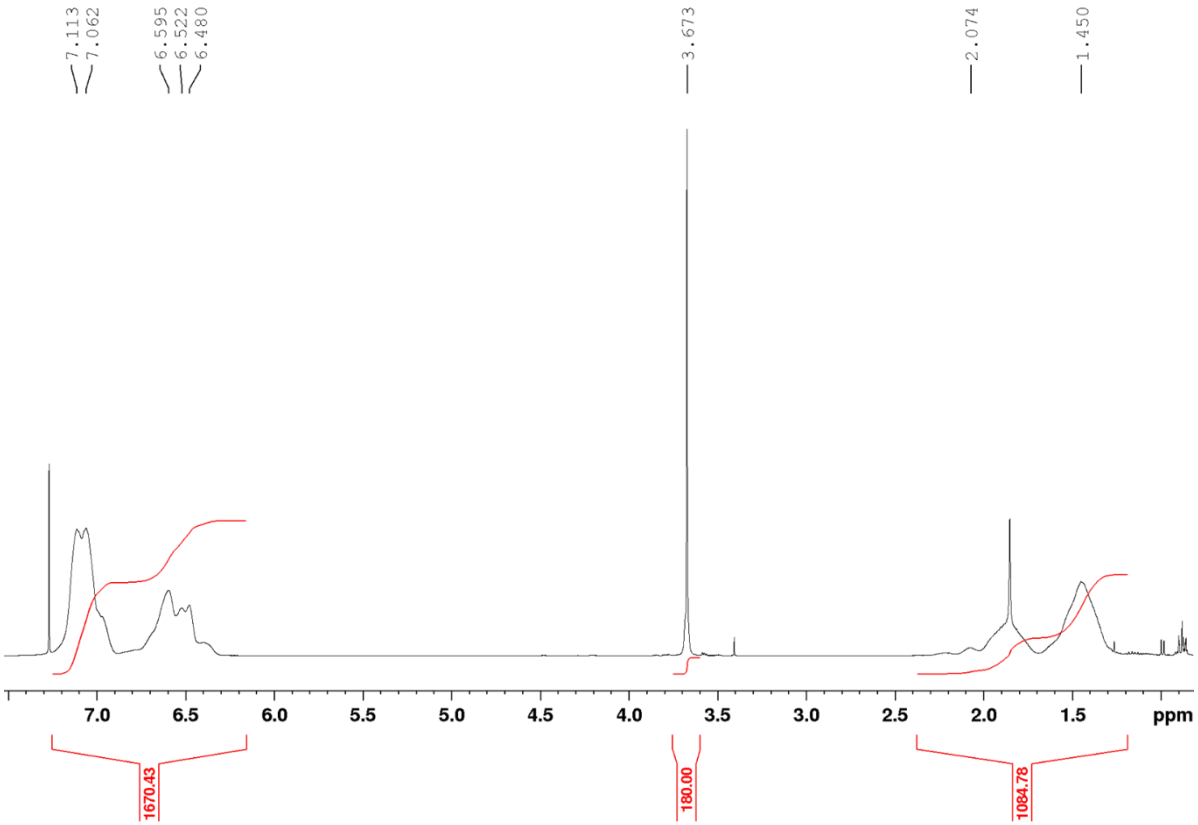

Figure 3.S3 ^{1}H NMR spectrum of PEO_{45}-*b*-PS_{99}-SH.

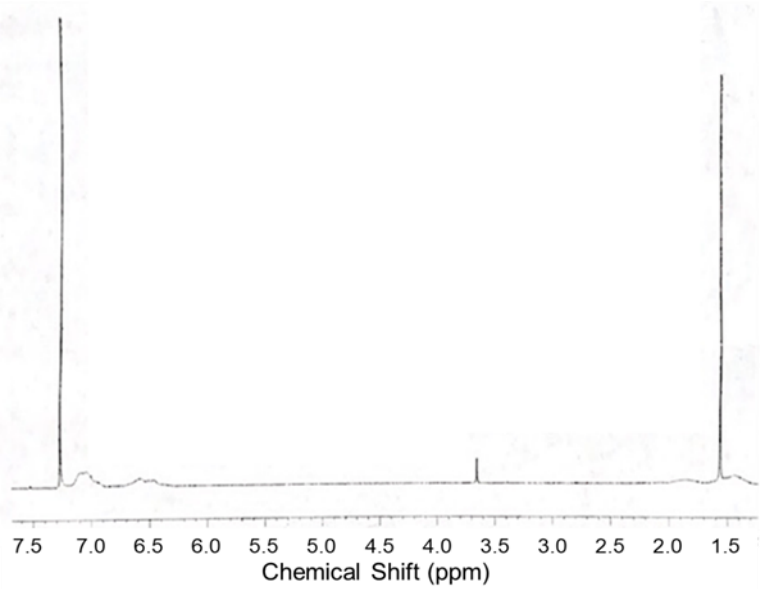

Figure 3.S4 ^{1}H NMR spectrum of PEO_{82}-*b*-PS_{652}-SH.

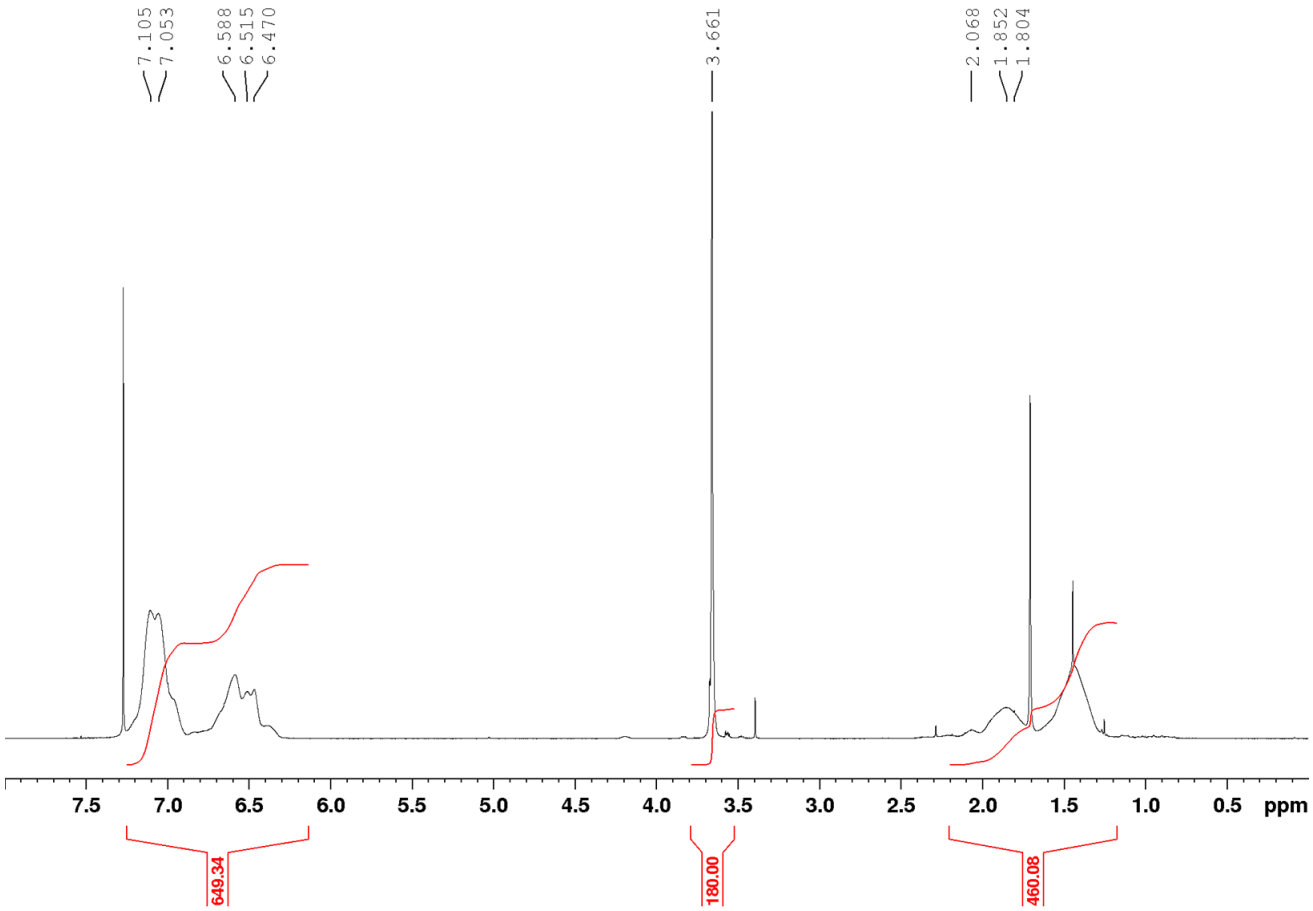

Figure 3.S5 ^{1}H NMR spectrum of PEO_{45}-*b*-PS_{130}-SH.

References

1. Wang, L.; Hasanzadeh Kafshgari, M.; Meunier, M. Optical Properties and Applications of Plasmonic-Metal Nanoparticles. *Adv. Funct. Mater.* **2020**.
2. Kao, J.; Thorkelsson, K.; Bai, P.; Rancatore, B. J.; Xu, T. Toward Functional Nanocomposites: Taking the Best of Nanoparticles, Polymers, and Small Molecules. *Chem. Soc. Rev.* **2013**, *42* (7).
3. Xia, Y.; Yang, H.; Campbell, C. T. Nanoparticles for Catalysis. *Acc. Chem. Res*. **2013**, *46* (8), 1671–1672.
4. Stratakis, E.; Kymakis, E. Nanoparticle-Based Plasmonic Organic Photovoltaic Devices. Mater. Today 2013, 16 (4), 133–146.
5. Kramer, I. J.; Sargent, E. H. The Architecture of Colloidal Quantum Dot Solar Cells: Materials to Devices. *Chem. Rev.* **2014**, *114* (1), 863–882.
6. Yang, L.; Zhou, Z.; Song, J.; Chen, X. Anisotropic Nanomaterials for Shape-Dependent Physicochemical and Biomedical Applications. Chem. Soc. Rev. 2019, 48 (19), 5140.
7. Prodan, E.; Radloff, C.; Halas, N. J.; Nordlander, P. A Hybridization Model for the Plasmon Response of Complex Nanostructures. *Science 2003*, *302* (5644), 419–422.
8. Halas, N. J.; Lal, S.; Chang, W.-S.; Link, S.; Nordlander, P. Plasmons in Strongly Coupled Metallic Nanostructures. *Chem. Rev.* **2011**, *111* (6), 3913–3961.
9. Gwo, S.; Chen, H. Y.; Lin, M. H.; Sun, L.; Li, X. Nanomanipulation and Controlled Self-Assembly of Metal Nanoparticles and Nanocrystals for Plasmonics. *Chem. Soc. Rev.* **2016**, *45* (20), 5672–5716.
10. Willets, K. A.; Van Duyne, R. P. Localized Surface Plasmon Resonance Spectroscopy and Sensing. Annu. Rev. *Phys. Chem*. **2007,** *58*, 267–297.
11. Jain, P. K.; Huang, W.; El-Sayed, M. A. On the Universal Scaling Behavior of the Distance Decay of Plasmon Coupling in Metal Nanoparticle Pairs: A Plasmon Ruler Equation. *Nano Lett.* **2007**, *7* (7), 2080–2088.
12. Klinkova, A.; Choueiri, R. M.; Kumacheva, E. Self-Assembled Plasmonic Nanostructures. *Chem. Soc. Rev*. **2014**, *43* (11), 3976.
13. Fan, J. A.; Wu, C.; Bao, K.; Bao, J.; Bardhan, R.; Halas, N. J.; Manoharan, V. N.; Nordlander, P.; Shvets, G.; Capasso, F. Self-Assembled Plasmonic Nanoparticle Clusters. *Science*. **2010**, *328* (5982), 1135–1138.
14. Yi, C.; Yang, Y.; Liu, B.; He, J.; Nie, Z. Polymer-Guided Assembly of Inorganic Nanoparticles. *Chem. Soc. Rev*. **2020**, *49* (2).
15. Duan, H.; Yang, Y.; Zhang, Y.; Yi, C.; Nie, Z.; He, J. What Is next in Polymer-Grafted Plasmonic Nanoparticles? *Giant* **2020,** *4*, 100033.
16. Schattling, P.; Jochum, F. D.; Theato, P. Multi-Stimuli Responsive Polymers – the All-in-One Talents. *Polym. Chem*. **2013**, *5* (1), 25–36.
17. Moffitt, M. G. Self-Assembly of Polymer Brush-Functionalized Inorganic Nanoparticles: From Hairy Balls to Smart Molecular Mimics. *J. Phys. Chem. Lett*. **2013**, *4* (21), 3654–3666.

18. Choueiri, R. M.; Klinkova, A.; Thérien-Aubin, H.; Rubinstein, M.; Kumacheva, E. Structural Transitions in Nanoparticle Assemblies Governed by Competing Nanoscale Forces. *J. Am. Chem. Soc.* **2013**, *135* (28).
19. Marla, K. T.; Meredith, J. C. Simulation of Interaction Forces between Nanoparticles: End-Grafted Polymer Modifiers. *J. Chem. Theory Comput.* **2006**, *2* (6), 1624–1631.
20. Jiao, Y.; Tibbits, A.; Gillman, A.; Hsiao, M.-S.; Buskohl, P.; Drummy, L. F.; Vaia, R. A. Deformation Behavior of Polystyrene-Grafted Nanoparticle Assemblies with Low Grafting Density. *Macromolecules* **2018**, *51* (18), 7257–7265.
21. Gao, B.; Arya, G.; Tao, A. R. Self-Orienting Nanocubes for the Assembly of Plasmonic Nanojunctions. *Nat. Nanotechnol.* **2012**, *7* (7), 433–437.
22. Gao, B.; Alvi, Y.; Li, V.; Tao, A. R. Polymer-Directed Assembly of Colloidal Nanoparticle Heterojunctions. *CrystEngComm.* **2014**, *16* (40), 9434–9440.
23. Gao, B.; Alvi, Y.; Rosen, D.; Lav, M.; Tao, A. R. Designer Nanojunctions: Orienting Shaped Nanoparticles within Polymer Thin-Film Nanocomposites. *Chem. Commun.* **2013**, *49* (39), 4382–4384.
24. Gurunatha, K. L.; Marvi, S.; Arya, G.; Tao, A. R. Computationally Guided Assembly of Oriented Nanocubes by Modulating Grafted Polymer–Surface Interactions. *Nano Lett.* **2015**, *15* (11).
25. Choueiri, R. M.; Galati, E.; Thérien-Aubin, H.; Klinkova, A.; Larin, E. M.; Querejeta-Fernández, A.; Han, L.; Xin, H. L.; Gang, O.; Zhulina, E. B.; Rubinstein, M.; Kumacheva, E. Surface Patterning of Nanoparticles with Polymer Patches. *Nat.* **2016,** *538* (7623), 79–83.
26. Yi, C.; Zhang, S.; Webb, K. T.; Nie, Z. 9 - Anisotropic Self-Assembly of Hairy Inorganic Nanoparticles. *Acc. Chem. Res.* **2016**, *50* (1), 12–21.
27. Galati, E.; Tebbe, M.; Querejeta-Fernández, A.; Xin, H. L.; Gang, O.; Zhulina, E. B.; Kumacheva, E. Shape-Specific Patterning of Polymer-Functionalized Nanoparticles. *ACS Nano*. **2017**, *11* (5), 4995–5002.
28. Choueiri, R. M.; Klinkova, A.; Pearce, S.; Manners, I.; Kumacheva, E. Self-Assembly and Surface Patterning of Polyferrocenylsilane-Functionalized Gold Nanoparticles. Macromol. *Rapid Commun.* **2018**, *39* (3), 1700554.
29. Galati, E.; Tao, H.; Tebbe, M.; Ansari, R.; Rubinstein, M.; Zhulina, E. B.; Kumacheva, E. Helicoidal Patterning of Nanorods with Polymer Ligands. *Angew. Chemie Int. Ed.* **2019**, *58* (10), 3123–3127.
30. Nie, Z.; Fava, D.; Kumacheva, E.; Zou, S.; Walker, G. C.; Rubinstein, M. Self-Assembly of Metal–Polymer Analogues of Amphiphilic Triblock Copolymers. *Nat. Mater.* **2007**, *6* (8), 609–614.
31. Nie, Z.; Fava, D.; Rubinstein, M.; Kumacheva, E. "Supramolecular" Assembly of Gold Nanorods End-Terminated with Polymer "Pom-Poms": Effect of Pom-Pom Structure on the Association Modes. *J. Am. Chem. Soc*. **2008**, *130* (11), 3683–3689.
32. Zhang, Z.; Horsch, M. A.; Lamm, M. H.; Glotzer, S. C. Tethered Nano Building Blocks: Toward a Conceptual Framework for Nanoparticle Self-Assembly. *Nano Lett.* **2003**, *3* (10), 1341–1346.

33. Akcora, P.; Liu, H.; Kumar, S. K.; Moll, J.; Li, Y.; Benicewicz, B. C.; Schadler, L. S.; Acehan, D.; Panagiotopoulos, A. Z.; Pryamitsyn, V.; Ganesan, V.; Ilavsky, J.; Thiyagarajan, P.; Colby, R. H.; Douglas, J. F. Anisotropic Self-Assembly of Spherical Polymer-Grafted Nanoparticles. *Nat. Mater.* **2009**, *8* (4), 354–359.
34. Zhao, B.; Zhu, L. Mixed Polymer Brush-Grafted Particles: A New Class of Environmentally Responsive Nanostructured Materials. *Macromolecule*s. **2009**, *42* (24), 9369–9383.
35. Tang, S.; Lo, T.-Y.; Horton, J. M.; Bao, C.; Tang, P.; Qiu, F.; Ho, R.-M.; Zhao, B.; Zhu, L. Direct Visualization of Three-Dimensional Morphology in Hierarchically Self-Assembled Mixed Poly(Tert -Butyl Acrylate)/Polystyrene Brush-Grafted Silica Nanoparticles. *Macromolecules*. **2013,** *46* (16), 6575–6584.
36. Bao, C.; Tang, S.; Wright, R. A. E.; Tang, P.; Qiu, F.; Zhu, L.; Zhao, B. Effect of Molecular Weight on Lateral Microphase Separation of Mixed Homopolymer Brushes Grafted on Silica Particles. *Macromolecules*. **2014**, *47* (19), 6824–6835.
37. Fox, T. L.; Tang, S.; Horton, J. M.; Holdaway, H. A.; Zhao, B.; Zhu, L.; Stewart, P. L. In Situ Characterization of Binary Mixed Polymer Brush-Grafted Silica Nanoparticles in Aqueous and Organic Solvents by Cryo-Electron Tomography. *Langmuir* **2015**, *31* (31), 8680–8688.
38. Koski, J. P.; Frischknecht, A. L. Fluctuation Effects on the Brush Structure of Mixed Brush Nanoparticles in Solution. *ACS Nano* **2018**, *12* (2), 1664–1672.
39. Chen, L.; Klok, H.-A. "Multifaceted" Polymer Coated, Gold Nanoparticles. *Soft Matter* **2013**, *9* (45), 10678.
40. Nakano, T.; Kawaguchi, D.; Matsushita, Y. Anisotropic Self-Assembly of Gold Nanoparticle Grafted with Polyisoprene and Polystyrene Having Symmetric Polymer Composition. *J. Am. Chem. Soc*. **2013**, *135* (18), 6798–6801.
41. Wang, Y.; Yang, G.; Tang, P.; Qiu, F.; Yang, Y.; Zhu, L. Mixed Homopolymer Brushes Grafted onto a Nanosphere. *J. Chem. Phys*. **2011**, *134* (13).
42. Jahn, A.; Stavis, S. M.; Hong, J. S.; Vreeland, W. N.; DeVoe, D. L.; Gaitan, M. Microfluidic Mixing and the Formation of Nanoscale Lipid Vesicles. *ACS Nano* **2010,** *4* (4), 2077–2087.
43. Song, J.; Cheng, L.; Liu, A.; Yin, J.; Kuang, M.; Duan, H. Plasmonic Vesicles of Amphiphilic Gold Nanocrystals: Self-Assembly and External-Stimuli-Triggered Destruction. *J. Am. Chem. Soc*. **2011**, *133* (28), 10760–10763.
44. Cheng, L.; Song, J.; Yin, J.; Duan, H. Self-Assembled Plasmonic Dimers of Amphiphilic Gold Nanocrystals. *J. Phys. Chem. Lett*. **2011**, *2* (17), 2258–2262.
45. Zubarev, E. R.; Xu, J.; Sayyad, A.; Gibson, J. D. Amphiphilicity-Driven Organization of Nanoparticles into Discrete Assemblies. *J. Am. Chem. Soc*. **2006**, *128* (47), 15098–15099.
46. Guo, Y.; Harirchian-Saei, S.; Izumi, C. M. S.; Moffitt, M. G. Block Copolymer Mimetic Self-Assembly of Inorganic Nanoparticles. *ACS Nano*. **2011**, *5* (4), 3309–3318.
47. Song, J.; Wu, B.; Zhou, Z.; Zhu, G.; Liu, Y.; Yang, Z.; Lin, L.; Yu, G.; Zhang, F.; Zhang, G.; Duan, H.; Stucky, G. D.; Chen, X. Double-Layered Plasmonic-Magnetic Vesicles by

Self-Assembly of Janus Amphiphilic Gold-Iron(II,III) Oxide Nanoparticles. *Angew. Chemie Int. Ed*. **2017**, *56* (28), 8110–8114.
48. Song, J.; Lin, L.; Yang, Z.; Zhu, R.; Zhou, Z.; Li, Z.-W.; Wang, F.; Chen, J.; Yang, H.; Chen, X. Self-Assembled Responsive Bilayered Vesicles with Adjustable Oxidative Stress for Enhanced Cancer Imaging and Therapy. *J. Am. Chem. Soc*. **2019**, *141* (20), 8158–8170.
49. Rossner, C.; Zhulina, E. B.; Kumacheva, E. Staged Surface Patterning and Self-Assembly of Nanoparticles Functionalized with End-Grafted Block Copolymer Ligands. *Angew. Chemie Int. Ed*. **2019**, *58* (27), 9269–9274.
50. Zhou, Y.; Ma, X.; Zhang, L.; Lin, J. Directed Assembly of Functionalized Nanoparticles with Amphiphilic Diblock Copolymers. *Phys. Chem*. **2017**, *19* (28), 18757–18766.
51. Gong, M.; Yu, Q.; Wang, C.; Wang, R. Simulating Surface Patterning of Nanoparticles by Polymers via Dissipative Particle Dynamics Method. *Langmuir* **2019**, *35* (16), 5534–5540.
52. Liu, Y.; Liu, Y.; Yin, J.-J.; Nie, Z. Self-Assembly of Amphiphilic Block Copolymer-Tethered Nanoparticles: A New Approach to Nanoscale Design of Functional Materials. Macromol. *Rapid Commun*. **2015**, *36* (8), 711–725.
53. He, J.; Liu, Y.; Babu, T.; Wei, Z.; Nie, Z. Self-Assembly of Inorganic Nanoparticle Vesicles and Tubules Driven by Tethered Linear Block Copolymers. *J. Am. Chem. Soc*. **2012**, *134* (28), 11342–11345.
54. He, J.; Huang, X.; Li, Y.-C.; Liu, Y.; Babu, T.; Aronova, M. A.; Wang, S.; Lu, Z.; Chen, X.; Nie, Z. Self-Assembly of Amphiphilic Plasmonic Micelle-Like Nanoparticles in Selective Solvents. *J. Am. Chem. Soc*. **2013**, *135* (21), 7974–7984.
55. Liu, Y.; He, J.; Yang, K.; Yi, C.; Liu, Y.; Nie, L.; Khashab, N. M.; Chen, X.; Nie, Z. Folding Up of Gold Nanoparticle Strings into Plasmonic Vesicles for Enhanced Photoacoustic Imaging. *Angew. Chemie Int. Ed*. **2015**, *54* (52), 15809–15812.
56. Yan, N.; Zhang, Y.; He, Y.; Zhu, Y.; Jiang, W. Controllable Location of Inorganic Nanoparticles on Block Copolymer Self-Assembled Scaffolds by Tailoring the Entropy and Enthalpy Contributions. *Macromolecules*. **2017**, *50* (17), 6771–6778.
57. Yan, N.; Liu, X.; Zhu, J.; Zhu, Y.; Jiang, W. Well-Ordered Inorganic Nanoparticle Arrays Directed by Block Copolymer Nanosheets. *ACS Nano.* **2019**, *13* (6), 6638–6646.
58. Sánchez-Iglesias, A.; Grzelczak, M.; Altantzis, T.; Goris, B.; Pérez-Juste, J.; Bals, S.; Van Tendeloo, G.; Donaldson, S. H.; Chmelka, B. F.; Israelachvili, J. N.; Liz-Marzán, L. M. Hydrophobic Interactions Modulate Self-Assembly of Nanoparticles. *ACS Nano* **2012**, *6* (12), 11059–11065.
59. Galván-Moya, J. E.; Altantzis, T.; Nelissen, K.; Peeters, F. M.; Grzelczak, M.; Liz-Marzán, L. M.; Bals, S.; Van Tendeloo, G. Self-Organization of Highly Symmetric Nanoassemblies: A Matter of Competition. *ACS Nano* **2014,** *8* (4), 3869–3875.
60. Grzelczak, M.; Sánchez-Iglesias, A.; Mezerji, H. H.; Bals, S.; Pérez-Juste, J.; Liz-Marzán, L. M. Steric Hindrance Induces Crosslike Self-Assembly of Gold Nanodumbbells. *Nano Lett*. **2012**, *12* (8), 4380–4384.
61. Zheng, R.; Liu, G.; Xiaohu, Y. Polymer Nano- and Microspheres with Bumpy and Chain-Segregated Surfaces. *J. Am. Chem. Soc.* **2005,** *127* (44), 15358–15359.

62. Liu, Y.; Yang, X.; Huang, Z.; Huang, P.; Zhang, Y.; Deng, L.; Wang, Z.; Zhou, Z.; Liu, Y.; Kalish, H.; Khachab, N. M.; Chen, X.; Nie, Z. Magneto-Plasmonic Janus Vesicles for Magnetic Field-Enhanced Photoacoustic and Magnetic Resonance Imaging of Tumors. *Angew. Chemie Int. Ed.* **2016**, *55* (49), 15297–15300.
63. Ye, X.; Zhu, C.; Ercius, P.; Raja, S. N.; He, B.; Jones, M. R.; Hauwiller, M. R.; Liu, Y.; Xu, T.; Alivisatos, A. P. Structural Diversity in Binary Superlattices Self-Assembled from Polymer-Grafted Nanocrystals. *Nat. Commun.* **2015**, *6* (1), 10052.
64. Gu, X. W.; Ye, X.; Koshy, D. M.; Vachhani, S.; Hosemann, P.; Alivisatos, A. P. Tolerance to Structural Disorder and Tunable Mechanical Behavior in Self-Assembled Superlattices of Polymer-Grafted Nanocrystals. *Proc. Natl. Acad. Sci.* **2017,** *114* (11), 2836–2841.
65. Yang, Y.; Wang, Y.; Jin, S.-M.; Xu, J.; Hou, Z.; Ren, J.; Wang, K.; Lee, E.; Zhang, L.; Zhang, Y.; Zhu, J. 3D Confined Assembly of Polymer-Tethered Gold Nanoparticles into Size-Segregated Structures. *Mater. Chem. Front.* **2019**, *3* (2), 209–215.
66. Fan, W.; Yung, B.; Huang, P.; Chen, X. Nanotechnology for Multimodal Synergistic Cancer Therapy. *Chem. Rev.* **2017**, *117* (22), 13566–13638.
67. Song, J.; Huang, P.; Duan, H.; Chen, X. Plasmonic Vesicles of Amphiphilic Nanocrystals: Optically Active Multifunctional Platform for Cancer Diagnosis and Therapy. *Acc. Chem. Res.* **2015**, *48* (9), 2506–2515.
68. Fu, Q.; Zhu, R.; Song, J.; Yang, H.; Chen, X. Photoacoustic Imaging: Contrast Agents and Their Biomedical Applications. *Adv. Mater.* **2018**, 1805875.
69. Yadav, S.; Sharma, A. K.; Kumar, P. Nanoscale Self-Assembly for Therapeutic Delivery. *Front. Bioeng. Biotechnol.* **2020**, *8*.
70. Lu, H.; Wang, J.; Wang, T.; Zhong, J.; Bao, Y.; Hao, H. Recent Progress on Nanostructures for Drug Delivery Applications. J. *Nanomater.* **2016**, 5762431.
71. Lu, J.; Sun, J.; Li, F.; Wang, J.; Liu, J.; Kim, D.; Fan, C.; Hyeon, T.; Ling, D. Highly Sensitive Diagnosis of Small Hepatocellular Carcinoma Using PH-Responsive Iron Oxide Nanocluster Assemblies. *J. Am. Chem. Soc.* **2018**, *140* (32), 10071–10074.
72. Grzelczak, M.; Liz-Marzán, L. M.; Klajn, R. Stimuli-Responsive Self-Assembly of Nanoparticles. *Chem. Soc. Rev.* **2019**, *48* (5), 1342–1361.
73. Ling, D.; Park, W.; Park, S.; Lu, Y.; Kim, K. S.; Hackett, M. J.; Kim, B. H.; Yim, H.; Jeon, Y. S.; Na, K.; Hyeon, T. Multifunctional Tumor PH-Sensitive Self-Assembled Nanoparticles for Bimodal Imaging and Treatment of Resistant Heterogeneous Tumors. J. Am. Chem. Soc. 2014, 136 (15), 5647–5655.
74. Li, F.; Du, Y.; Liu, J.; Sun, H.; Wang, J.; Li, R.; Kim, D.; Hyeon, T.; Ling, D. Responsive Assembly of Upconversion Nanoparticles for PH-Activated and Near-Infrared-Triggered Photodynamic Therapy of Deep Tumors. *Adv. Mater.* **2018**, *30* (35), 1802808.
75. Liu, Y.; Liu, B.; Nie, Z. Concurrent Self-Assembly of Amphiphiles into Nanoarchitectures with Increasing Complexity. *Nano Today* **2015**, *10* (3), 278–300.
76. Deng, K.; Luo, Z.; Tan, L.; Quan, Z. Self-Assembly of Anisotropic Nanoparticles into Functional Superstructures. *Chem. Soc. Rev.* **2020**, *49* (16).

77. Li, F.; Josephson, D. P.; Stein, A. Colloidal Assembly: The Road from Particles to Colloidal Molecules and Crystals. Angewandte Chemie - International Edition. John Wiley & Sons, Ltd January 10, **2011**, pp 360–388.
78. Wang, D.; Hermes, M.; Kotni, R.; Wu, Y.; Tasios, N.; Liu, Y.; de Nijs, B.; van der Wee, E. B.; Murray, C. B.; Dijkstra, M.; van Blaaderen, A. Interplay between Spherical Confinement and Particle Shape on the Self-Assembly of Rounded Cubes. *Nat. Commun.* **2018**, *9* (1).
79. Thorkelsson, K.; Bai, P.; Xu, T. Self-Assembly and Applications of Anisotropic Nanomaterials: A Review. *Nano Today* **2015**, *10* (1).
80. Jain, P. K.; Lee, K. S.; El-Sayed, I. H.; El-Sayed, M. A. Calculated Absorption and Scattering Properties of Gold Nanoparticles of Different Size, Shape, and Composition: Applications in Biological Imaging and Biomedicine. *J. Phys. Chem. B* **2006,** *110* (14).
81. Lee, S.; Sim, K.; Moon, S. Y.; Choi, J.; Jeon, Y.; Nam, J.-M.; Park, S.-J. Controlled Assembly of Plasmonic Nanoparticles: From Static to Dynamic Nanostructures. *Adv. Mater*. **2021**, 2007668.
82. Wu, H. L.; Kuo, C. H.; Huang, M. H. Seed-Mediated Synthesis of Gold Nanocrystals with Systematic Shape Evolution from Cubic to Trisoctahedral and Rhombic Dodecahedral Structures. *Langmuir* **2010,** *26* (14), 12307–12313.
83. Zheng, Y.; Zhong, X.; Li, Z.; Xia, Y. Successive, Seed-Mediated Growth for the Synthesis of Single-Crystal Gold Nanospheres with Uniform Diameters Controlled in the Range of 5–150 Nm. *Part. Syst. Charact*. **2014**, *31* (2), 266–273.
84. Yue, X.; Liu, X.; Yan, N.; Jiang, W. Self-Assembly of Gold Nanocubes into Three-Dimensional Hollow Colloidosomes and Two-Dimensional Superlattices. *Chem. Commun.* **2020**, *56* (84)
85. Klinkova, A.; Thérien-Aubin, H.; Ahmed, A.; Nykypanchuk, D.; Choueiri, R. M.; Gagnon, B.; Muntyanu, A.; Gang, O.; Walker, G. C.; Kumacheva, E. Structural and Optical Properties of Self-Assembled Chains of Plasmonic Nanocubes. *Nano Lett.* **2014**, *14* (11).
86. Lu, F.; Vo, T.; Zhang, Y.; Frenkel, A.; Yager, K. G.; Kumar, S.; Gang, O. Unusual Packing of Soft-Shelled Nanocubes. *Sci. Adv*. **2019**, *5* (5).
87. Lu, S.-F.; Li, B.-Y.; Li, Y.-C.; Lu, Z.-Y. Computer Simulation Study on the Self-Assembly of Tethered Nanoparticles with Tunable Shapes. *RSC Adv*. **2019**, *9* (3).
88. Hooshmand, N.; El-Sayed, M. A. Collective Multipole Oscillations Direct the Plasmonic Coupling at the Nanojunction Interfaces. Proc. *Natl. Acad. Sci.* **2019**, *116* (39), 19299–19304.
89. Liu, Y.; Li, Y.; He, J.; Duelge, K. J.; Lu, Z.; Nie, Z. Entropy-Driven Pattern Formation of Hybrid Vesicular Assemblies Made from Molecular and Nanoparticle Amphiphiles. *J. Am. Chem. Soc*. **2014**, *136* (6), 2602–2610.
90. Asakura, S.; Oosawa, F. Interaction between Particles Suspended in Solutions of Macromolecules. *J. Polym. Sci.* 1958, *33* (126), 183–192.
91. Sacanna, S.; Irvine, W. T. M.; Chaikin, P. M.; Pine, D. J. Lock and Key Colloids. *Nat.* **2010**, *464* (7288), 575–578.

92. Discher, D. E.; Eisenberg, A. Polymer Vesicles. Science. American Association for the Advancement of Science August 9, **2002**, pp 967–973.
93. Che, H.; Cao, S.; van Hest, J. C. M. Feedback-Induced Temporal Control of "Breathing" Polymersomes To Create Self-Adaptive Nanoreactors. *J. Am. Chem. Soc*. **2018**, *140* (16).
94. Prince, E.; Kumacheva, E. Design and Applications of Man-Made Biomimetic Fibrillar Hydrogels. *Nat. Rev. Mater*. **2019,** *4* (2).
95. Krack, M.; Hohenberg, H.; Kornowski, A.; Lindner, P.; Weller, H.; Förster, S. *Nanoparticle-Loaded Magnetophoretic Vesicles. *J. Am. Chem. Soc.* **2008**, *130* (23), 7315–7320.
96. Sanchez-Gaytan, B. L.; Cui, W.; Kim, Y.; Mendez-Polanco, M. A.; Duncan, T. V.; Fryd, M.; Wayland, B. B.; Park, S.-J. Interfacial Assembly of Nanoparticles in Discrete Block-Copolymer Aggregates. *Angew. Chemie Int. Ed*. **2007**, *46* (48), 9235–9238.
97. Wilson, D. A.; Nolte, R. J. M.; Hest, J. C. M. van. *Entrapment of Metal Nanoparticles in Polymer Stomatocytes. *J. Am. Chem. Soc*. **2012**, *134* (24), 9894–9897.
98. Ma, S.; Qi, D.; Xiao, M.; Wang, R. Controlling the Localization of Nanoparticles in Assemblies of Amphiphilic Diblock Copolymers. *Soft Matter* **2014**, *10* (45), 9090–9097.
99. Warren, S. C.; Messina, L. C.; Slaughter, L. S.; Kamperman, M.; Zhou, Q.; Gruner, S. M.; DiSalvo, F. J.; Wiesner, U. Ordered Mesoporous Materials from Metal Nanoparticle–Block Copolymer Self-Assembly. *Science* **2008**, *320* (5884), 1748–1752.
100. Klinkova, A.; Thérien-Aubin, H.; Choueiri, R. M.; Rubinstein, M.; Kumacheva, E. Colloidal Analogs of Molecular Chain Stoppers. Proc. *Natl. Acad. Sci*. **2013,** *110* (47), 18775–18779.
101. Zhang, W.-B.; Yu, X.; Wang, C.-L.; Sun, H.-J.; Hsieh, I.-F.; Li, Y.; Dong, X.-H.; Yue, K.; Horn, R. Van; Cheng, S. Z. D. Molecular Nanoparticles Are Unique Elements for Macromolecular Science: From "Nanoatoms" to Giant Molecules. *Macromolecules* **2014**, *47* (4), 1221–1239.
102. Liu, K.; Nie, Z.; Zhao, N.; Li, W.; Rubinstein, M.; Kumacheva, E. Step-Growth Polymerization of Inorganic Nanoparticles. *Science* **2010,** *329* (5988), 197–200.
103. Song, J.; Zhou, J.; Duan, H. Self-Assembled Plasmonic Vesicles of SERS-Encoded Amphiphilic Gold Nanoparticles for Cancer Cell Targeting and Traceable Intracellular Drug Delivery. *J. Am. Chem. Soc*. **2012**, *134* (32), 13458–13469.
104. Coleman, B. R.; Moffitt, M. G. Amphiphilic Inorganic Nanoparticles with Mixed Polymer Brush Layers of Variable Composition: Bridging the Paradigms of Block Copolymer and Nanoparticle Self-Assembly. *Chem. Mater*. **2018**, *30* (7), 2474–2482.
105. Eugene R. Zubarev, ; Jun Xu, †; Arshad Sayyad, and; Gibson, J. D. Amphiphilicity-Driven Organization of Nanoparticles into Discrete Assemblies. *J. Am. Chem. Soc.* **2006**, *128* (47), 15098–15099.
106. Yu, X.; Zhang, W.-B.; Yue, K.; Li, X.; Liu, H.; Xin, Y.; Wang, C.-L.; Wesdemiotis, C.; Cheng, S. Z. D. Giant Molecular Shape Amphiphiles Based on Polystyrene–Hydrophilic [60]Fullerene Conjugates: Click Synthesis, Solution Self-Assembly, and Phase Behavior. *J. Am. Chem. Soc*. **2012**, *134* (18), 7780–7787.

107. Wang, B.; Li, B.; Dong, B.; Zhao, B.; Li, C. Y. Homo- and Hetero-Particle Clusters Formed by Janus Nanoparticles with Bicompartment Polymer Brushes. *Macromolecules* **2010**, *43* (22), 9234–9238.
108. Nikolic, M. S.; Olsson, C.; Salcher, A.; Kornowski, A.; Rank, A.; Schubert, R.; Frömsdorf, A.; Weller, H.; Förster, S. Micelle and Vesicle Formation of Amphiphilic Nanoparticles. *Angew. Chemie Int. Ed*. **2009,** *48* (15), 2752–2754.
109. Yi, C.; Yang, Y.; Nie, Z. Alternating Copolymerization of Inorganic Nanoparticles. *J. Am. Chem. Soc.* **2019**, *141* (19), 7917–7925.
110. Hu, J.; Wu, T.; Zhang, G.; Liu, S. Efficient Synthesis of Single Gold Nanoparticle Hybrid Amphiphilic Triblock Copolymers and Their Controlled Self-Assembly. *J. Am. Chem. Soc*. **2012**, *134* (18), 7624–7627.
111. Song, J.; Duan, B.; Wang, C.; Zhou, J.; Pu, L.; Fang, Z.; Wang, P.; Lim, T. T.; Duan, H. SERS-Encoded Nanogapped Plasmonic Nanoparticles: Growth of Metallic Nanoshell by Templating Redox-Active Polymer Brushes. *J. Am. Chem. Soc*. **2014**, *136* (19), 6838–6841.
112. Huang, P.; Lin, J.; Li, W.; Rong, P.; Wang, Z.; Wang, S.; Wang, X.; Sun, X.; Aronova, M.; Niu, G.; Leapman, R. D.; Nie, Z.; Chen, X. Biodegradable Gold Nanovesicles with an Ultrastrong Plasmonic Coupling Effect for Photoacoustic Imaging and Photothermal Therapy. *Angew. Chemie* Int. Ed. **2013**, *52* (52), 13958–13964.
113. He, J.; Wei, Z.; Wang, L.; Tomova, Z.; Babu, T.; Wang, C.; Han, X.; Fourkas, J. T.; Nie, Z. Hydrodynamically Driven Self-Assembly of Giant Vesicles of Metal Nanoparticles for Remote-Controlled Release. *Angew. Chemie Int. Ed*. **2013**, *52* (9), 2463–2468.
114. Mai, Y.; Eisenberg, A. Controlled Incorporation of Particles into the Central Portion of Vesicle Walls. *J. Am. Chem. Soc*. **2010**, *132* (29), 10078–10084.
115. Chen, Y.; Wang, Z.; He, Y.; Yoon, Y. J.; Jung, J.; Zhang, G.; Lin, Z. Light-Enabled Reversible Self-Assembly and Tunable Optical Properties of Stable Hairy Nanoparticles. *Proc. Natl. Acad. Sci*. **2018**, *115* (7), E1391–E1400.
116. Kiely, C. J.; Fink, J.; Brust, M.; Bethell, D.; Schiffrin, D. J. Spontaneous Ordering of Bimodal Ensembles of Nanoscopic Gold Clusters. *Nat*. **1998**, *396* (6710), 444–446.
117. Wei, J.; Niikura, K.; Higuchi, T.; Kimura, T.; Mitomo, H.; Jinnai, H.; Joti, Y.; Bessho, Y.; Nishino, Y.; Matsuo, Y.; Ijiro, K. Yolk/Shell Assembly of Gold Nanoparticles by Size Segregation in Solution. *J. Am. Chem. Soc*. **2016,** *138* (10), 3274–3277.
118. Parola, A.; Reatto, L. Depletion Interaction between Spheres of Unequal Size and Demixing in Binary Mixtures of Colloids. **2015**, *113* (17–18), 2571–2582.
119. Grzelczak, M.; Sánchez-Iglesias, A.; Liz-Marzán, L. M. Solvent-Induced Division of Plasmonic Clusters. *Soft Matter* **2013**, *9* (38), 9094–9098.
120. Pastoriza-Santos, I.; Kinnear, C.; Pérez-Juste, J.; Mulvaney, P.; Liz-Marzán, L. M. Plasmonic Polymer Nanocomposites. *Nat. Rev. Mater.* **2018**, *3* (10), 375–391.